SAPIENZA
UNIVERSITÀ DI ROMA

Sapienza University of Rome

DEPARTMENT OF INFORMATION ENGINEERING, ELECTRONICS AND TELECOMMUNICATIONS

PhD in INFORMATION AND COMMUNICATION TECHNOLOGY (ICT)

THESIS FOR THE DEGREE OF DOCTOR OF PHILOSOPHY

Electromagnetic device for imaged guided microwave ablation

Thesis Advisors

Prof. Marta Cavagnaro

Dr. Lorenzo Crocco

Candidate

Mengchu Wang

Academic Year MMXIX-MMXXII (XXXIV cycle)

Nature is the domain of liberty.

by Alexander von Humboldt

Acknowledgement

Doing research is often like a solitary endeavour but in many ways of group achievement. The journey of pursuing a Ph.D. can be sometimes stressful but, in the meantime, full of self-accomplishment. I believe that I cannot reach the destination of this journey without the help of the following people:

My first thanks should go to my supervisor at CNR-IREA: Dr. Lorenzo Crocco, who offered me this precious opportunity to do my Ph.D. research at CNR-IREA within the EMERALD network. During these three years of study, he followed my study progress closely and always reply to my questions promptly. He frequently gives me pertinent advice on improving my research methodology and correcting my writing issues tirelessness. He is capable of explaining the profound scientific principles in a vivid way thus make the learning process enjoyable. Apart from the scientific mentoring, he also help me on settling down in Naples when I first arrived. He had constantly checked the well-being of me and other Ph.D. students during the pandemic lockdown period and cheer us up with his optimistic spirit and sense of humour. I would not be this productive without his encouragement during the three years of study.

My next thanks go to my supervisor at Sapienza University of Roma: Prof. Marta Cavagnaro, whom I respect deeply. Although we were not able to meet regularly because of the pandemic, she managed to closely follow my research progress remotely and patiently provided me with rich-in-details suggestions for my research. Her genuine interest in science and dedication to cultivating the next generation of researchers had inspired me. I appreciate the in-personal conversation with her, not only for the fruitful scientific discussion but also for the

imperceptible influence on values. As a woman in science, she motivated me and other students that gender is not an intrinsic factor limiting us from excelling in our careers.

I would like to say thank you to my colleague and friend Rosa Scapattici at CNR-IREA for the collaboration at work and fruitful discussion on inverse scattering which enhance my understanding of microwave imaging systems.

I wish to express my gratitude to the following people for their time and expertise:

Prof. Martin O'Halloran and Dr. Laura Farina for hosting my secondment at the National University of Ireland Galway, the secondment offered me the chance to improve my experimental skills and allowed me to get familiar with the microwave liver ablation treatment and bio tissue dielectric properties measurement;

Prof. Nadine Joachimowicz and Prof. Hélène Roussel for hosting my secondment at CNRS remotely. It is a pity that I was not able to participate in the secondment on site due to the Covid-19 pandemic. But their expertise in phantom realization and provided me with a 3D phantom for the experimental set-up play an important role in my thesis;

Prof. Ibrahim Akduman for hosting my secondment at MITOS Medical Technologies remotely and introducing me to the clinical trials of the microwave imaging system for breast cancer.

My acknowledgement also goes to Prof. Sandra Costanzo for the realization of the antenna in the microwave imaging system and for providing me with suggestions on the antenna experimental assessment.

My special thank goes to Branislav Nikovic from WIPL-D for his patient help and in-time responses for me to get familiar with the WIPL-D software.

I have to thank my colleagues and friends at CNR-IREA: Adele Fusco, Sabatino Buonanno, Fabiana Calo, Genni Testa, Stefania Romeo, Olga Zeni, Anna Sannino, Fernando Monterroso for their kind help whenever I have difficulties with my life.

I would like to thank all the ESRs in the EMERALD network, especially Aleksandar Janjic, Soroush Abedi, David Rodriguez-Duarte, Alexandra Prokhorova, and Alvaro Yago for the meaningful technical discussion and the time we spend together, these three years would be a solitude journey without the support of you guys.

Finally, I would like to say thank you to my beloved parents for their constant encouragement, support and unconditional love that let me chase my dream without hesitation. This thesis is dedicated to you.

Table of Contents

List of Figures

List of Tables

Abstract

This dissertation demonstrates the design of a microwave imaging system for monitoring liver thermal ablation treatments.

Liver cancer is the third most deadly cancer worldwide and has an increasing yearly fatality rate. Liver thermal ablation is considered to be an effective alternative to conventional treatment methods such as surgery. However, over the years, real-time monitoring of liver thermal ablation has become a big challenge because the existing modalities like computed tomography (CT), magnetic resonance imaging (MRI), positron emission tomography (PET), and Ultrasound imaging (US) have limitations in the applications at hand, that make them incapable or not suitable of providing real-time temperature values. Therefore, the assessment of the ablation procedure heavily relies on the clinician's experience. Microwave imaging (MWI) is a potential candidate for this clinical need, since it provides a map of the dielectric properties of an unknown target from the knowledge of the scattered electromagnetic field. In fact, during liver thermal ablation treatments, the water molecules in the ablation zone dramatically reduce due to the heating. This process yields a change in dielectric properties values in the ablation zone as compared to the un-treated liver. The principle of microwave imaging for thermal ablation monitoring is to take advantage of the dielectric properties contrast between the ablated zone and the un-treated liver tissue. In fact, by recording and processing the scattered field at different stages of the treatment, it should be possible to image the evolution of the dielectric properties in the domain of interest. According to existing knowledge of the correspondence between liver's dielectric properties values and temperature, it would then be possible to derive the local temperature in the ablation zone and hence determine the ablation stage.

Among the advantages of MWI for thermal ablation monitoring, it could be cited the low-cost, portability, capability of real-time imaging, harmless nature, as exploitation of low-power, non-ionizing radiation. Thanks to these circumstances. MWI has been considered for a number of biomedical applications, such as breast imaging, brain imaging, bone imaging, etc.

A microwave imaging system for monitoring liver thermal ablation treatment would be made by an array of antennas embedded into a coupling medium and located in close proximity to the human abdomen, in front of the area to be treated.

In this research, firstly, a numerical analysis was performed to determine the optimal working conditions in terms of operating frequency and coupling medium dielectric properties. Additionally, the dielectric properties of healthy ex vivo liver, as well as thermally ablated one were measured. Secondly, the antennas in the microwave imaging system were designed within the proposed working condition. Studies were performed with different antenna substrate materials looking for the most compact design. Three different antipodal Vivaldi antennas were designed and compared. After the microwave antenna design was completed, an in-silico assessment of the experimental set-up was performed, to define the optimal number of antennas and their spacing. The optimized set-up consists of eight antennas arranged in a staggered two-rows antennas array configuration immersed inside the coupling medium. Then, a simple yet representative experimental set-up for the validation of the imaging system was studied. The set-up foresees the 8 antennas inserted inside a tank filled with the coupling material; in front of the antenna array, a 3-D printed ellipsoidal phantom filled with tissue-mimicking liquid represents the thermally ablated zone. The retrieved images inside the domain of interest show that the designed system can detect the position of the ablated zone and identify it at different ablation stages. Finally, the chosen antenna was realized and experimentally verified, and a recipe to realize the coupling material was proposed and experimentally tested. Ultimately, the system was experimentally assessed with one antenna mechanically moved in a linear motion measuring the signal in front of the 3-D printed

phantom. The numerical and experimental assessment of the microwave imaging system verifies the feasibility of such a system for liver ablation monitoring.

This study paves the way for the real-time monitoring of liver thermal ablation through microwave imaging techniques.

Chapter 1

Introduction

1.1. Clinical Motivation

Liver cancer is a malignancy that occurs in the cells of the liver. In 2020, it was the sixth most common cancer and the third most deadly cancer worldwide with an increasing yearly fatality rate [1]. The causes of liver cancer could be chronic infection with hepatitis B virus (HBV), hepatitis C virus (HCV), cirrhosis, certain inherited liver diseases, diabetes, fatty liver disease, excessive alcohol consumption, etc [2]. Liver cancer has a higher incidence rate and death rate in developing countries than in developed ones due to a lack of health care infrastructure and insufficient disease management [1]. As liver cancer is a major obstacle to improve life expectancy globally, effective cancer treatments have been investigated over the years. So far, the most used treatment methods for liver cancer are surgery, thermal ablation, embolization therapy, radiation therapy, target drug therapy, chemotherapy, and immunotherapy [3]. The prognosis for liver cancer is patient-dependent. In practice, only 5% to 15% of the patients are suitable for surgical removal [2]. Thermal ablation is the alternative treatment to conventional surgery, being minimally invasive, low-cost, and rapid. Until now, radio frequency ablation, cryoablation, and a more recently, microwave ablation are the main thermal ablation techniques that have been adopted on the clinical side [4].

1.2. Thermal Ablation Techniques

Radio frequency ablation (RFA)

Radio frequency ablation is a technique based on the temperature increase achievable in biological tissues through the absorption of a radiofrequency current. Most devices operate from 375 to 500 kHz [5]. A needle-like electrode is placed in the tumor to heat it, while a ground electrode is appropriately located on the patient's skin. Consequently, the local temperature rises to above 60 ℃ or higher, resulting in cellular death. RFA is a low-cost treatment that has been adopted in the clinic for many years. Hence, extensive experience has been made. It is used to treat tumors that occur in the liver, lung, kidney, and bone. However, the main limitations of RFA, including poor performance near blood vessels and inability to conduct

current through charred tissue, lead to a low rate of complete ablation for tumors bigger than about 3 cm [6].

Cryoablation (CA)

Cryoablation destroys cancer cells through extremely low temperatures. This treatment is performed by inserting a cryoprobe (a hollow needle containing a circulated low-temperature thermal conductive fluid) into the tumor [7]. The cryoprobe can rapidly freeze the tissue to -40℃, which produces the cytotoxic effect of disrupting cellular membranes and achieving cell death [8]. Cryoablation has high precision and is able to produce larger ablation zones as compared to other heat-based ablation techniques like radio frequency ablation and microwave ablation [7]. However, it also increases the risk of post-ablation haemorrhage, and the cost of treatment is rather high [7].

Microwave ablation (MWA)

Similar to RFA, microwave ablation destroys cancer cells by using electromagnetic energy to increase the temperature in the biological tissues. MWA uses electromagnetic energy sources within the microwave spectrum. Most devices operate at either 915 MHz or 2.45 GHz. Correspondingly, a needle-like ablation antenna is inserted into the tumor to be treated, and it is enabled to radiate very high-power microwaves. Active cooling circulation is used to prevent the overheating of the feeding structure (see Figure 1-1) hence allowing higher power to be used in the system. Unlike RFA, no ground pad is needed in microwave ablation. In addition to that, MWA has a higher thermal efficacy resulting in larger volumes of the ablation zone, minimization of the heat sink effect, higher efficiency in coagulating blood vessels, and faster ablation time. MWA is suitable for liver tumors whose dimension can be as big as 5 cm, and can eradicate tumors with a minimally invasive approach, without damaging adjacent vital structures. As such, it can significantly reduce patients' morbidity and mortality rate as compared to other treatment procedures [9].

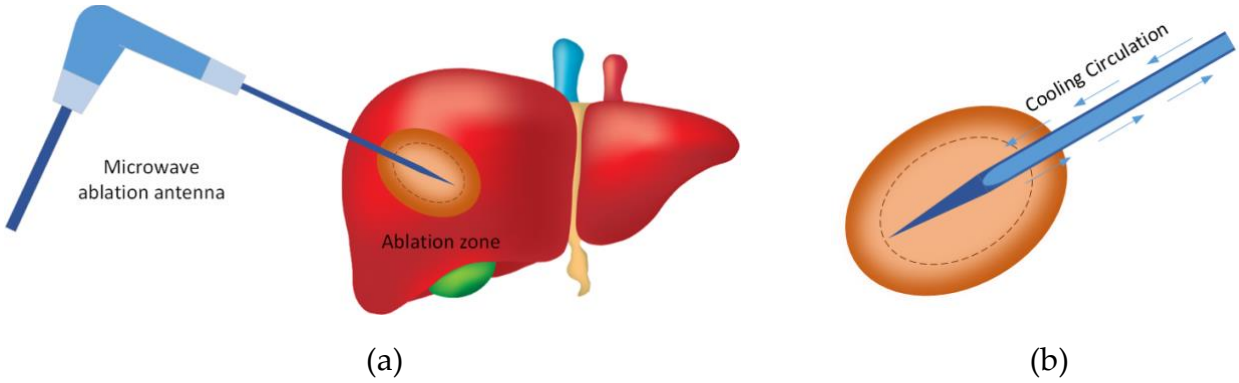

(a) (b)

Figure 1-1 Microwave liver ablation (MWA): (a) schematic (b) ablated zone

The ablated zone often shows an ellipsoidal shape. It is also called the coagulation zone, corresponding to the irreversibly damaged biological tissue. There is a thin layer of hyperemic red rim around the coagulation zone called the transition zone, which contains viable cells [10]. Only the coagulation zone is considered to be "successfully ablated". A coagulation zone that includes the whole tumor plus a safety margin, which in the liver tumor is usually about 5 mm, corresponds to a positive conclusion of the procedure, as insufficient ablated tumorous cells will lead to cancer recurrence [11]. In some systems, in the center of the coagulation zone, temperatures above 100 °C are reached, leading to carbonization of the tissue.

Over the years, the diversity of outcomes has been the main hurdle in the development of thermal ablation treatments. In this respect, the lack of an accurate and objective real-time imaging system to be operated during the treatment for temperature monitoring purposes is one of the most important limitations. Because of this lack, the effectiveness of the treatment mostly relies on the clinician's expertise and skills [12]. Accordingly, the development of real-time monitoring systems is a fundamental issue that researchers must confront to enable the deployment of thermal ablation to reach its full potential.

1.3. Imaging Modalities for Liver Tumor Ablation

Until now, several imaging modalities have been implemented in the clinics at different stages of thermal ablation procedures, such as computed tomography (CT), magnetic resonance imaging (MRI), positron emission tomography (PET), and ultrasound (US).

Computed tomography (CT)

CT uses ionizing radiation to build three-dimensional images of tissue based on the density: the X-rays emitted from the source pass through the body and are picked up by the detectors placed on the opposite side. Both the X-ray source and the detectors rotate together around the patient to obtain the 2D X-ray image of each slice [13]. CT imaging has a high spatial resolution (~1mm) and is capable of discriminating different soft tissues. The major drawback of CT imaging is its ionizing nature. To avoid unwanted damage due to exposure to ionizing radiation, patients are entitled to be exposed to a limited total radiation dose per year [13]. For this reason, CT is used for diagnosis, verification of the tumor location, and follow-up, but it cannot be used for real-time monitoring.

Magnetic resonance imaging (MRI)

MRI is a non-ionizing imaging technique that is capable of providing full three-dimensional images of the patient. MRI signals arise from the precession of protons of water molecules inside the body around an applied static magnetic field. Different contrasts between soft tissues could be acquired, varying the frequency and phase parameters of the MRI acquiring sequences [13]. MRI exhibits outstanding sensibility in discriminating between different soft tissues and has a high spatial resolution (~1mm). However, the temporal resolution of MRI is much slower than CT, and each scan takes 3-10mins. Therefore, MRI is more susceptible to patients' movement. The static magnetic field will attract metallic objects, thus creating a safety hazard for patients with external implants devices [14]. Moreover, the presence of different electromagnetic fields at different frequencies (static magnetic field, gradients, radiofrequency field) poses issues in terms of compatibility when pairing with other electromagnetic (EM)

devices. Additionally, its high cost and bulky size make it hardly chosen as the imaging modality for the real-time monitoring of the procedure. Currently, MRI is mainly used in the procedure to confirm the diagnosis.

Positron emission tomography (PET)

PET is an imaging technique that is used to diagnose malignant diseases in patients. Before the PET scan, a radioactive tracer isotope is injected into the patient. The tracer is incorporated within the organ of interest by the metabolic processes and annihilated with positrons. The gamma-ray pairs emitted from the positron annihilation are detected by the detectors in the PET system. PET usually works in combination with CT adding to the precision of anatomic localization the functional imaging. It is capable of providing 3D images of the patients. The drawback of PET, besides the radioactive isotope intake, is that the radioactive tracer will not persist in a patient for a long time. Moreover, the cost of a PET scan is high.

Ultrasound imaging (US)

Ultrasound imaging is a cost-effective, non-invasive imaging modality exploiting non-ionizing radiations that is capable of providing real-time imaging of various tissues. The ultrasound images are produced through the detection of backscattering of mechanical energy reflected from the boundaries between different tissues and structures inside the body. Ultrasound is also capable of determining the blood flow velocity and direction in the vessels based on measuring the Doppler shift between the transmitted and scattered signal. The main drawback of US is the poor penetration inside hard structures like bones and low-resolution contrast between soft tissues. Its main clinical applications involve cardiology, gastroenterology, gynecology and obstetrics, otolaryngology, and hemodynamics.

In thermal ablation treatments, ultrasound is used to locate the thermal applicator in the center of the tumor. It is also used to monitor the ongoing treatment. However, water vapor generated by the high temperatures during the procedure blinds the instrument so that the monitoring capacity heavily relies on the clinician's experience and insightfulness.

Role of imaging in thermal ablation procedures

The mentioned imaging modalities play a crucial role in the framework of the thermal ablation procedures to pursue different objectives, as illustrated in Table 1-1 [5][15]:

(1) *planning*: determining whether the patients are suitable for ablation procedures, including identifying the tumor size, shape, and location relative to blood vessels, etc. Imaging techniques including CT, MRI, PET/CT, and US have been used for this purpose.

(2) *targeting*: the placement of the applicator into the tumor before the treatment procedure and the resolution of the best route to achieve such a placement; imaging modalities such as CT, MRI, and US have been used for this goal.

(3) *monitoring*: observing the evolution of the tissue in the ablated region during the procedure, determining the treatment effects based on the changes in the imaging that occurs during the ablation procedure. Imaging modalities like CT, MRI, and US can efficiently monitor the cryoablation zone. At the same time, no fully satisfying modalities have been so far exploited for heat-based ablation, such as RFA and MWA.

(4) *assessment of treatment response*: immediate assessment if the target endpoint was reached after the ablation procedure. Cone-beam CT, CT, MRI, PET, and US have been used for this aim.

(5) *follow-up*: postprocedural imaging to verify the outcome of the ablation treatment, usually after six weeks, and determine if additional ablation therapy is required. Imaging modalities such as CT, MRI, PET, and US have been used for this goal.

Table1-1 imaging modalities used for the thermal ablation procedure

Imaging purpose	**planning**	**targeting**	**monitoring**	**assessment of treatment response**	**follow-up**
Imaging modalities	CT, MRI, PET/CT, and US	CT, MRI, and US	**CT, MRI, and US can be used only for cryoablation**	Cone-beam CT, CT, PET, MRI, and US	MRI, CT, PET, and US

As it was mentioned before, it is well understood that the continuous monitoring of the evolution of the ablation zone during RF and microwave ablation procedures remains difficult. CT has the potential to provide real-time imaging during thermal ablation [16]. However, the ionizing radiation it exploits has an intrinsic cancer risk towards both the patient and the medical staff, thus making it unsuitable for the task [17]. MRI currently shows well-validated techniques for near real-time temperature monitoring for cryoablation [18], but its high cost, bulky size, and poor compatibility with the electromagnetic ablation techniques make its use as a tool to monitor the ablation process unfavorable. Finally, US has attractive features such as being portable, cost-effective, and capable of real-time imaging. However, it is difficult to monitor the ablation process because the US sensor is blinded by the hyper-echogenic cloud caused by water vaporization [5].

Because of the challenges among the existing imaging modalities, a new technology that can overcome all the issues would be needed. In this respect, a novel imaging modality has been proposed recently: microwave imaging (MWI) [19]. Microwave imaging is portable, low-cost, uses non-ionizing radiation, and is capable of real-time imaging. The technique reconstructs the map of the dielectric properties of an unknown target from the knowledge of the scattered electromagnetic field. Until today, a considerable amount of research works was dedicated to microwave imaging for biomedical applications such as breast cancer detection [20], brain stroke monitoring [21], thermal therapy monitoring [22], osteoporosis diagnosis [23].

The hypothesis at the basis of using MWI for real-time monitoring of thermal ablation procedures is related to the dielectric properties change in the liver tissue during the thermal ablation treatment. Indeed, during microwave thermal ablation, the water molecules in the ablation zone dramatically decrease due to the heating of the tissues. This results in a change in dielectric properties values in the ablated tissue as compared to the untreated one [24], which can be detected by a microwave imaging system [25].

1.4. Dissertation Overview

This dissertation consists of seven chapters. In Chapter 2, the principles of microwave imaging are discussed, and microwave imaging systems that have been developed for liver thermal ablation monitoring are reviewed. In Chapter 3, the tissue properties of the human abdomen tissues are reviewed; additionally, the measured dielectric properties of liver tissue after MWA are demonstrated. Moreover, numerical analysis on a simplified human abdomen model is performed to derive initial guidelines for the development of a microwave imaging device for monitoring thermal ablation treatments of liver tumors. In particular, the frequency band of the MWI system and the dielectric properties of a medium to optimize electromagnetic field coupling to the human body are derived. Following the initial design guidelines, Chapter 4 presents three antennas for the microwave imaging system, specifically designed to work in the conditions identified in the previous chapter. In Chapter 5, an in-silico validation of the microwave imaging system experimental set-up is performed, presenting the results of an MWI device aimed at monitoring the evolution of the ablation zone. Chapter 6 presents the prototyped implementation of the device and an initial experimental assessment. In Chapter 7, conclusions and future perspectives are discussed.

Chapter 2

State-of-the-art of Microwave Imaging Systems for Biomedical Applications

2.1. Introduction

Microwave imaging is a technique that can retrieve the location, shape, and dielectric properties of an unknown target based on measurements of a scattered electromagnetic field. Thanks to the capability of electromagnetic waves to penetrate examined bodies, MWI can achieve the aforementioned piece of information in a non-invasive and nondestructive way [26]. MWI has shown promising performance for applicability to different fields: remote sensing [27], concealed weapons detection [28], mine detection [29], etc. In particular, MWI has a high potential for future medical diagnosis thanks to its attractive features such as non-ionizing radiation, cost-effectiveness, capability of providing real-time 3D visualization [30]. Up to now, medical applications of MWI were mainly devoted to the diagnosis of breast tumors [31] or brain hemorrhages [32]. In these applications MWI detects the presence of the target (e.g., the tumor) due to the contrast of the permittivity and the conductivity often observed between different tissues according to their kind and pathological conditions (e.g., the healthy tissue and malignant tissue) [33]. In [34] an initial feasibility study of MWI for real-time monitoring of thermal ablation procedures of the liver was performed. The study had some limitations, as the used antennas, the used configuration, etc. However, the promising outcomes of the study motivate the research conducted in this thesis.

There are several challenges to address when developing microwave imaging systems for medical purposes:

- Characterization of the tissue dielectric properties at microwaves;
- The development of high-performance apparatuses for microwave imaging systems, such as antennas, RF front-end systems;
- The development of accurate and efficient imaging algorithms;
- Optimizing measurement approaches in terms of antennas number, array configurations, and frequency band.

In this chapter, the state-of-the-art microwave imaging systems are reviewed. Firstly, the basic principles of microwave imaging systems are illustrated. Then, the key elements for microwave imaging systems such as coupling medium and antennas are reviewed. Following that, the measurement approach that is adopted in microwave imaging systems is discussed. Finally, the state-of-the-art of microwave imaging systems for liver ablation monitoring is reviewed.

2.2. Microwave Imaging Principles

2.2.1. Forward and Inverse Scattering Problems

A general description of a microwave imaging system is given in Figure 2-1. In the proposed scenario, a scatterer is hosted in the region of interest (ROI) surrounded by a set of antennas acting as transmitters (TX) and receivers (RX). These antennas are located in a coupling medium that can be different from the background medium filling the ROI when no scatterer is present (unperturbed scenario). In the case of MWI system for liver ablation monitoring, the ablation zone is considered as the scatterer in Figure 2-1, and all the other tissues in the abdomen region (healthy liver, muscle, fat and skin) are considered as the background medium.

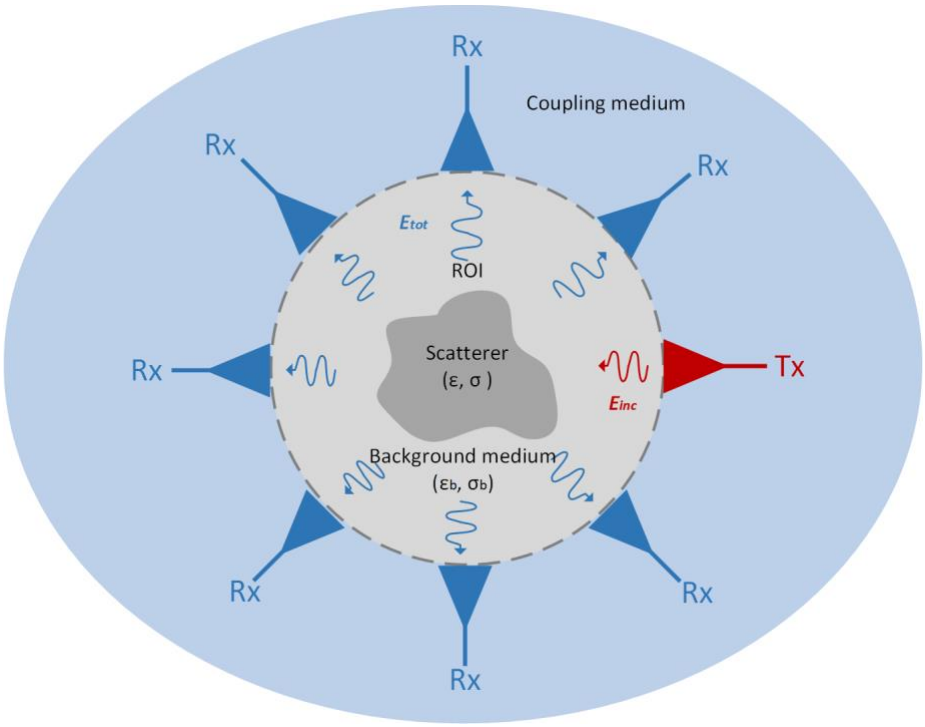

Figure 2-1 The schematic of microwave imaging systems

When the transmitting antenna illuminates the ROI in the unperturbed scenario the so-called incident field ($\underline{E}_{inc}$) is recorded by the receiving antennas. Whereas, when a scatterer whose dielectric properties (ε_s, σ_s) are different from the background medium (ε_b, σ_b) is located inside the ROI, a different field, the total field ($\underline{E}_{tot}$) is generated and recorded through the receiving antennas. The difference between the incident field and the total field is called the scattered field ($\underline{E}_{scat}$). The scattering phenomenon is described by the following equations [35]:

$$\underline{E}_{tot}(\underline{r}) = \underline{E}_{inc}(\underline{r}) + \underline{E}_{scat}(\underline{r}) \tag{2-1}$$

$$\underline{E}_{scat}(\underline{r}) = k_b^2 \int_{\Omega} \underline{E}_{tot}(\underline{r}')\chi(\underline{r}')g_i(\underline{r},\underline{r}')dr' \quad \underline{r} \notin \Omega, \underline{r} \in \Gamma \tag{2-2}$$

$$\underline{E}_{tot}(\underline{r}) = \underline{E}_{inc}(\underline{r}) + k_b^2 \int_{\Omega} \underline{E}_{tot}(\underline{r}')\chi(\underline{r}')g_i(\underline{r},\underline{r}')dr' \quad \underline{r} \in \Omega \tag{2-3}$$

where $k_b = \omega\sqrt{\mu_0\varepsilon_0\varepsilon_b}$ is the complex wave number inside the unperturbed scenario, Ω is the ROI, Γ represents the surface where the antennas are located, $g_i(\underline{r},\underline{r}')$ is the Green function in the unperturbed scenario describing the field at point $\boldsymbol{r}'$ generated by the source at point $\boldsymbol{r}$. The

function $\chi(\underline{r'})$ is the contrast function defined by the contrast between the scatterer and the background medium:

$$\chi(\underline{r'}) = \frac{\varepsilon_s(\underline{r'})}{\varepsilon_b(\underline{r'})} - 1 \tag{2-4}$$

As the region of interest is illuminated by one of the antennas, an equivalent current is induced by:

$$\underline{J}_{eq} = j\omega\varepsilon_b \, \chi \underline{E}_{tot} \tag{2-5},$$

which is the source of the scattered field.

Equations (2-1),(2-2),(2-3) are the basis of the forward and inverse scattering problems [36]. In the forward scattering problem, the goal is to compute the scattered field given the knowledge of the incident field and the scatterer. According to Hadamard's definition in [37], the forward scattering problem is well-posed. This is due to the linearity of the forward scattering problem. The solution to the problem is unique and continuous, depending on the data.

On the other hand, the inverse scattering problem is quite the opposite: it aims at retrieving the electrical properties of an unknown scatterer by solving the equations (2-2), (2-3). In this case, only the measurements of the total field and the incident field are known. Accordingly, the inverse scattering problem is non-linear and ill-posed in the sense of Hadamard, due to the lack of continuous dependence of the solution on the data [37].

Methods to deal with the ill-posed inverse scattering problem will be illustrated in detail in Chapter 5.

In microwave thermal ablation of the liver, the liver tissue dielectric properties are altered during the ablation process. This change is a function of temperature as shown in Figure 2-2. [24]. Because the ablation process creates a dielectric properties contrast between the ablated liver and the untreated liver, and such a contrast evolves during the treatment, a microwave

imaging system could take advantage of this circumstance to retrieve the changes in the permittivity of the ablated region.

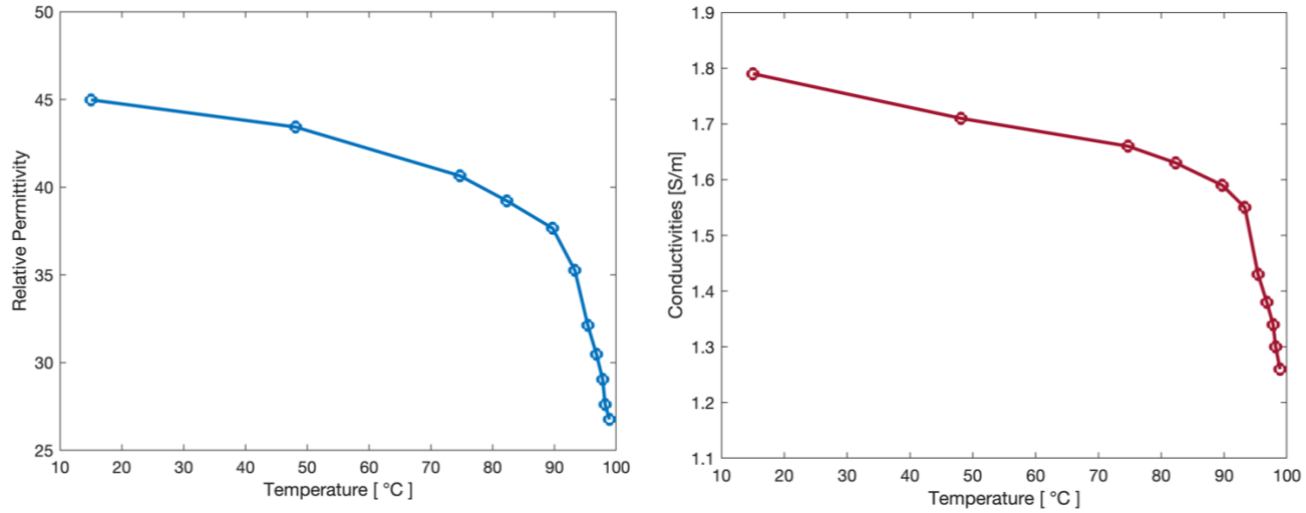

(a) (b)

Figure 2-2 Temperature dependent bovine liver tissue didelectric properties obtained at 2.45 GHz: (a) relative permittivity; (b) conductivity [24]

2.3. Microwave Imaging Apparatuses and Systems

2.3.1. Coupling Medium

One of the biggest challenges that researchers confront when it comes to microwave medical imaging system design is the penetration of the microwave field into the body. Due to the large dielectric properties difference between skin and air, instead of penetrating into the tissue, part of the electromagnetic wave is reflected at the interface between the antenna and tissue [20]. To overcome this difficulty, the majority of microwave imaging systems for medical imaging applications use high permittivity coupling media to facilitate the matching between the antenna and the tissue [20]. In addition, the utilization of a coupling medium reduces the wavelength in the unperturbed scenario to $\lambda/\sqrt{\varepsilon}$ [38]: this not only allows for an an increase of achievable spatial imaging resolution but also efficiently scales down the antenna dimension [39].

The choice of the coupling medium should take several aspects into account: constant dielectric properties across the band of interest, low-loss, physical and temporal stability, non-toxicity to humans, cost-effectiveness, and ease of realization and use. The introduction of a coupling medium into the system will bring a degree of uncertainty to the data processing because the dielectric properties of the coupling medium are forcibly frequency-dependent [38]. On the other hand, this difficulty could be overcome if taking the frequency-dependent dielectric property of the medium into account when developing the algorithms, which, however, increases their complexity [40].

Up to now, various coupling media have been used for different microwave imaging systems. Saline water, a material that is easy to acquire, is the most frequently used medium for MWI systems [41][42][43][44]. It can help provide high-resolution imaging thanks to its high permittivity. Nevertheless, the high conductivity of such material largely attenuates the electromagnetic power before it penetrates the target [45]. Ultra-sound gel, the main component of which is water, and thus has dielectric properties similar to water, has been used for breast cancer imaging [46]. Other water-soluble materials that can be used are, e.g., corn syrup [47], glycerin [48][49], triton X-100 [38], sodium metasilicate gel [50], whose dielectric properties could be tuned with water to achieve desired values. Vegetable oil [40][51][52] along with animal fat, are low conductivity materials that have been used for MWI systems [53]. Oil/water emulsion, which takes advantage of the low conductivity of oil, has a dielectric property quite constant across the typical microwave bandwidth. However, because oil is not water-soluble, this mixture is physically unstable and separates rather quickly after being prepared [54]. Acetone [55], similar to water/oil emulsion, has very low conductivity. However, it could irritate human skin, which may not be clinically safe to use. Recently, a low conductivity solid coupling medium was developed for brain stroke imaging [56][57]. In this case, the antennas are embedded inside a solid rubber and surround the head phantom like a helmet. Such a medium is physically stable, which is suitable for portable devices. The main

drawback of such a solid medium is the complex preparation process [58]. The details of several coupling media proposed in the literature and their dielectric properties are shown in Table2-1.

Table2-1 Typical coupling mediums used for microwave imaging systems

Coupling medium	**Permittivity**	**Conductivity [S/m]**	**Frequency [GHz]**	**Physical state**
Saline [42]	79	1.86	0.9	Liquid
Ultra-sound gel [46]	68	3	3	Gel
Corn syrup/water mixture [47]	44.5 @ 0.25 GHz 18.7 @ 3 GHz	0.3 @ 0.25 GHz 0.64 @ 3 GHz	0.25 - 3	Gel
Glycerin/water mixture [48]	28.0 @ 0.9 GHz	1.01 @ 0.9 GHz	0.9 - 1.3	Liquid
Triton X-100/water mixture [38]	23.130	0.335	1	Liquid
Oil-water emulsion [54]	22.9	0.07	0.915	Liquid
Acetone [55]	22.25	0.05	1	Liquid
Urethane rubber and graphite powder [56]	18.3	0.19	1	Solid
Sodium meta silicate gel [50]	16.6 @ 0.25 GHz 8.2 @ 3 GHz	0.52 @ 0.25 GHz 0.71 @ 3 GHz	0.25 - 3	Gel
Pork fat [53]	4.8	0.039	2	Solid
Soybean oil [40]	2.6	0.05	6	Liquid

2.3.2. Antennas

The antenna plays a key role in the MWI system because it dictates how the incident electromagnetic field impinges on the human body and how the scattering response from the body is gathered by the MWI system [59]. Nowadays, MWI systems for medical applications demand antennas to show wide bandwidth, have compact dimensions, and be low-cost. The design of antenna elements needs to trade-off between those factors.

2.3.2.1. Working Frequency

Several constraints lie in front of the antenna design for the MWI system. A major one is the limitation of electromagnetic spectrum availability for biomedical applications [60]. Up to now,

the majority of MWI systems for biomedical proposes works at Industrial, Scientific, and Medical (ISM) band, because unlicensed operations are permitted in these bands [61][62]. Imaging resolution is proportional to the working frequency. A higher frequency allows to reveled finer details. However, due to the lossy nature of the tissue, the electromagnetic wave attenuates severely at higher frequencies.

Apart from that, in inverse scattering, the non-linearity of the problem becomes even more pronounced as the working frequency increases. Therefore, the system is even less robust against noise on the data [63] [64].

In addition to the constraints mentioned above, studies in [65][66][67] have shown that different working frequencies and coupling media should be selected for different body regions to maximize the electromagnetic waves transmitted to the tissue. When considering the human body as a simple 1D-layered transmission line model and the incident electromagnetic field as a plane wave incident normally to the body, it is possible to easily calculate the transmission coefficient at the interface between the analyzed body region and background medium. Accordingly, a suitable working frequency range could be derived. It is found that brain imaging systems are optimized if working at a frequency around 1 GHz [38] [49] [68][69][70][71][72][73][74][75], and breast imaging systems would be best using a higher frequency range, up to 6 GHz [76][77][78][79][80][81][82][83][84][85].

2.3.2.2. Bandwidth

Bandwidth is another important design criterion of a microwave imaging system. In a time-domain system, a wideband signal is crucial because it provides higher image resolution [40]. While in the frequency domain system, both narrowband antennas and wideband antennas could be used [84][86][87][88]. The merit of wideband antennas is that they could give a degree of freedom by allowing a broad range of frequency points to be used in the MWI algorithm [89]. Generally, bowtie antennas [82][83][90], Vivaldi antennas [51][91][88][92], horn antennas [85][93][94] are the wideband antennas commonly used for microwave imaging systems.

Monopoles and customized multi-frequency narrow band patch antennas are less common but have been used for frequency-domain imaging systems [84][87].

2.3.2.3. Compactness

Most biomedical MWI systems demand compact antenna dimensions because of the limited space available to accommodate the antennas near the position of the body under test [53][84][87][88]. Therefore, it is vital to design an antenna with a compact dimension able to maintain its performance at lower frequencies. Several antenna miniaturization techniques have been investigated so far, apart from what was already mentioned in section 2.3.1. i.e., the utilization of a coupling medium. The other miniaturization techniques include introducing slots to elongate the antenna surface current path, hence increasing the antenna electrical length [95][96][97], or using high permittivity dielectric materials to scale down the wavelength of the antenna [98][99]. The usage of metasurfaces [100][101] also proved to enhance the antenna's resonance at low frequencies.

What is worth mentioning here is that those miniaturization techniques do not come at no cost. The shrink of antennas' physical size always comes together with the sacrifice of their bandwidth and Q factor [102][103].

2.3.2.4. Antenna Performances

For biomedical MWI systems, the antenna radiation pattern is less important as compared to usual applications because the measurement usually takes place in the near-field region of the antenna. Accordingly, antenna performances are evaluated in terms of antennas matching and electromagnetic field distribution in the proximity of the antenna. End-fire antennas are one of the most desirable candidates for biomedical MWI systems because they allow a high number of elements to be placed in an array configuration.

As already mentioned in section 2.3.1, many MWI systems for biomedical applications work inside a coupling medium, which could help match the electromagnetic power from the antenna to the target. However, there are challenges when it comes to the design of an antenna

that should operate inside a coupling medium: when the substrate permittivity is lower than the coupling medium, it is observed that at the higher frequencies, the direction of maximum radiation shifts from the broad-side direction. To overcome such radiation problems, a dielectric lens whose permittivity is higher than the coupling medium could be used [51][105]. The high permittivity dielectric lens at the antenna aperture also focuses the antenna radiation at higher frequencies, thus improving the antenna's radiation and penetration into the human body tissues without changing the antenna matching [51][104][105]. Other approaches such as removing a piece of substrate from the aperture side [106] and adding parasitic elements [107][108][109] also proved to be applicable.

It must be mentioned here that there are MWI systems that work in air so that they do not have to deal with such difficulties [46][68][69][77][78].

2.3.2.5. Typical Antenna candidates

Vivaldi antennas are the most widely used antennas for medical imaging systems thanks to their wideband performances and end-fire radiation pattern [67][88][92]. Because of their small aperture dimension in contact with the human body, it allows a higher number of antenna elements to be placed in an array configuration [88][92].

Horn antennas are another type of wideband antennas, which make them a good choice for MWI systems [86][93][94][98]. The drawback of horn antennas is their large aperture, which is not suitable for low-frequency applications, and rigid structure that makes an array of such antennas a quite cumbersome structure. Bowtie antennas, in the form of planar bi-conical antennas, have the advantages of wideband, low profile, and ease of fabrication. Those merits make them a good choice for a cost-effective system [82][83][110]

Monopoles, as well as dipoles antennas, are popular candidates used by the first prototypes of medical imaging systems because they have omnidirectional radiation patterns in the azimuth plane and can be effectively modeled as a line source in a 2-D imaging problem [42].

Usually, they are used for applications where narrowband operations are considered, and wide beam-width is preferred [41][44].

When aiming at a portable imaging system, patch antennas are preferable candidates because of their planar shape, which can be easily integrated into a wearable device. Typical examples include triangular patch antennas [68][72], planar monopoles [78], and coplanar waveguide antennas [111][112]. Several antennas designed for microwave imaging systems are demonstrated in Table2-2.

Table2-2 Typical antennas candidates for microwave imaging systems

Antenna type	**Bandwidth**	**Frequency range(GHz)**	**Applications**	**Dimensions (Aperture × H) (mm)**
Horn antenna [93]	Ultra-wideband	1-11	Breast imaging	25×20×13
Patch antenna [84]	Narrow-band	1.36,1.74,2.38, 3.03	Breast imaging	32×33×3
Vivaldi antenna [88]	Ultra-wideband	0.5-3	Breast imaging	30×0.5×36
Bowtie antenna [110]	Ultra-wideband	0.45-1.45	General-purpose	50×50×1.27
Patch antennas [68]	Ultra-wideband	0.857–1.493	Brain imaging	40×46×14
Monopole antenna [44]	Narrow-band	0.3-1	Bone imaging	34×2.3

2.3.3. Measurement Approach

As mentioned earlier, the measurement approach adopted to measure the scattered field greatly influences the performances of the MWI system [30]. Intending to harness the untapped potential of a microwave imaging system, one should find the optimal measurement approach, i.e., the number of antennas used by the system and the way to arrange the array. An optimal measurement approach aims at a fast and accurate measurement of the scattered field. In

particular, the goal is to use as few antenna elements as possible while gathering the largest part of the available information as possible [113].

2.3.3.1. Measurement Configuration

Three main measurement configurations are mostly used for MWI imaging systems. One is the mono-static configuration: the same antenna acts both as the transmitting and receiving antenna. In this arrangement, the antenna moves around the region of interest (ROI). Such a single-element configuration avoids the mutual coupling between antennas. It is often used for cost-effective systems [34][70][114]. The drawback of such a configuration is that the measurement time is relatively long due to the mechanical movements of the antenna. Besides, only a very limited amount of data is collected in this way, making it difficult to achieve accurate images of the target.

An uncommon configuration is to place an antenna array around the ROI, but only one antenna is active during the measurement [115]. In this arrangement, the coaxial cable connection to the antenna is manually switched to a different antenna each time after the scattering parameter is recorded. No switching matrix or multi-port VNA is needed for such a configuration, which largely reduces the system complexity and cost.

Another widely used measurement configuration is the bi-static configuration, in which the ROI is illuminated by a transmitting antenna, and the scattered field is measured by a different receiving antenna [30]. A simple measurement system implementing this configuration could consist of only two antennas [85], a transmitting antenna that radiates the incident field, and a receiving antenna that is moved around the ROI to collect the scattered field at various positions.

A more complex configuration is the multi-static configuration, which consists of several antennas surrounding the ROI. In this configuration, each antenna acts in turn as a transmitting antenna, while all the others receive the scattered field. Accordingly, the transmitting antenna illuminates the ROI from various positions, and the scattered field is recorded by several receiving antennas. Such MWI systems could come in the form of a fixed array [49] [72] or a

rotating scheme with fewer antenna elements [79][116][117]. The multi-static configuration offers the possibility to acquire data with great spatial diversity, and it provides more information than the monostatic configurations [30]. At the same time, multi-static MWI systems bring challenges such as high computational cost, mutual coupling between antenna elements, and high system costs. When a switching matrix is used, the cross-talk between each channel during the measurement could also downgrade the system performances [30].

2.3.3.2. Number of Antennas

It is well understood that more antenna elements in a MWI system could enable acquiring more data from the ROI, leading to better images [118]. However, it should not be expected that increasing infinitely the antenna number the system performances improve. Increasing the antenna number not only increases the system complexity but also introduces more discretization errors when it comes to data processing [113]. A small error in the measured data will lead to a much larger error in the solution [119]. The study in [120] shows that it is possible to achieve the same imaging resolution with a small number of antennas if the antennas are properly arranged around the ROI. Practical considerations on the system cost and complexity as well as on the required measurement time suggest that one should aim at using the minimum number of antennas needed to collect the available information. In the framework of medical MWI, such a trade-off is dictated by the practical constraints that come from the limited space available to accommodate the antennas close to the investigated region of the body.

The existing MWI systems for medical application are found using less than 30 antennas: such as 8 antennas [49][121], 10 antennas [68][75], 12 antennas [68], 14 antennas [114], 16 antennas [77], 24 antennas [72], and 32 antennas [42][84]. One special case is the MWI system in [71][99], which used up to 177 ceramic waveguide antennas for brain imaging.

A rotation scheme can be used in the MWI system to achieve sufficient data without increasing the number of antennas in the system. For example, the MWI system in [117] is consists of 2 antennas rotating around the target. It is capable of obtaining 1296 measurements.

Similar schemes are found in [76] and [116], in which the antennas are located on a platform rotating around the target recording the measurements data.

2.4. Summary

This chapter presents the principles of microwave imaging systems. In particular, the coupling medium, antennas, and the measurement approach were discussed in detail. So far, the majority of the MWI systems have been developed for medical diagnostic applications like breast imaging and brain imaging. Microwave imaging for examining deep body parts (i.e., liver, kidney) was considered a challenging task due to the high electromagnetic power loss inside the biological tissues.

MWI systems for thermal ablation monitoring are less investigated. Recent papers report a MWI systems for thermal ablation of breast cancer in which the proposed algorithm is based on waveform reconstruction [122]. In the paper it is shown that the MWI system is capable of revealing the dimension of the ablation zone in real-time. Another MWI system for monitoring interstitial thermal therapy was numerically assessed [123]. In this work, a GPU acceleration distorted Born iterative method (DBIM) was used to provide real-time monitoring of the ablation treatment. The system was able to provide the accurate temperature map in the ROI and to estimate the time needed to reach the target temperature in the treatment region.

To examine the possibility of deploying microwave imaging for real-time monitoring of thermal ablation procedures of the liver, an initial feasibility study was performed in [34]. The results evidenced that MWI can detect the differences between pre-ablated liver and post-ablated liver. The drawback of the study is that the antennas were not specifically designed for the imaging system. Besides, the MWI system in that study is a mono-statistic system, and as such, it shows the limitations mentioned in section 2.3.3.1.

Nevertheless, the promising outcomes of those studies motivate the research in this application.

Chapter 3

3 Microwave Imaging System for Thermal Ablation Monitoring: Identification of the Design Parameters

Parts of this chapter were published as:

- [J-1] M. Wang, L. Crocco and M. Cavagnaro, "On the Design of a Microwave Imaging System to Monitor Thermal Ablation of Liver Tumors," in IEEE Journal of Electromagnetics, RF and Microwaves in Medicine and Biology. 2021.
- [C-4] M. Wang, L. Farina, L. Crocco, and M. Cavagnaro, "Changes in dielectric properties following a microwave thermal ablation procedure." 2021 International Conference on Electromagnetics in Advanced Applications, 9-13 August 2021, Honolulu, Hawaii, USA.

3.1. Introduction

In this chapter, the design parameters of the microwave imaging system for liver thermal ablation monitoring are evaluated. Such parameters include the dielectric properties of the coupling medium, as well as the optimum bandwidth of the imaging system. To this end, the interaction between the electromagnetic field and the abdomen region of the human body was studied.

A preliminary step is to study the anatomy of the human abdomen region. The abdomen region relevant for liver ablation monitoring mainly consists of four tissues: skin, fat, muscle, and liver. Since the imaging in the domain of interest is based on detecting the scattered field caused by the changes in the ablated region, which has different dielectric properties as compared to that of the background medium, the dielectric properties of the skin, fat, muscle, and liver tissue are fundamental for the task at hand, and as such, they are reviewed first. Moreover, the liver tissue properties after the MWA procedure are demonstrated.

To study the interaction of the electromagnetic field and the human abdomen, and try to derive general conclusions, the geometry was simplified, considering the complex abdomen region as a planar layered model on which a plane wave impinges with orthogonal incidence. The analysis of the proposed model allows determining the optimal working conditions in terms of working frequency band and properties of the coupling medium to be adopted for improving the matching between the probing field and the human body.

To verify the outcome of the analysis on the planar layered model, an EM simulation was carried out in the WIPL-D environment [124]. In particular, a plane wave impinging on a simple cylindrical layered structure mimicking the abdomen was simulated. The outcome of the simulation agrees with the analysis carried out on the planar layered model.

After selecting the theoretical properties of the coupling medium, a study looking for the realization of such a medium was carried out leading to a new recipe made by readily available components. The proposed medium has advantages such as stability in time, constant dielectric

properties in the frequency band of interest, non-toxicity, cost-effectiveness, and ease of fabrication. The experimental assessment of the medium proves it is feasible in practice.

3.2. Abdomen Tissue Properties

The abdomen is a chamber starting from the inferior margin of the thorax to the superior margin of the pelvis and the lower limb [125]. Within the abdomen, the liver is the largest visceral organ and is mainly in the right hypochondrium and epigastric region, extending into the left hypochondrium [125]. The liver consists of a right lobe and a left lobe, connected by the umbilical fissure and the falciform ligament [126]. Figure 3-1 shows a magnetic resonance image of the abdomen cross-section on the transverse plane [127]. It clearly indicates the location of the liver in the abdomen.

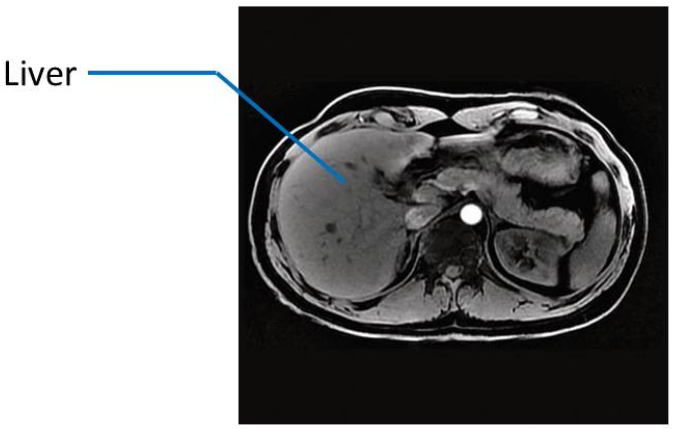

Figure 3-1 Magnetic resonance image of the abdomen cross-section [127]

The portion of the abdominal region, which is of interest for the applications at hand, mainly consists of four types of tissues, i.e., skin, fat, muscle, and liver.

The dielectric properties of the mentioned biological tissues in the frequency band of interest are approximately from 100 MHz to a few GHz [30]. It is well understood that polarization of the water molecule inside the tissue is the main contributor to the observed dielectric properties

for these frequencies [128]. The relaxation of the tissue properties can be described using a single-pole Cole-Cole model [129]:

$$\varepsilon = \varepsilon'(\omega) - j\varepsilon''(\omega) = \varepsilon_\infty + \frac{\Delta\varepsilon}{1+(j\omega\tau)^{1-\alpha}} + \frac{\sigma_i}{j\omega\varepsilon_0}, \quad (3\text{-}1)$$

where ε' is the real part of the dielectric permittivity, ε'' is the imaginary part of the dielectric permittivity, ε_∞ is the dielectric permittivity at infinite frequency, $\Delta\varepsilon$ is the magnitude of the dispersion, ω is the angular frequency, $\omega = 2\pi f$, f is the frequency, τ is the relaxation time, α is the distribution parameter, σ_i is the static ionic conductivity, and ε_0 is the permittivity of free space. The single-pole Cole-Cole parameters of the mentioned tissues are reported in Table 3-1.

Table 3-1 Single Pole Cole-Cole Parameters of Human Abdomen Tissue [129]

Cole-Cole Parameters					
Tissue	ε_∞	$\Delta\varepsilon$	$\tau[s]$	α	$\sigma_i[S/m]$
Skin	4	32	7.23e-12	0	0.0002
Fat	2.5	3	7.96e-12	0.2	0.01
Muscle	4	50	7.23e-12	0.1	0.2
Liver	4	39	8.84e-12	0.1	0.02

The dielectric properties of the four tissues in the abdomen region in the frequency range of interest are demonstrated in Figure 3-2 (a). It is found from the figure that the tissue permittivity decreases as frequency increases, while the tissue conductivities increase as frequency increases. This explains why the electromagnetic wave is lossier in the bio-tissue at higher frequencies. The electromagnetic wave penetration depth inside the tissue is demonstrated in Figure 3-2 (b). It is found that the penetration depth in the lossy tissues like skin, muscle, and liver is much shorter as compared to that in the fat. In general, penetration depth decreases inside the tissue as frequency increases. When the working frequency raises above 5 GHz, the penetration depth of skin, muscle, and liver tissue reduces to below 10 mm. This is one of the main reasons why, instead of using higher frequencies which would provide high spatial resolution, the majority of MWI systems operate at low frequencies (below 6 GHz).

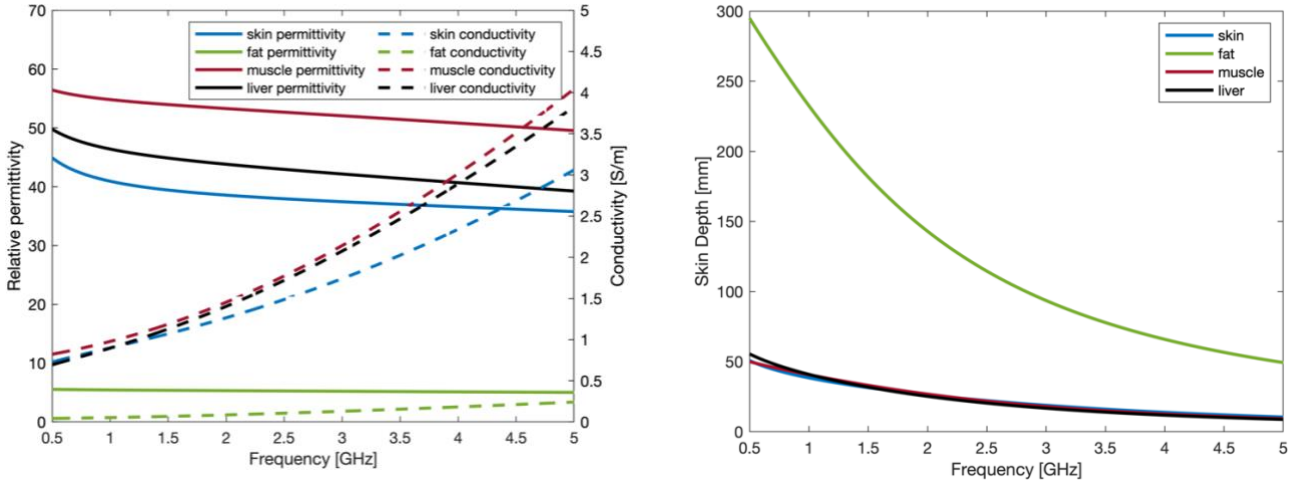

(a) (b)

Figure 3-2 (a) Human Abdomen Tissue Properties; (b) Tissue penetration depth

3.2.1. Liver Dielectric Properties After the MWA Procedure

To investigate the best MWI set-up in terms of frequency band, number of antennas, array configuration, and so on, as well as to perform numerical studies on the MWI system, accurate knowledge of the dielectric properties of tissues and of their changes as a function of the temperature and frequency must be developed. In view of this, the dielectric properties of the liver tissue after an *ex-vivo* MWA procedure were investigated.

The schematic of the MWA experimental set-up is shown in Figure 3-3, which consists of the following elements:

- Microwave power generator (Sairem SAS, France)
- Microwave ablation monopole antenna
- Semi-rigid coaxial cable (Micro-Coax Inc., Pottstown, PA, US)
- Fiber-optic temperature thermometer (Reflex Signal Conditioner, Neoptix, Inc., Quebec, Canada).
- Fiber-optic sensor (Reflex Signal Conditioner, Neoptix, Inc., Quebec, Canada).

- Peristaltic pump (DP2000, Thermo-Fisher Scientific Inc, Waltham, Massachusetts, US)
- 18°C thermostatic water bath for cooling

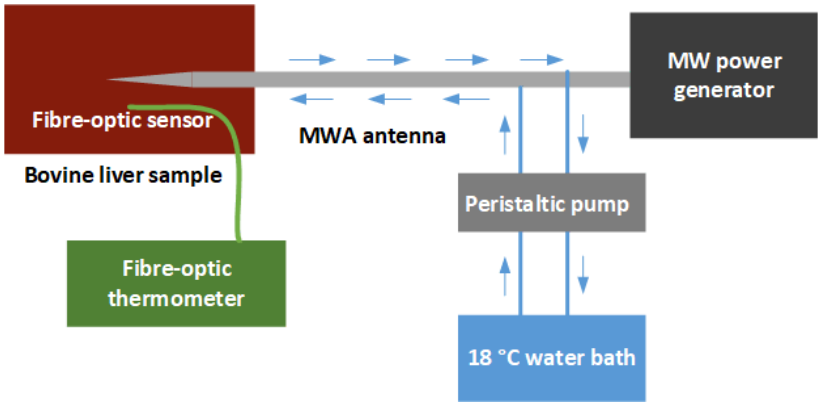

Figure 3-3 Schematic of the MTA experimental set-up

The ablation antenna used for the MWA procedure is shown in Figure 3-4 (a). It is a monopole antenna fabricated extracting 6 mm of the inner conductor of a UT-047 semi-rigid coaxial cable from the outer one (Micro-Coax Inc., Pottstown, PA, US). The length of the ablation applicator from the SMA connector to the feed-point is 20 cm. This prototype antenna is optimized to work in 18 °C cooling water at 2.45 GHz [130]. The antenna is nested in a plastic shell with two ports. During the ablation procedure, the cold water is imported from the port close to the SMA connector and circulated through the antenna tip, then exported from another port. The cooling system was driven by a peristaltic dispensing pump (DP2000, Thermo-Fisher Scientific Inc, Waltham, Massachusetts, US) which was operating at a flow rate of 50 ml/min (shown in Figure 3-4 (b)).

(a) (b)

Figure 3-4 (a) MWA antenna (b) MWA experimental set-up

The MWA experiment was carried out on five bovine liver samples. The liver was obtained from a local abattoir and ablated the same day. The liver arrived at the lab frozen (measured temperature 12 °C) so that it was brought back to room temperature (24 °C) by using a thermal water bath (154626Q, Thermo-Fisher Scientific Inc, Waltham, Massachusetts, US). The experiment settings parameters for the MWA procedure are shown in Table 3-2. Each ablation procedure had a duration of 5 minutes. The temperature of the ablated region was monitored during the ablation process with a fiber-optic temperature thermometer whose fiber-optic sensor was positioned at 10 mm from the antenna feed. After completing the ablation, the samples were let naturally return to room temperature.

Table 3-2 Experiment Settings Parameters for MWA procedure

Experiment Settings Parameters	
Ablation time	5 mins
Working frequency	2.45 GHz
Generated wave	Continues wave
Forward power	32 watts
Reflected power	2 watts
Power at antenna tip	30 watts
Water flowing rate	50 ml/mins
Water temperature	18 °C

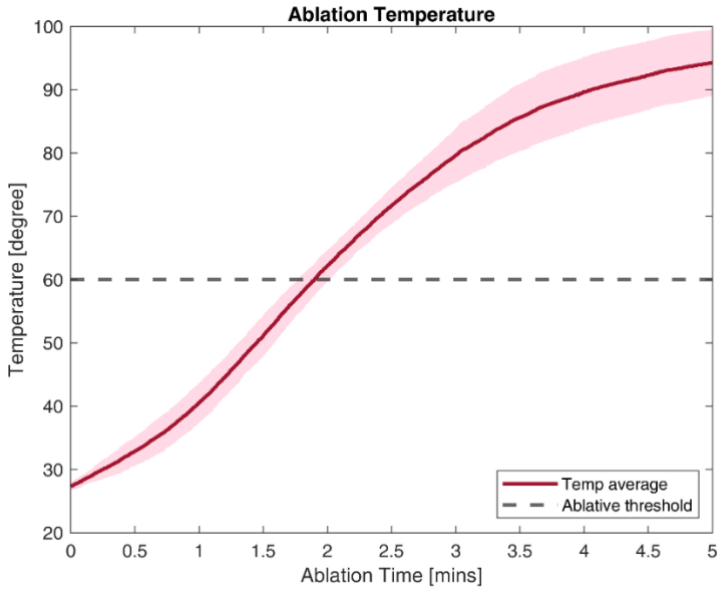

Figure 3-5 Recorded ablation temperature

The average temperature recorded by the fiber-optic sensor during the five MWA procedures is shown in Figure 3-5; the light red band shows the standard derivations of the ablation temperature. It can be seen that the temperature is around 27 °C at the beginning of the MWA and rises up to around 95 °C at the end of the procedure. The 60 °C ablative thresholds took place at about 2 mins. Figure 3-6 shows a bovine liver sample before and after the MTA procedure. It can be seen from the figure that the ablation zone shows an ellipsoidal shape. When the ablation temperature goes above 60 °C, coagulation occurs, which corresponds to the irreversibly damaged biological tissue. The thin layer of hyperemic red rim around the coagulation zone is also visible. In this experiment, no carbonized region was observed because the temperature did not exceed 100 °C during the experiment.

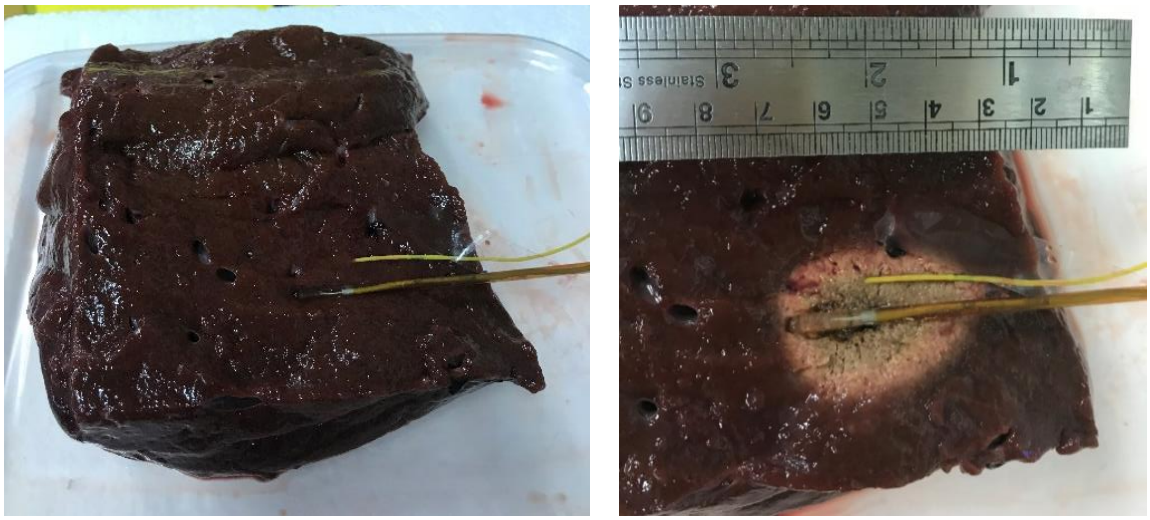

(a) (b)

Figure 3-6 Bovine liver sample (a) before the MTA procedure (b)after the MTA procedure

The dielectric properties of the liver tissue were measured with a slim form probe (Keysight 85070E) connected with a vector network analyzer (Keysight E5063A) both before and after the thermal ablation procedure. The ablation zone in each sample was measured six times, the measurement points of the ablation zone are reported in Figure 3-7. The measurement frequency range was from 0.5 - 5 GHz, and 201 frequency points were recorded.

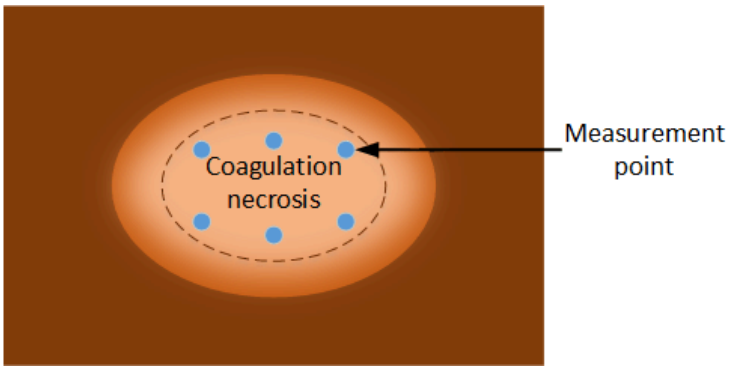

Figure 3-7 Measurement point of the ablation zone

The dielectric properties of the liver before and after the MWA procedure are shown in Figure 3-8. In the figure, the average and standard derivation of the liver tissue properties are

reported. In particular, the dark red and dark blue curves in the figure indicate the mean values of the dielectric properties measured in liver tissue (6 times from 5 samples each), while the light red and light blue bar indicate the standard derivation of the measured data. From the results, it can be seen that the permittivity of post-ablation tissue reduced as compared to the pre-ablation tissue due to the water content loss. The study only reports the tissue properties after the ablation treatment because broad band measurement results can not be aquired during the ablation process.

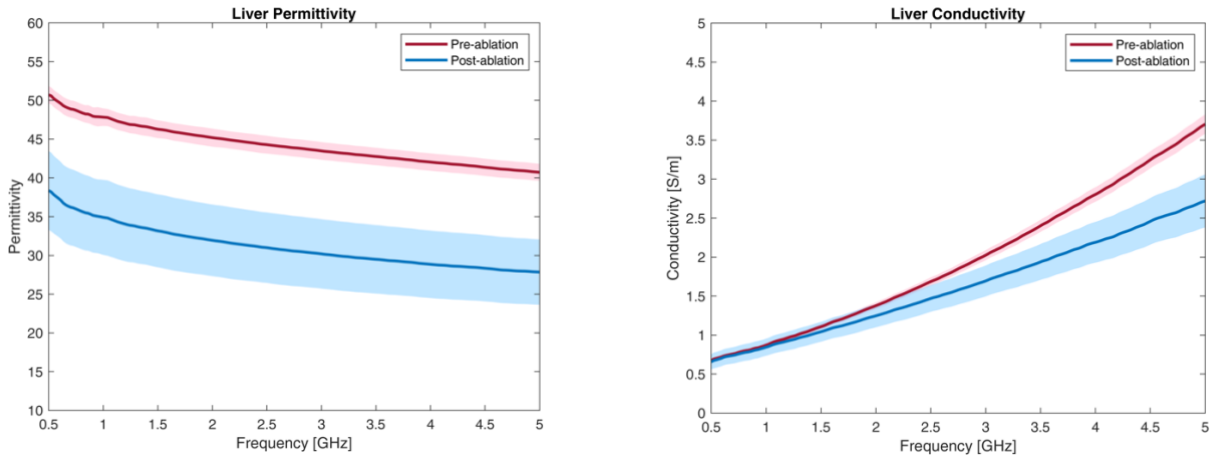

(a) (b)

Figure 3-8 (a) pre and post-ablated liver permittivity (b) pre and post-ablated liver conductivity

3.3. A Simple Model of the Abdomen

In an MWI system, the used antennas are usually located within a coupling medium, which facilitates the penetration of the electromagnetic power radiated by the antennas into the biological tissues [20]. Accordingly, the coupling medium properties and the antennas' frequency band have to be chosen in such a way that the largest possible portion of the electromagnetic (EM) power radiated by the MWI antennas enters the abdomen and provides a meaningful backscattered signal after interacting with the liver. For the sake of simplifying the problem, it is important to translate the complex anatomy structure into a simple model.

To this end, as a first-order approximation, the region of interest can be represented by a semi-infinite multi-layer planar slab, composed of skin, fat, muscle, and liver. Similarly, the EM field propagating within the coupling medium and impinging on the layered model can be represented as a plane wave traveling in the direction orthogonal to the interface between the medium and the skin. Based on average statistics [131], [132], the thickness of the skin (l_s) was taken equal to 2.3 mm, that of fat (l_f) 12.2 mm, and that of muscle (l_m) 20.2 mm. The last layer, mimicking the liver, is considered to be semi-infinite in-depth, being the target of the analysis. For the sake of simplifying the problem, as an initial investigation, this study looks only into the analysis of a 1D model based on the average statistic. The study of the patient-dependent abdomen model of different tissue thicknesses was not taken into account here. Then, the above-described layered structure exposed to the plane wave with orthogonal incidence can be conveniently studied through the formalism of transmission lines [133], as sketched in Figure 3-9.

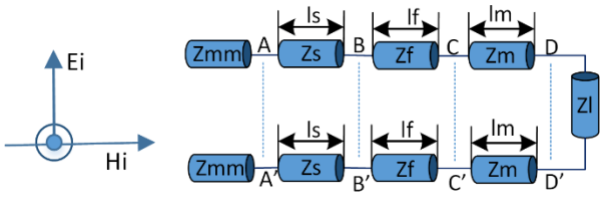

Figure 3-9 Transmission line model of a plane wave impinging orthogonally on a planar layered structure

Following the transmission line equivalence, the characteristic impedance of the line segment corresponding to the n-th tissue is given as [133]:

$$Z_n = \sqrt{\mu_0/\varepsilon_0\varepsilon_n}, \tag{3-2}$$

Where ε_n is the complex relative permittivity of the n-th tissue, as given in (3-1).

In the following, Z_{mm}, Z_s, Z_f, Z_m, and Z_l, denote the characteristic impedances of coupling medium, skin, fat, muscle, and liver, respectively. According to the impedance transfer equation, the equivalent impedance at interface CC' (Figure 3-9) between fat and muscle is [133]:

$$Z_{CC'} = Z_m \cdot \frac{Z_{DD'} + jZ_m \cdot tank_m l_m}{Z_m + jZ_{DD'} \cdot tank_m l_m}, \quad (3\text{-}3)$$

where

$$Z_{DD'} = Z_L, \quad (3\text{-}4)$$

represents the impedance of the liver. The equivalent impedance at interface BB' between skin and fat is calculated with an equation readily obtained from equation (3-3), simply substituting Z_f to Z_m, l_f to l_m, and $Z_{CC'}$ to $Z_{DD'}$. Similarly, the equivalent impedance at interface AA' between coupling medium and the skin is:

$$Z_{AA'} = Z_s \cdot \frac{Z_{BB'} + jZ_s \cdot tank_s l_s}{Z_s + jZ_{BB'} \cdot tank_s l_s}, \quad (3\text{-}5)$$

From the knowledge of $Z_{AA'}$ the reflection coefficient of the electric field at the interface between the coupling medium and skin can be finally evaluated as:

$$\Gamma_{AA'} = \frac{Z_{AA'} - Z_{mm}}{Z_{AA'} + Z_{mm}}, \quad (3\text{-}6)$$

While the transmission coefficient for the power at the interface with the coupling medium is:

$$T_{AA'} = 1 - |\Gamma_{AA'}|^2. \quad (3\text{-}7)$$

Based on the formulas above, the transmission coefficient at the interface between a generic lossless medium, with relative permittivity varying between 1 and 80, and the layered structure providing a simplified model of the abdomen was calculated in a frequency range between 500 MHz and 5 GHz. Figure 3-10 (a) shows the calculated transmission coefficient as a function of the coupling medium permittivity and frequency. The plot shows that similar to what happens in other biomedical applications [134], a 'forbidden transmission band' occurs from 2 GHz to 3 GHz, where the transmission coefficient is lower than 0.5. Such an effect arises because the layered structure is made by a low permittivity layer (fat), enclosed between two higher permittivity layers (skin and muscle, respectively), behaving like a waveguide at some frequencies [135]. Accordingly, between 2 GHz and 3 GHz less power is delivered to the target as compared to other portions of the frequency spectrum. The power transmission increases again above 3 GHz. However, the penetration depth of the EM wave severely decreases at

higher frequencies Figure 3-2 (b)), thus making it difficult if not impossible, to accurately measure useful signals. Accordingly, in the MWI system under design, it is preferable to use frequencies below 2 GHz. Following these considerations, Figure 3-10 (a) suggests that the best choice would be a frequency band of 500 MHz - 2 GHz and a coupling medium with a permittivity value between about 25 and 10. In fact, higher permittivity values show degraded performances at the low frequencies, where the penetration depth into the tissues of the human body is greater. Moreover, a high permittivity of the coupling medium means higher water content, which is usually accompanied by high conductivities. On the contrary, although lower permittivity values show better transmission at low frequencies, the 2-3.5 GHz stopband shows almost no power transmission to the target. From the above analysis, the optimal choice of the coupling medium is derived as a medium whose permittivity value is close to 23. This value is associated with a realistic medium obtained with a water-oil emulsion showing a permittivity of about 23 at 915 MHz [54]. Further more, using a coupling medium with a high permittivity value, allows to scale down the electromagnetic wavelength to $\lambda/\sqrt{\varepsilon_m}$ hence, reduceing the antenna dimention.

To verify if the unavoidable presence of losses has an effect on the previous outcomes, the transmission coefficient has been recomputed considering a coupling medium with losses. In particular, the losses associated with the medium in [54] were considered (0.07 S/m at 915 MHz). Accordingly, the 1-D transmission analysis was repeated considering a coupling medium with relative permittivity between 1 and 80 and a conductivity of 0.07 S/m. As can be seen from Figure 3-10 (b) the above-reported findings are confirmed.

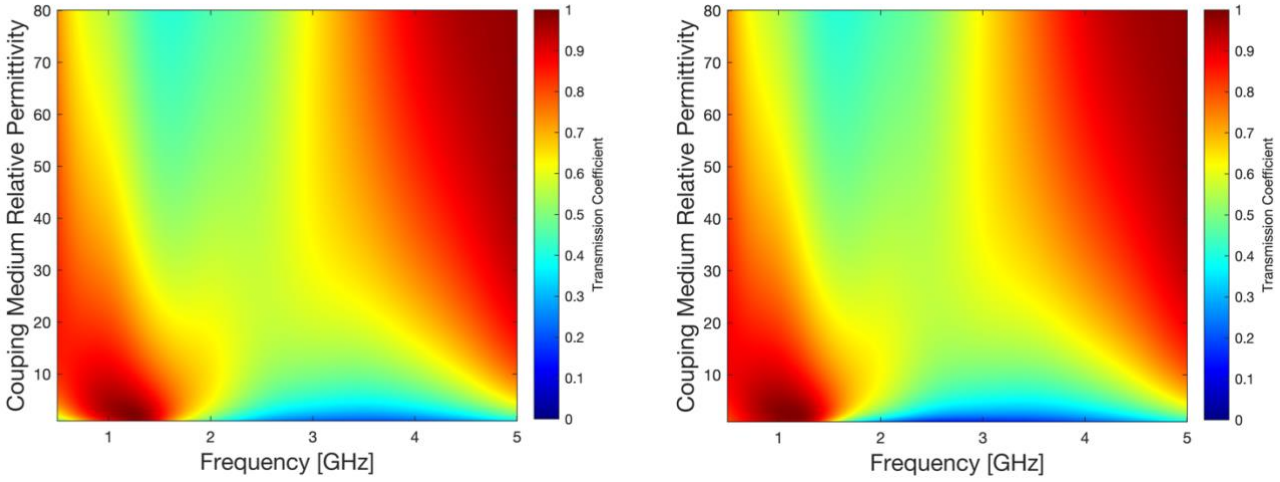

(a) (b)

Figure 3-10 Transmission coefficient for different coupling medium permittivity; (a) lossless coupling medium, (b) coupling medium with a conductivity of 0.07 S/m.

To verify whether the presence of the ablation zone would have an impact on the result of numerical analysis, the transmission coefficient was computed when a layer of ablated tissue was present. As the ablated liver is located inside the healthy liver, to this end, a 6-layered structure made by skin, fat, muscle, liver, ablated zone, and liver was modeled. The thickness of the liver layer between the muscle and ablated zone was set to 10 mm, and that of the ablated zone was 25 mm. The other tissue layers were the same as the pre-ablation model, and the coupling medium was chosen after the previous analysis used (coupling medium properties: ε_r=23, σ=0.07 S/m). The dielectric properties of the thermally ablated liver were those measured on post-ablation *ex-vivo* bovine liver (Figure 3-8) [136].

The results are shown in Figure 3-11, where a comparison of the two models, i.e., absence and presence of the ablated zone, is performed. As can be seen, at low frequencies (below 2 GHz, which is the frequency range of interest), the two curves are slightly different, even if very close values of the transmission coefficient are obtained in the two cases. Above 2 GHz, the two curves are almost overlapping, in agreement with the effect of the foreseen stopband and the significant reduction of the penetration depth of the EM field at higher frequencies. In

general, the transmission coefficients in the two scenarios exhibit similar behavior, confirming that the designed coupling medium works properly, also in the presence of the ablated tissue.

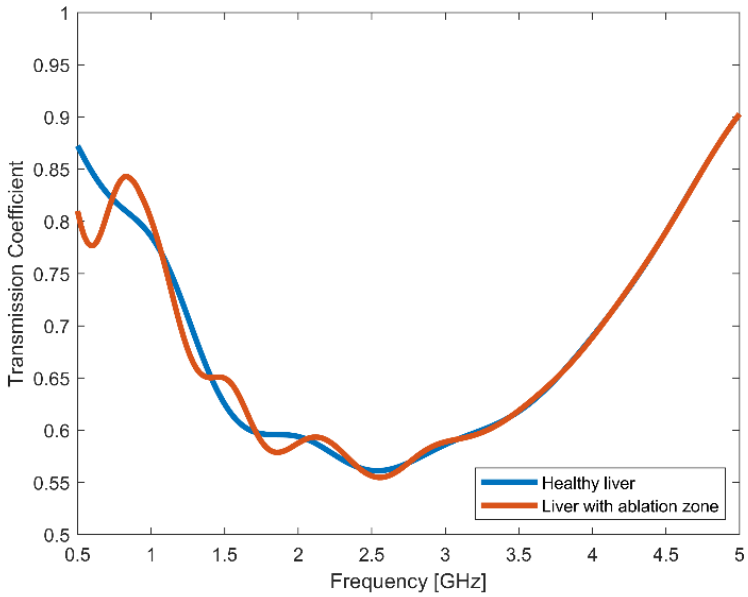

Figure 3-11 1-D transmission coefficient for a medium ε_r=23, σ=0.07 S/m comparing healthy liver or liver with a thermally ablated area 25 mm thick

3.4. Numerical Validation of the Design Guidelines

To verify the outcome of the analysis based on the 1-D transmission line model, a simulation was carried out in the WIPL-D Pro CAD environment (WIPLD d.o.o., Serbia), which is a software package for electromagnetic simulation of arbitrary 3D structures, based on the methods of moments approach [137]. In particular, a plane wave impinging on a cylindrically layered structure mimicking the abdomen was simulated (Figure 3-12). The electric field amplitude was set to 1 V/m, and the electric field polarization was parallel to the axis of the cylinder.

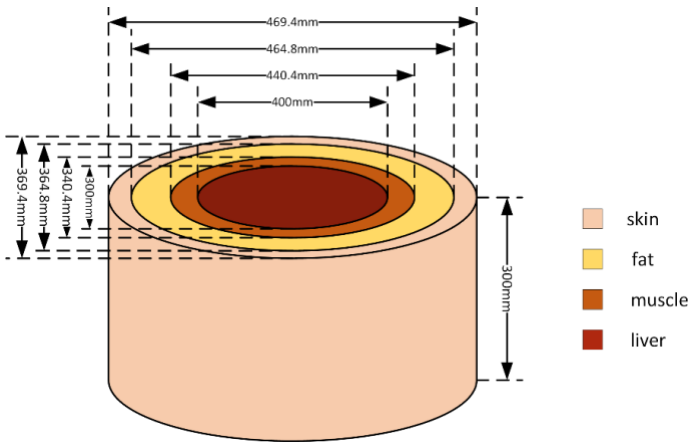

Figure 3-12 Cylindrical abdomen phantom geometry

Figure 3-13 shows the E-field distribution (unit: dBμV/m)) in the central transversal section of the phantom with respect to the height. In particular, Figure 3-13 (a) is obtained considering the phantom surrounded by air and the plane wave at 1 GHz, while Figure 3-13 (b) refers to the case in which the phantom is surrounded by a lossless coupling medium with a relative permittivity value of 23 at 1 GHz, and Figure 3-13 (c) refers the case in which the phantom is surrounded by a lossless coupling medium with a relative permittivity value of 23 at 2.5 GHz. Plots have been normalized the maximum E-field value in correspondence to the surface of the skin. Table 3-3 reports the maximum E-field absolute values in the different tissues in the three cases, normalized to the maximum value recorded in the skin in the case of air surrounding the model, at 1 GHz. From Figure 3-13 and Table 3-3, it can be noticed that at 1 GHz the field values absorbed into the phantom when the coupling medium is present are greater than when air surrounds the cylinder. In the case that the coupling medium surrounds the model, the E-field amplitude inside the liver is higher at 1 GHz than that at 2.5 GHz, as expected. The results also confirm the considerations on the lower spatial resolution expected when air surrounds the geometry. Finally, it is worth noting that field coverage looks wider when air is present. This is possibly due to surface waves traveling around the cylinder. This phenomenon is not desirable since it could give rise to scattered fields with arbitrary phases with respect to the

useful signal from the inside of the body. Accordingly, the reported results confirm that the use of the identified coupling medium and frequencies below 2 GHz is the most suitable choice.

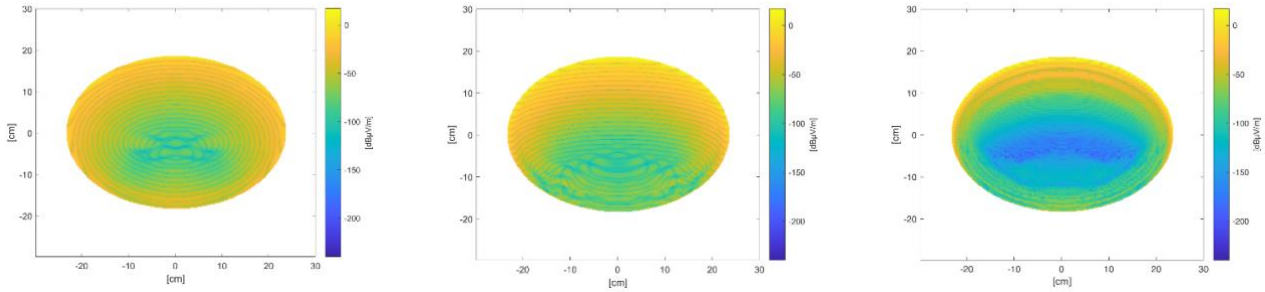

(a) (b) (c)

Figure 3-13 E-Field distribution within a cylindrical layered phantom evaluated through WIPL-D (a) phantom in free pace at 1 GHz; (b) phantom in coupling medium with permittivity value of 23 at 1 GHz; (c) phantom in coupling medium with permittivity value of 23 at 2.5 GHz

Table 3-3 Maximum E-field Normalized Value Inside Tissue

Maximum E-field Normalized Value (dBμV/m)			
Tissue	In air	In coupling medium	In coupling medium
	@ 1 GHz	@ 1 GHz	@ 2.45 GHz
Skin	0	32.0645	16.0858
Fat	-3.8641	28.0761	14.9491
Muscle	-31.1005	-1.273	-5.2039
Liver	-46.8066	-17.9472	-17.9645

3.5. Practical Realization of the Coupling Medium

After defining the theoretical dielectric properties of the coupling medium, its realization is the next step. As it was discussed in section 2.3.1, various coupling mediums have been used for MWI systems, such as saline water [41], triton X-100/water mixture [38], glycerin/water mixture [48], vegetable oil [40], oil/water emulsion [54], solid urethane rubber with graphite powder [56], etc.

The medium proposed for the microwave imaging system to monitor liver ablation should have the following features: constant dielectric properties along the frequency of interest (0.5-2 GHz), dielectric properties stable in time, non-toxicity, low cost. Moreover, the medium should be easy to make. The existing media that have been used for the other MWI systems have different constraints. The permittivity of the saline water is higher than the target value 23; the conductivity of the triton X-100 or glycerin water mixture is relatively high; the permittivity of the vegetable oil is lower than the target value; oil/water emulsion could achieve the desired dielectric properties, but the water and oil in the medium tend to separate very quickly. The solid urethane rubber with graphite powder could achieve the desired dielectric properties. However, the preparation process is complex. Regarding the mentioned difficulties, a new coupling medium is proposed here as a mixture of water, oil, dishwashing detergent, and guar gum. The recipe is improved from the oil/water emulsion in [54] by adding guar gum as a thickening agent to increase the fluid viscosity and, as such, solving the separating issue between phases of the mixture (water and oil), and thus avoiding the need for continuous circulation. The components that make the coupling medium to achieve the target permittivity of 23, are given in Table 3-4.

Table 3-4 Coupling Medium Recipe

Components	Ratio by weight
distilled water	37.80%
sunflower oil	57.84%
guar gum	0.42%
dishwashing detergent	3.94%

The preparation procedure of the coupling medium works as follows:

- Fill a container with distilled water, then smoothly sprinkle the guar gum powder on the surface of the water. Gently stir the mixture with a whisk until the guar gum powder is dissolved in the water, taking care of avoiding air bubbles during this process. If any lump remains undissolved, use a sieve to remove it.

- Add dishwashing detergent into the solution and gently mix it.
- Add the sunflower oil into the mixture and stir it until all ingredients are well incorporated.

The dielectric properties of the coupling medium were measured with the open-ended coaxial probe technique, using the Keysight high-temperature probe (Keysight 85070E) connected to a vector network analyzer (P5002A Keysight Streamline, 9 kHz to 9 GHz). The measurement uncertainty of the system is 5%. 201 frequency points were measured from 500 MHz to 5 GHz. To verify whether the coupling medium's dielectric properties were stable in time, the medium was measured three times in a one-week observation time. The first measurement (day 0) was performed right after the preparation of the coupling medium. The second measurement was performed 24 hours (day 1) after the first measurement, and the third measurement was performed 7 days (day 7) after the first measurement.

Figure 3-14 Measurement experimental set-up

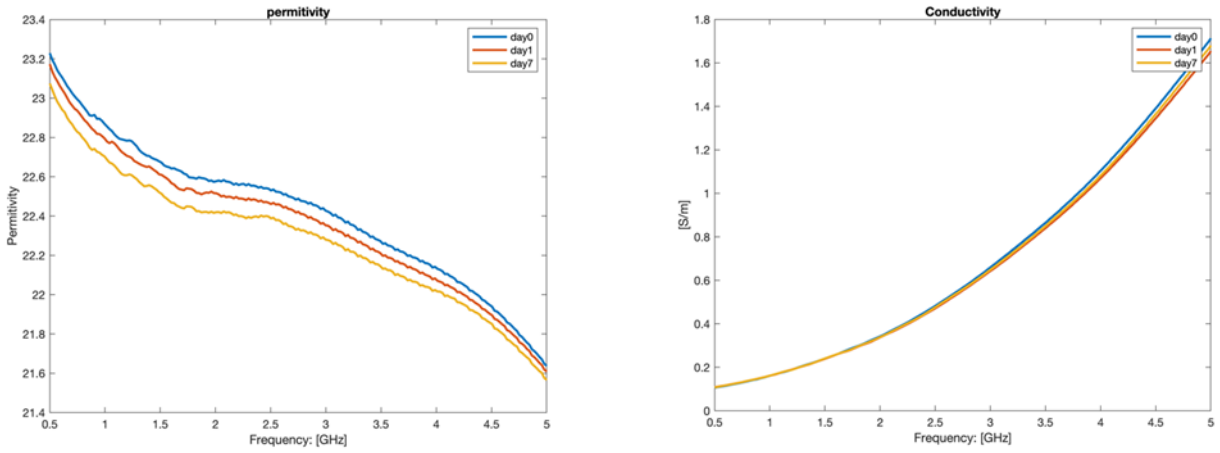

(a) (b)

Figure 3-15 Dielectric properties of the coupling medium (a) permittivity (b) conductivity

Figure 3-14 shows the experimental set-up used to measure the dielectric properties of the coupling medium. Figure 3-15 (a) and (b) demonstrates the properties measured right after the realization of the mixture and one day and 7 days after. It is found that in the frequency band of interest, the relative permittivity of the medium is close to the target value $\varepsilon_r = 23$ on day 0.

In particular, the mean values and the standard derivation of the coupling medium dielectric properties along the frequency band of 500 MHz - 5 GHz are reported in Table 3-5.

Table 3-5 Dielectric Parameters of the Coupling Medium

Relative permittivity ε_r		Conductivity σ [S/m]	
Mean	STD	Mean	STD
22.36	1.55	0.67	6.37×10^{-3}

The change in the measured values on day 1 and day 7 with respect to the values right after realization are reported in Table 3-6 as the mean difference computed from 500 MHz to 5 GHz. From the table, it is found that the variation is below 2%, so it can be stated that the coupling medium's dielectric properties are stable in a 1-week observation time.

Table 3-6 Coupling medium dielectric properties difference evaluated in one-week time

ε_r difference		σ difference	
Day 1	Day 7	Day 1	Day 7
0.27%	0.61%	1.82%	1.06%

3.6. Summary

This chapter provides the initial guidelines for the design of a microwave imaging device for monitoring thermal ablation treatments of liver tumors. In particular, the frequency band was defined, and the dielectric properties of the medium to improve coupling with the human body and in-depth detection of the target were evaluated. The 0.5-2 GHz frequency band and a coupling medium with ε_r=23 were identified as suitable working conditions. A novel coupling medium recipe was proposed and tested. The measurement results of the proposed coupling medium show that it is feasible for the microwave imaging system and stable in time.

It is worth noting that, while the presented numerical analysis is referred to a device for monitoring thermal ablation of liver tissue, which is the most clinically relevant case, the methodology is general and can be applied for the design of devices for monitoring thermal treatments (ablation or hyperthermia) in regions of the body different from the liver.

Chapter 4

4. Antennas for the Microwave Imaging System

Parts of this chapter were published as:

- [J-1] M. Wang, L. Crocco and M. Cavagnaro, "On the Design of a Microwave Imaging System to Monitor Thermal Ablation of Liver Tumors," in IEEE Journal of Electromagnetics, RF and Microwaves in Medicine and Biology. 2021.
- [C-2] M. Wang, L. Crocco and M. Cavagnaro, "Antipodal Vivaldi Antenna with Ceramic Cone Lens for Biomedical Microwave Imaging Systems," 2021 15th European Conference on Antennas and Propagation (EuCAP), 22- 26 March. 2021, pp. 1-5, Virtual Conference.

4.1. Introduction

In an MWI system, the antenna plays a crucial role because it dictates the amount of electromagnetic power transmitted to the investigated region, and it is the sensing element that receives the scattered field [59]. Therefore, antenna design for MWI systems has received substantial interest in the last two decades, and a considerable amount of research has been dedicated to this topic.

It is well understood that microwave imaging resolution can be increased either by using high frequencies or by using multiple antennas arranged in an array [113]. However, this brings difficulties to the design of antennas for biomedical applications. These antennas usually have to work in close proximity to human body tissues, wherein the electromagnetic wave attenuates severely as the frequency increases [60]. Besides, as is shown in the previous chapter, even at lower frequencies some forbidden bands can occur. This limits the portion of the electromagnetic spectrum that can be effectively used. Finally, due to the restricted body area allowed for measurement [53], it is vital to design an antenna with compact dimensions while preserving its performance at lower frequencies. Summarizing the reported considerations, biomedical MWI systems demand the antennas to be wide-band, efficient in terms of power transmission, and compact.

With reference to the optimal working conditions of an MWI system for monitoring thermal ablation described in chapter 3 (coupling medium properties ε_r=23 and working frequency band 0.5-2 GHz), in this chapter, three possible antennas are presented. The first antenna is an antipodal Vivaldi antenna using RT/duriod 6010LM as substrate [67]. Then, to improve antenna radiation when working inside the coupling medium closely to the abdomen region, an antipodal Vivaldi antenna with a cone-shaped ceramic lens is proposed [105]. The presence of the cone-shaped ceramic lens improved the antenna's radiation inside the phantom without degrading the antenna's matching or increasing the antenna's dimensions. Finally, a slot-loaded antipodal Vivaldi antenna was designed aiming at the miniaturization of antenna

dimension while still maintaining its working bandwidth at lower frequencies. Since the realized coupling medium shows some unavoidable losses, antennas' design will be carried out including the presence of a low conductivity value (about 0.07 S/m) in the coupling medium.

4.2. Antipodal Vivaldi Antenna

4.2.1. Antenna Design

The antenna in this section was designed following the steps and equations in [138]. The design was focused on taking the desirable features of the antipodal Vivaldi antenna (AVA) and translating them into the considered scenario: while the AVA in [138] is designed to work in air and in the 3-10 GHz frequency band, the AVA designed in this work operates in the coupling medium, and works in a lower frequency band, i.e., from 500 MHz up to 2 GHz.

According to the equations ruling Vivaldi antennas [138], the antenna dimensions are determined by the lowest working frequency. In the present design, to take into account the presence of the coupling medium, the equations of the original design [138] were modified as illustrated below. The antenna dimension is given by

$$W = L = \frac{c}{f_l}\sqrt{\frac{2}{\varepsilon_{mm} + \varepsilon_{sub}}} \quad (4\text{-}1)$$

where W is antenna width, L is antenna length, c is the speed of light in vacuum, f_l is the lowest working frequency, ε_{mm} is the permittivity of the coupling medium, ε_{sub} is the permittivity of the substrate.

The input microstrip line has a characteristic impedance given by [139]:

$$Z_0 = \begin{cases} \frac{60}{\sqrt{\varepsilon_e}}\ln\left(\frac{8t_s}{w_m} + \frac{w_m}{4t_s}\right) & for \frac{w_m}{t_s} \le 1 \\ \frac{120\pi}{\sqrt{\varepsilon_e}[\frac{w_m}{t_s} + 1.393 + 0.667\ln(\frac{w_m}{t_s} + 1.444)]} & for \frac{w_m}{t_s} \ge 1 \end{cases} \quad (4\text{-}2)$$

where w_m is the microstrip line width, t_s is the substrate thickness and the effective permittivity ε_e is calculated as:

$$\varepsilon_e = \frac{\varepsilon_{sub}+\varepsilon_{mm}}{2} + \frac{\varepsilon_{sub}-\varepsilon_{mm}}{2} \cdot \frac{1}{\sqrt{1+12t_s/w_m}} \quad (4\text{-}3)$$

The radiating part of the antenna is created by the intersection of two different ellipses, as shown in Figure 4-1, where the antenna substrate is transparent for the sake of clarity.

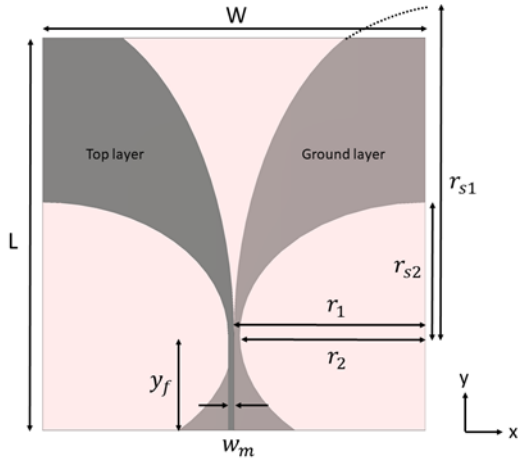

Figure 4-1 Antipodal Vivaldi Antenna (AVA-RT) geometry (gray: metallic layer, pink: antenna substrate (RT/duriod 6010LM))

The major and minor radii of the large ellipse are indicated as r_{s1} and r_1, respectively. The major and minor radii of the small ellipse are r_{s2} and r_2, respectively. They are determined by the following equations:

$$r_1 = \frac{W + w_m}{2} \quad (4\text{-}4)$$

$$r_2 = \frac{W - w_m}{2} \quad (4\text{-}5)$$

$$r_{s1} = a \cdot r_1 \quad (4\text{-}6)$$

$$r_{s2} = b \cdot r_2 \quad (4\text{-}7)$$

where a and b are optimization parameters, which are adjusted to achieve the desired performances, and w_m is the microstrip line width. Finally, y_f is the microstrip line length. Use the center of the antenna bottom line as the coordinate reference (x=0, and y=0), the center of

the small ellipse of the ground plane is: x=r_2, and y=y_f; while the center of the large ellipse is: x=r_1, and y=y_f.

The antenna was designed on the RT/duriod 6010LM substrate (Rogers Cooperation, Chandler, Arizona, USA, $\varepsilon_{sub} = 10.2$, t_s=1.905 mm), and simulated through CST software (Dassault Systèmes, Vélizy-Villacoublay, France).

Starting from the numerical values given by equation (4-1) - (4-7) for the chosen specifications, optimization was performed using the CST optimization tool on the following parameters: a, b, W, L, y_f, looking for the antenna's dimensions to achieve the best matching in the frequency band from 0.5 to 5 GHz. The antenna dimension and the optimized parameters are given in Table 4-1.

Table 4-1 Antipodal Vivaldi antenna dimension and optimization parameters

Parameters	Values [mm]	Parameters	Values [mm]
W	60	r_1	30
L	60	r_2	29.1
y_f	14.5	r_{s1}	50.1
w_m	0.9	r_{s2}	20.37
a	0.7	t_s	1.905
b	1.67		

4.2.2. Study of the Substrate Material

In MWI, the imaging resolution can be improved by increasing the number of antennas [113]. Hence, it is preferable to use compact antennas so to allow using a larger number of elements. According to equation (4-1), using high permittivity substrate materials should allow decreasing the antenna dimensions. Three types of substrates were considered, aiming to design an antenna as small as possible. In particular, RT/duriod 6010LM (Rogers Cooperation, USA, ε_{sub}=10.2), T-Ceram E-20 material (T-Ceram, S.r.o. Czechia, ε_{sub}=20.0), and T-Ceram E-37 (T-Ceram, S.r.o. Czechia, ε_{sub}=37) were considered. The thicknesses of these substrates are 1.905

mm, 2 mm, and 2 mm, respectively, plus a 17-μm-thick conductive coating. The antipodal Vivaldi antenna with RT/duriod 6010LM substrate (AVA-RT) (Figure 4-1) and the antipodal Vivaldi antenna with T-Ceram E-20 substrate (AVA-E-20) (Figure 4-2(a)) were designed following the steps and equations in section 4.2.1. The antipodal Vivaldi antenna with T-Ceram E-37 substrate (AVA-E-37) (Figure 4-2(b)) was designed applying equation (1) in [88]. In [88] the Vivaldi radiator has an exponential geometry defined as follow:

$$y_i = \pm\left(A_i e^{P_i(x-B_i)} + C_i\right), i = a, f, t. \tag{4-8}$$

The reason for implementing the design steps in [88] is that the antenna herein discussed was for biomedical microwave imaging purposes and worked in a coupling medium whose permittivity value was 25, similar to the coupling medium adopted in our study.

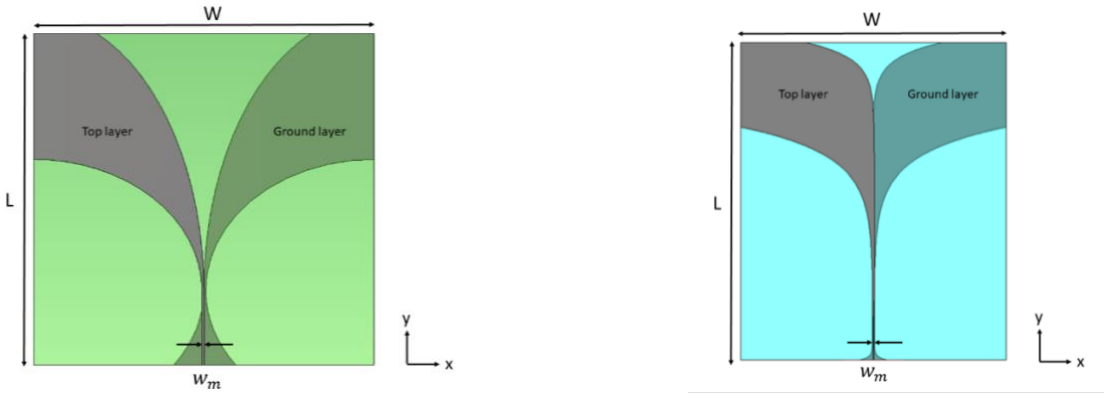

(a) (b)

Figure 4-2 Antenna geometry (a) AVA-E-20; (b) AVA-E-37 gray: metallic layer, pink: T-Ceram E-20 substrate; blue: T-Ceram E-37 substrate

The S_{11}-parameters of the antennas, when operating in the coupling medium, are shown in Figure 4-3. The designed antennas cover a frequency band from 500 MHz to 5 GHz, which is more than the required bandwidth (500 MHz - 2 GHz).

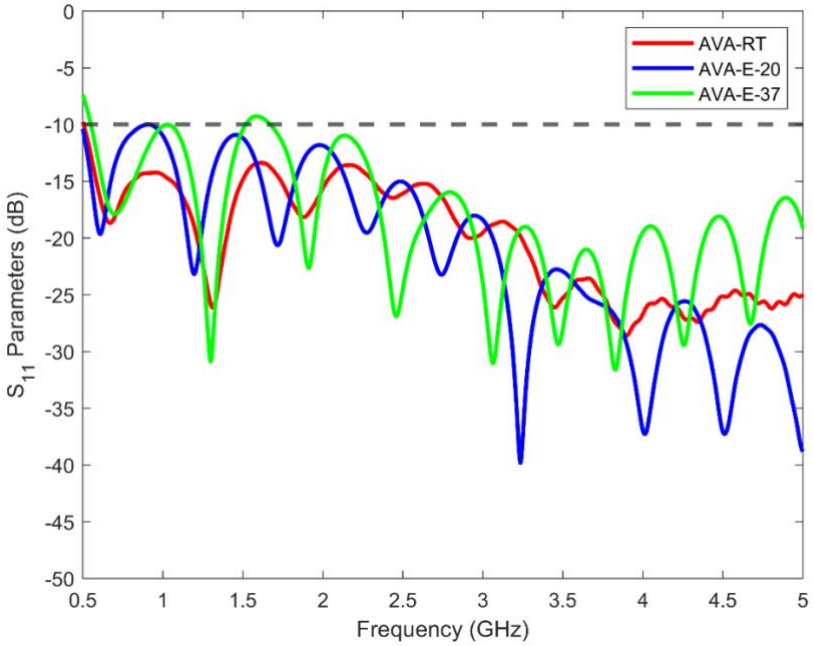

Figure 4-3 Simulated S11 parameters of Vivaldi antennas on three different substrates: RT/duriod 6010LM, T-Ceram E-20, T-Ceram E-37. The antennas are immersed in a coupling medium

Table 4-2 gives the dimensions of the antennas after the optimization process. It is found that the antenna with RT/duriod 6010LM and the one with T-Ceram E-20 substrates have the same dimensions. Even if the permittivity value of the T-Ceram E-20 substrate is higher than that of RT/duriod 6010LM, this does not correspond to a further decrease in the antenna dimension inside the coupling medium. AVA-E-37 has the most compact dimensions as compared to the other two antennas, with a 41% reduction. Because the dielectric constant of T-Ceram E-37 material is much higher than the RT/duriod 6010LM and T-Ceram E-20, the microstrip line width (t_s) of AVA-E-37 is much thinner than that of AVA-RT and AVA-E-20. Such a thin microstrip line could bring difficulty when it comes to the fabrication of the antenna.

Table 4-2 Dimensions of Vivaldi antennas on three different substrates: RT/Duroid 6010 LM, T-Ceram E-20, T-Ceram E-37

Antenna Parameters [mm]			
	AVA-RT	AVA-E-20	AVA-E-37
W	60	60	42
L	60	60	50
W×L	3600	3600	2100
w_m	0.90	0.34	0.15
t_s	1.905	2.000	2.000

The E-field distributions of the three antennas inside the coupling medium are shown in Figure 4-4. The field is given on the yz plane at 500 MHz, 1 GHz, and 2 GHz, respectively. From the figure, it is obvious that the antennas exhibit similar behaviors in these frequencies.

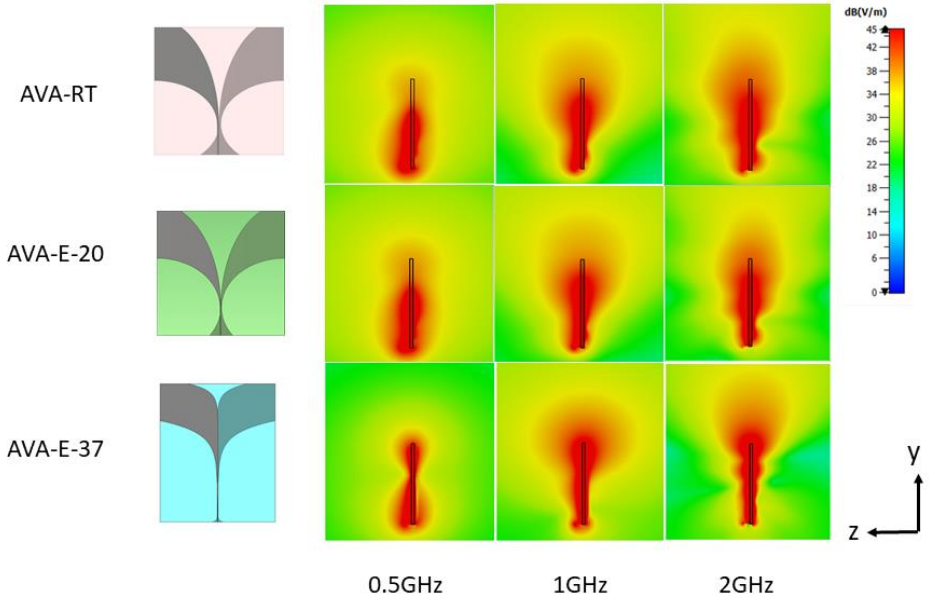

Figure 4-4 E-field distribution of Vivaldi antennas on three different substrates: RT/duriod 6010LM, T-Ceram E-20, T-Ceram E-37. The antennas are immersed in the coupling medium

4.2.3. SMA Connector Issue

In Section 4.2.2, the antennas were simulated in CST with a waveguide feeding in order to simplify the model. However, in practice, the antenna is fed by a coaxial cable through an SMA connector. It is well understood that the transition from coaxial feeding to a microstrip line feeding could cause mismatch and introduce noise [140]. To characterize this behavior, the three antennas in the previous section were simulated again by including a SMA feeding, as shown in Figure 4-5 (a).

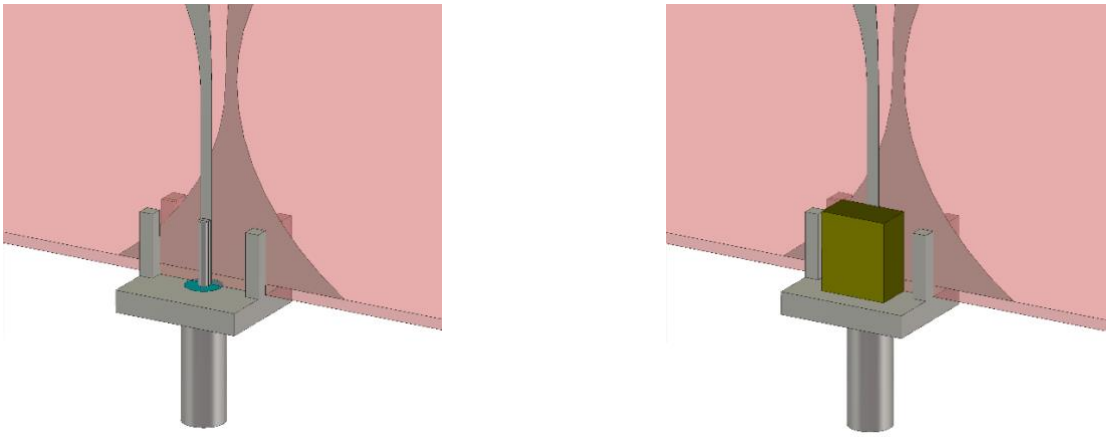

(a) (b)

Figure 4-5 Antenna feedings: (a) SMA connector and (b) SMA connector whose pin is covered with epoxy resin

Figure 4-6 shows the corresponding S_{11} parameters of the three proposed antennas (dashed lines). As can be seen, when the antennas are connected to an SMA connector and placed inside the coupling medium, they become mismatched. A possible explanation is that the SMA connector is designed to work in air. To overcome this problem, a simple solution was proposed by covering the connector pin with epoxy resin ($\varepsilon_r = 4$) which has a dimension of 4.76×5.75×2.77 mm^3 (see Figure 4-5 (b)). This allows isolating the connector pin from the coupling medium, thus avoiding the connector impedance mismatch. From the results in Figure 4-6, it can be noted that the use of the epoxy resin changes the behavior of the S-parameters for all three antennas but only provides the expected effect for the AVA-RT antenna.

Conversely, the AVA-E-20 antenna remains mismatched in the frequency range of interest (from 800 MHz to 1.8 GHz), and the AVA-E-37 remains mismatched throughout the whole frequency band. This is due to the large dielectric property difference between the substrate material and the epoxy resin. A sensitivity study was carried out with a slight variation of 1-2 mm of the epoxy resin dimension; the S_{11}-parameters of the antennas were barely changed.

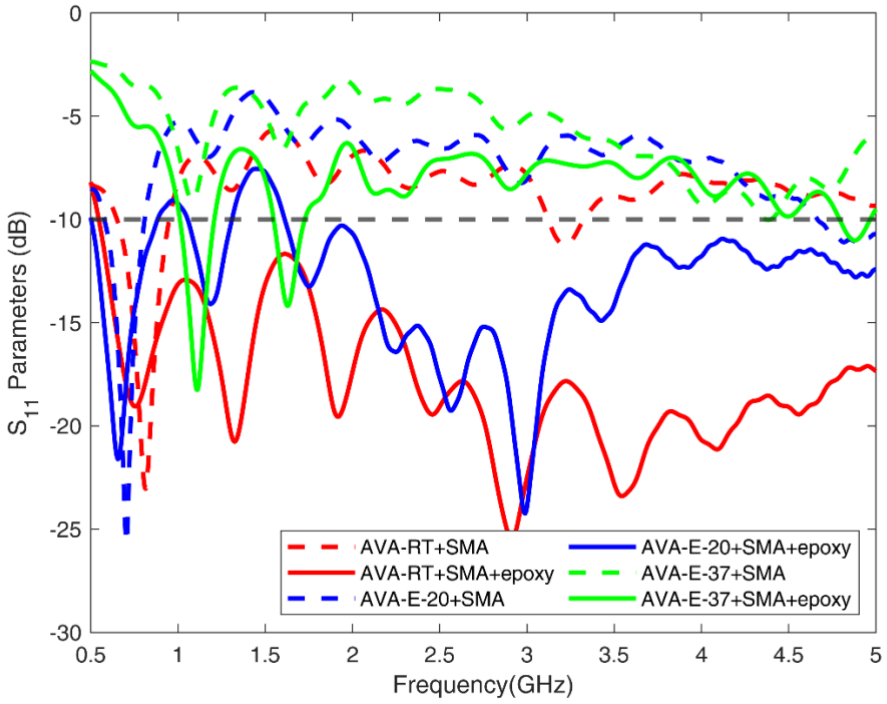

Figure 4-6 Simulated S_{11} parameters of the three antennas with different feedings

Finally, simulations were carried out to verify the antenna behavior in the presence of the human body. To this end, the AVA-RT, fed by a SMA connector and immersed in the coupling medium, was placed in contact with a 4-layer abdomen phantom made by the same tissues, with the same thicknesses, as in Section 3.2. Figure 4-7 compares the antenna's matching in the presence and in the absence of the phantom. From the figure, it can be derived that the antenna keeps the matching when the human body is present. As a further comparison, Figure 4-7 reports the S_{11} parameter of the antenna simulated when a spherical post-ablation zone is placed at the center of the phantom, 10 mm beneath the muscle-liver interface. The diameter of

the ablation zone is 25 mm, and its properties are ε_r=26.67, σ=1.26 S/m [24]. As for the case of the 1-D analysis, we can notice that the presence of the ablation zone does not change the antenna matching as compared to the healthy liver case, confirming that the designed antenna is a suitable candidate for the MWI device. Moreover, a quantitative difference can be observed in the S_{11} value in the band of interest (i.e., below 2 GHz, Figure 4-8. Such a difference represents the signal useful for imaging purposes.

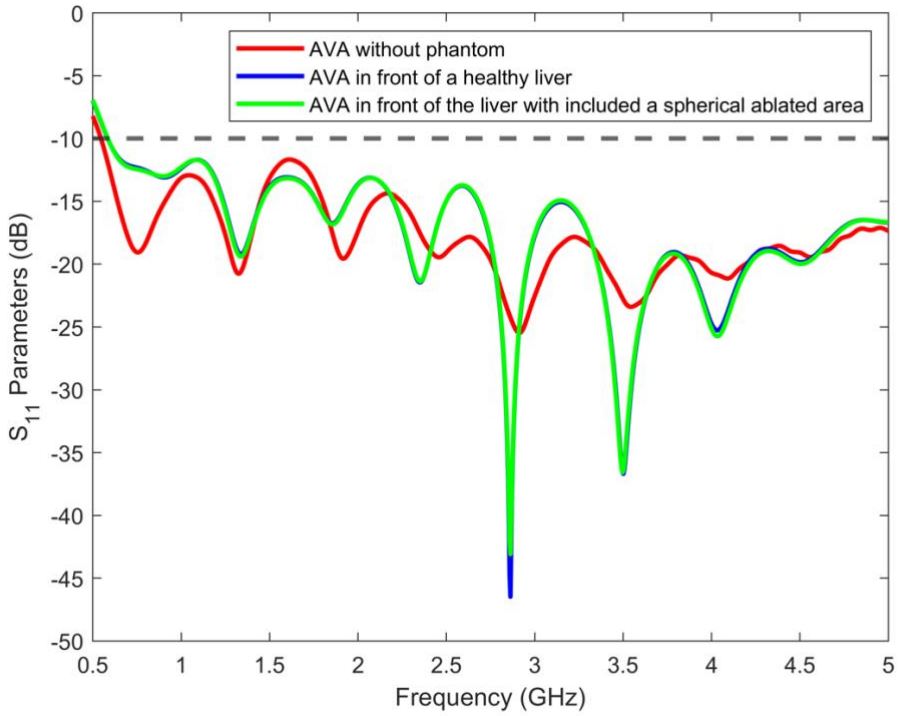

Figure 4-7 Simulated S_{11} parameters of the AVA-RT antenna fed by SMA connector and immersed in the coupling medium (ε_r=23, σ=0.07 S/m) when the antenna radiates in the coupling medium and when it is positioned in front of different abdomen phantoms

As can be noted from Figure 4-8, the differential signal between the AVA simulated with the layered abdomen phantom with and without the ablation zone varies between -50 dB and -110 dB. Such a differential signal level is above the dynamic range of a commercial VNA, indicating that such a signal can be detected.

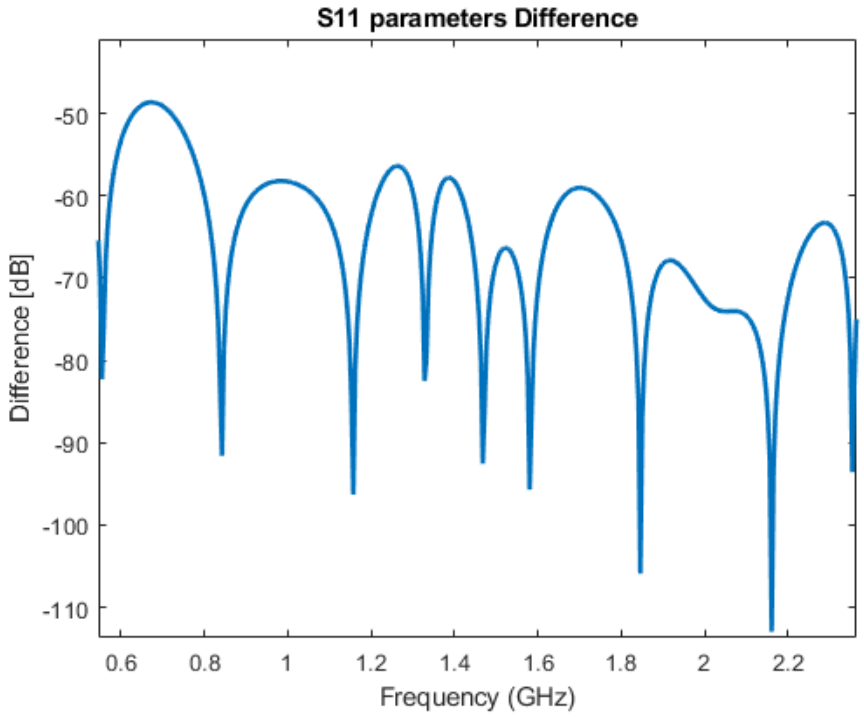

Figure 4-8 Differential signal between the S-parameters of the AVA simulated with the phantom with and without the ablation zone

4.3. Antipodal Vivaldi Antenna with Ceramic Cone Lens

4.3.1. Antenna Design

As mentioned in section 4.1, in biomedical applications antennas have to be designed to account for the performance degradation due to the lossy nature of human tissues. The antipodal Vivaldi antenna AVA-RT designed in section 4.2 fulfills all design criteria but the radiation direction shifts from the broad-side direction when it works above 3 GHz (see Figure 4-11). This is because the antenna substrate has a lower permittivity value (ε_{sub}=10.2) as compared to the background medium (ε_{mm}=23), so, when the wave leaves the substrate and enters into the coupling medium, a discontinuity of the wave phase velocity occurs, which leads to a distortion of the radiation direction [51]. Even though the optimum working

bandwidth for the MWI system was settled up to 2 GHz, it was decided to investigate this issue further.

One simple approach to solve this problem is to remove a piece of substrate from the antenna aperture [106]. This could effectively avoid the phase velocity discontinuity without complicating the antenna design. Additionally, in [51] and [104], a profiled dielectric lens inserted in the substrate hole, was able to improve the antenna radiation without changing the antenna impedance.

Following this direction, a triangular-shaped section of the substrate within the antenna's aperture was removed; the base of the triangle was d_1= 28 mm and the height h_1= 20.5 mm (Figure 4-9 (b)). To further enhance the antenna radiation, an additional antenna was studied in which the triangular substrate slot was replaced with a piece of ceramic with a permittivity higher than that of the background medium. The ceramic material used for this lens is T-Ceram E-37 (T-Ceram, S.r.o. Czechia, ε_r=37).

Two geometries of ceramic lens were suggested for improving the antenna performances: a triangular shape, whose dimensions fit into the removed part of the substrate (Figure 4-9 (c)), and a cone shape with a base radius r_{a1}=14 mm, and height h_1=20.5 mm. As compared to the antennas in [51] and [104], the ceramic cone has a symmetrical shape in the xy and the yz-planes, which could improve the antenna radiation in both planes (Figure 4-9(d)). The mentioned four antipodal Vivaldi antennas' geometries are shown in Figure 4-9, named as antipodal Vivaldi antenna with the complete RT/duriod 6010LM substrate (AVA-RT; Figure 4-9 (a)); antipodal Vivaldi antenna with a piece of substrate removed (AVA-RS; Figure 4-9 (b)); antipodal Vivaldi antenna with triangular-shaped lens (AVA-TL; Figure 4-9 (c)); antipodal Vivaldi antenna with cone-shaped lens (AVA-CL; (Figure 4-9 (d)), respectively.

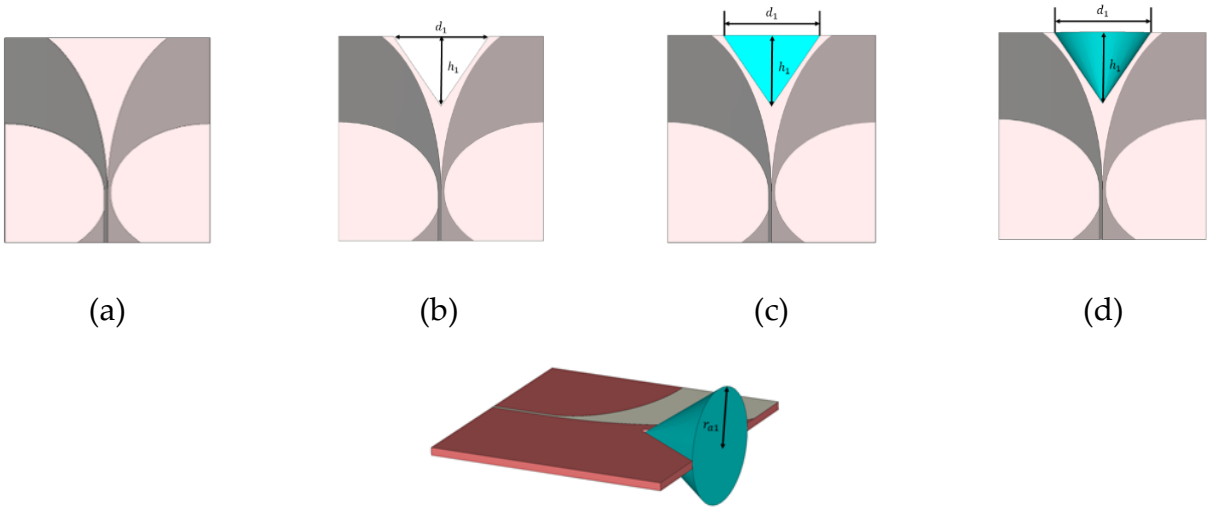

Figure 4-9 Antenna geometries (a) Antipodal Vivaldi antenna with the complete RT/duriod 6010LM substrate (AVA-RT); (b) Antipodal Vivaldi antenna with the removed substrate (AVA-RS); (c) Antipodal Vivaldi antenna with the triangular-shaped lens (AVA-TL); (d) Antipodal Vivaldi antenna with the cone-shaped lens (AVA-CL); (e) 3D view of the AVA-CL. d_1=28 mm, h_1=20.5 mm, r_{a1}=14 mm (grey: metallic part; pink: antenna substrate; blue: ceramic lens

4.3.2. Antenna Performance Comparison

The simulated S_{11} parameters of the four antennas are shown in Figure 4-10. The antennas work from 0.5 GHz to 5 GHz inside the coupling medium, with a possibility to work at a higher frequency. Despite the difference in their designs, the matching is similar. The removal of the antenna substrate and the implementation of extra ceramic materials barely changes the antenna matching.

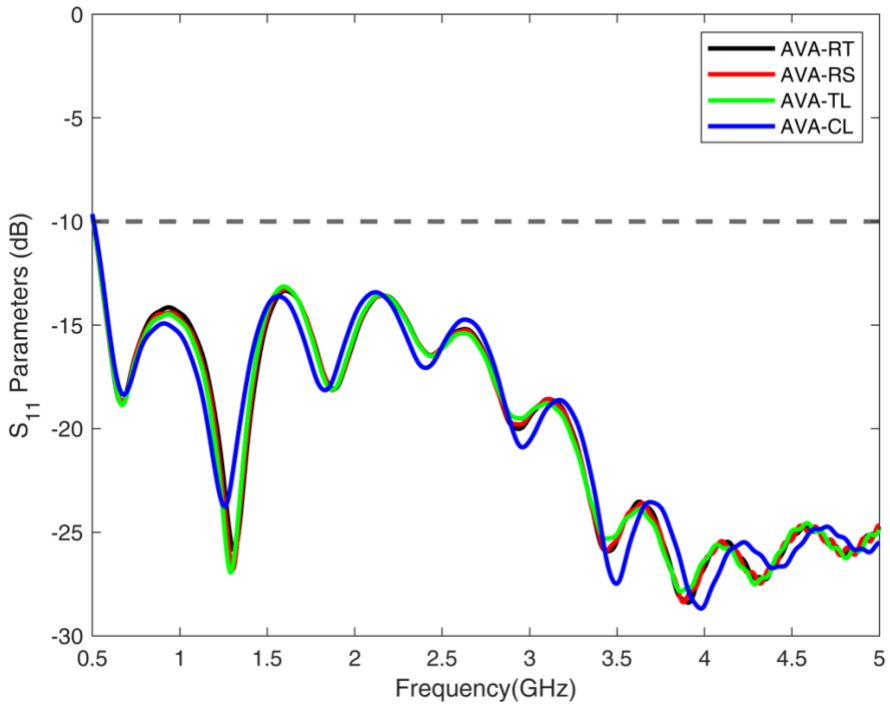

Figure 4-10 Simulated S_{11} parameters of the four AVA antennas immersed in the coupling medium: AVA-RT, AVA-RS, AVA-TL, AVA-CL

However, significant differences occur in their radiating behavior, as can be noticed from the E-field distributions shown in Figure 4-11 (a) at plane xy; (b) at plane yz. The four AVAs share similar radiation performances below 2 GHz, while as the frequency increases above 3 GHz, the direction of maximum radiation of AVA-RT shifts from the boresight, with a reduction of the radiated field on the xy-plane (Figure 4-11 (a)), especially at 5 GHz. The AVA-RS shows an improvement in the electric field at higher frequencies after removing the substrate. However, asymmetry in the radiated field in the yz-plane (Figure 4-11 (b)) is still observed above 4 GHz. The E-field of the AVA-TL shows improved radiation mainly in the yz-plane as compared to the antenna without a lens. The AVA-CL shows improved radiation above 2 GHz in both planes as compared to the other three antennas. Owing to the symmetrical shape of the cone lens, the AVA-CL shows symmetrical radiation in the xy and the yz-planes.

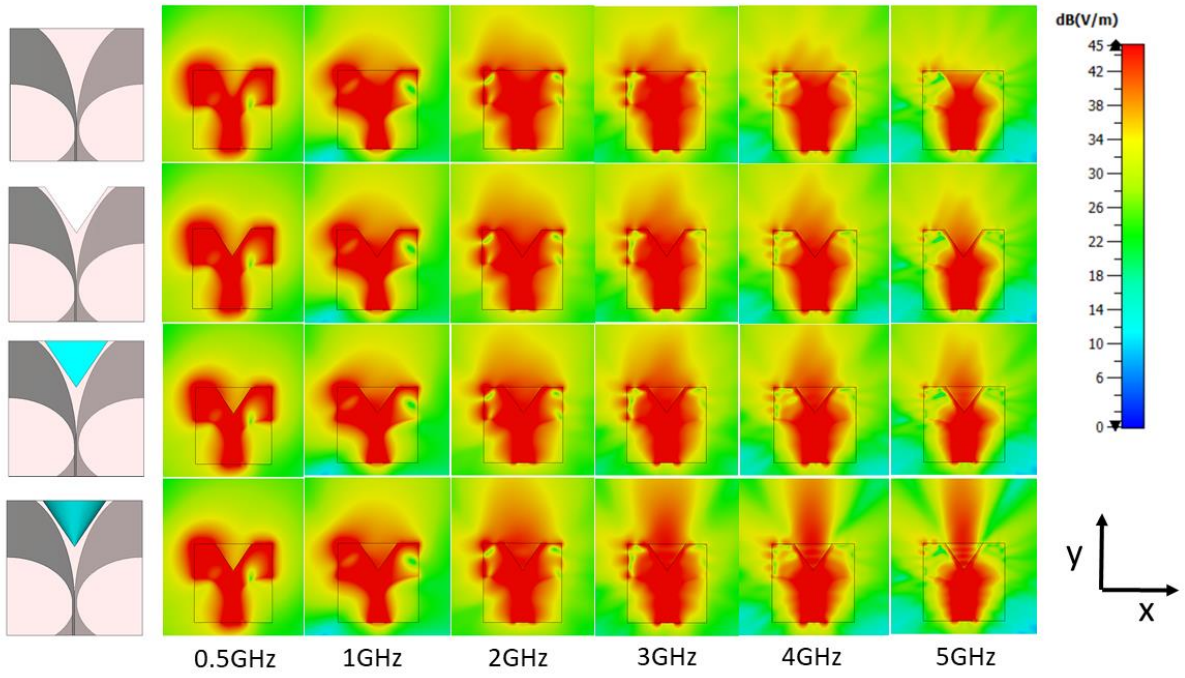

(a)

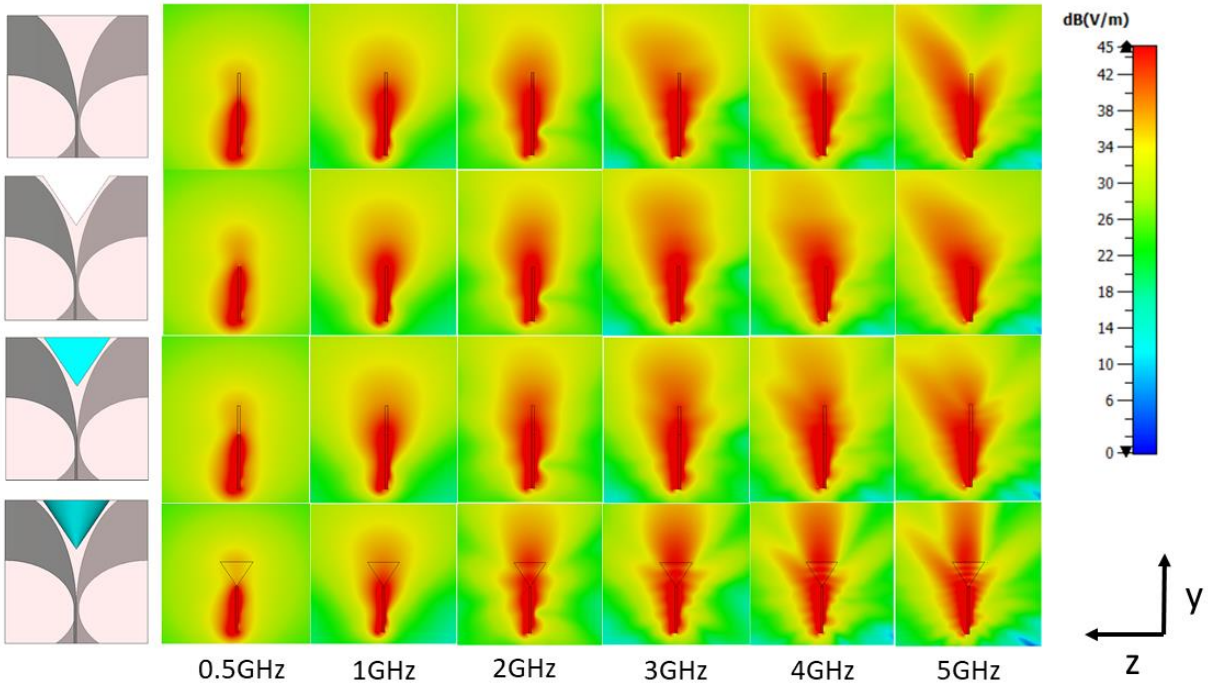

(b)

Figure 4-11 E-field distribution of the four Vivaldi antennas: (a) at xy-plane; (b) at yz-plane. From top to bottom are: AVA-RT, AVA-RS, AVA-TL, and AVA-CL. The antennas are immersed in a coupling medium (ε_r=23, σ=0.07 S/m)

Since the proposed antenna has to work close to the body, it is essential to verify the matching of the AVA-CL when located close to the abdomen region. As already discussed in section 4.2, the AVA-RT antenna proved to keep the matching when located close to a simple layered human abdomen phantom [67]. To verify the performance of the ceramic enhanced antenna, the AVA-CL has been immersed in the coupling medium and placed in contact with the same 4-layer abdomen phantom made by the same tissues, with the same thicknesses, as in Section 4.2. The simulated S_{11} parameters are demonstrated in Figure 4-12. From the figure, it can be seen that the antenna matching is slightly worsened with the presence of the abdomen phantom, but the working bandwidth remains almost the same.

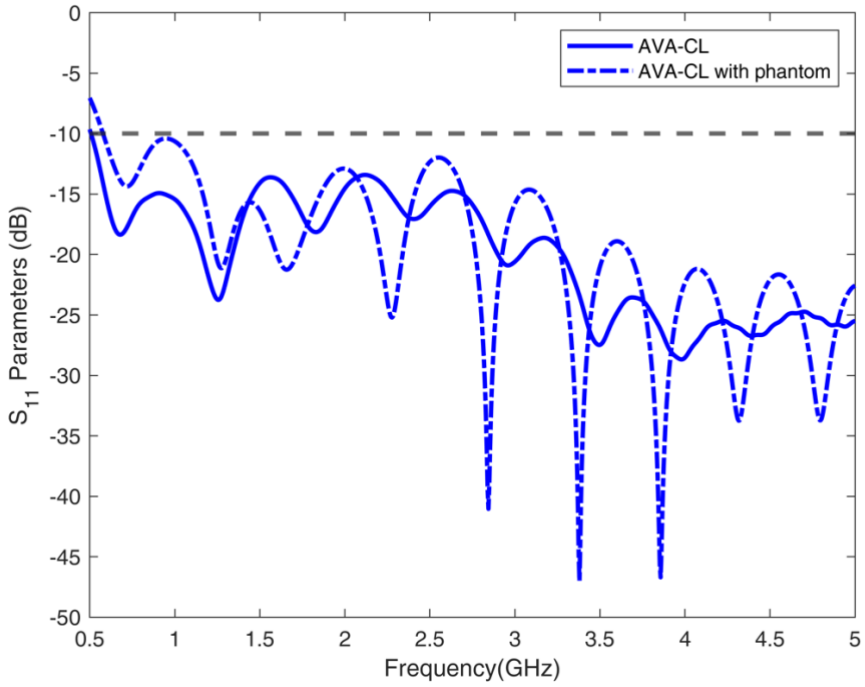

Figure 4-12 Simulated S_{11} parameters of the AVA-CL antenna immersed in the coupling medium (ε_r=23, σ=0.07 S/m) when the antenna radiates in the coupling medium and when it is positioned in front of abdomen phantoms

The E-field distribution of the AVA-RT and AVA-CL in front of the layered abdomen phantom is demonstrated in Figure 4-13. It is found that the electromagnetic penetration depth decreases inside the tissue as frequency increases. On the other hand, the presence of the

ceramic cone lens improved the antenna's radiation inside the tissue as compared to the antenna without the ceramic cone lens.

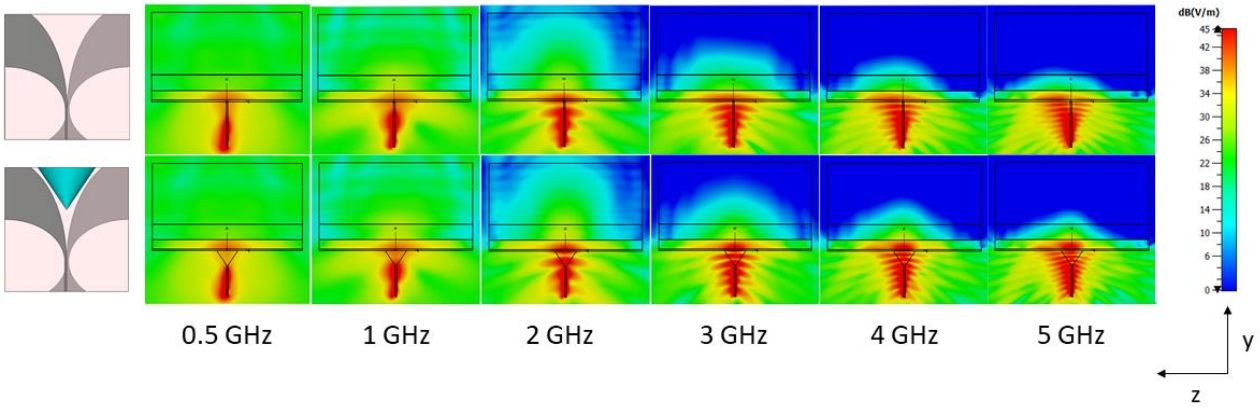

Figure 4-13 E-field distribution of the AVA-RT and AVA-CL in front of the layered abdomen phantom

4.4. Slot-loaded Antipodal Vivaldi Antenna

4.4.1. Antenna Design

As is mentioned in the introduction section, typical MWI systems exploit multiple antennas surrounding the measurement region to improve imaging resolution [113]. When designing an MWI system for monitoring liver ablation, only a limited part of the body is available for measurements. Hence, it is crucial to design an antenna with a compact dimension while maintaining its matching at low frequencies (around 500 MHz).

Section 4.2.2 investigated antenna miniaturization techniques by implementing high permittivity materials as antenna substrate. Indeed, the AVA-E-37's dimensions reduced by 41% as compared to the AVA-RT. However, the AVA-E-37 shows a mismatch issue when connecting the SMA connector and immersing it inside the coupling medium. Therefore, a study specifically aimed at antenna miniaturization techniques based on the antenna with RT/duriod 6010LM substrate is performed in this section.

The challenge of antenna miniaturization was early discussed by Hansen [141]. It is well understood that the reduction of antenna physical size always comes together with a reduction of its bandwidth and Q factor. How to scale down the antenna without degradation of its performances is an obstacle that researchers have confronted over the years. Several different antenna miniaturization techniques have been investigated so far. Among these, etching slots on the antenna's radiator proved to be an efficient way. This method could elongate the surface current path and hence increase the antenna's electrical length without increasing the antenna's overall dimension [142]. Promising studies such as [96][97] have shown that the slots on the radiator could enhance the antipodal Vivaldi antenna's lowest bandwidth without increasing its physical dimension. Besides, adding parasitic elements at the aperture side of the antenna showed improvements in the antenna radiation and enhancement of its bandwidth at low frequencies [107][143].

In this section, a slot-loaded antipodal Vivaldi antenna (SAVA) was designed aiming for the miniaturization of the AVA-RT antenna developed in section 4.2. The antenna's geometry is shown in Figure 4-14. To reduce the antenna dimensions with respect to those proposed in section 4.2, the following miniaturization techniques were applied: firstly, the antenna's width was trimmed by 20 mm (dimension Wa in Figure 4-14). This step reduced the antenna's aperture in front of the human abdomen region from 60 mm down to 40 mm. However, the reduction of the antenna's physical dimension also reduced the antenna's electrical length, hence, the antenna's lowest working frequency was shifted towards higher frequencies. To maintain the antenna's lowest working frequency as close as possible to 500 MHz, a slot was etched in the middle of the radiator and the ground plane to elongate the current path. The slot width, length, and position were not chosen arbitrarily. These parameters were selected after analyzing the influence of the different geometrical characteristics on the antenna's matching. In particular, simulations were performed with the parameter sweep function of the CST software (Dassault Systems, France) on the following parameters: R_1, R_2, D_1, D_s, θ, L_s, W_p, W_s (see Figure 4-14). The resulting antenna's dimensions are listed in

Table 4-3. In this design, due to realization availabilities, the chosen substrate is Arlon AR1000, with a relative permittivity $\varepsilon_r = 9.8$, a thickness of 1.575 mm (0.062″), and a conductive copper layer thickness equal to 0.035 mm. Despite the permittivity and thickness difference between the Arlon AR1000 and RT/duriod 6010LM substrate, the antenna matching is quite similar.

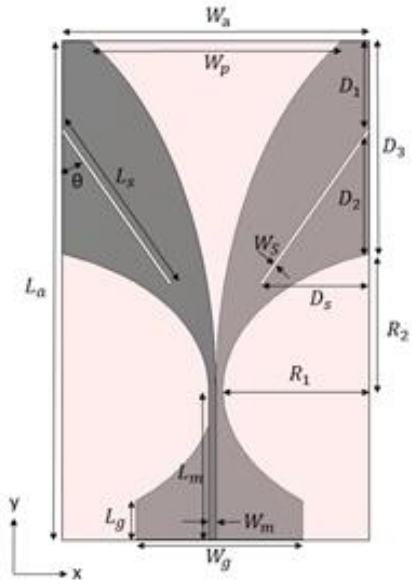

Figure 4-14 Slot-loaded antipodal Vivaldi antenna (SAVA) geometry (gray: metallic layer, pink: antenna substrate)

Table 4-3 Dimensions of the slot-loaded antipodal Vivaldi antenna

Parameter	Value [mm]	Parameter	Value [mm]
W_a	40	L_a	65
W_p	32.9	L_g	5
W_g	21.7	L_m	19.5
W_m	0.9	L_s	24.9
W_s	0.4	D_1	11.2
R_1	19.1	D_2	15.8
R_2	17.8	D_3	27.7
θ	35°	D_s	14

4.4.2. Antenna Performances

The AVA-RT and AVA-CL antennas proved to keep the matching when located close to a simple layered human abdomen phantom. To verify the performance of the SAVA, the antenna was immersed in the coupling medium and placed in contact with the same 4-layer abdomen phantom made by the same tissues, with the same thicknesses, as in Section 4.2. The simulated S_{11} parameters are demonstrated in Figure 4-15. It can be seen that the antenna matching is slightly worsened with the presence of the abdomen phantom in the frequency range from 0.75-1.75 GHz.

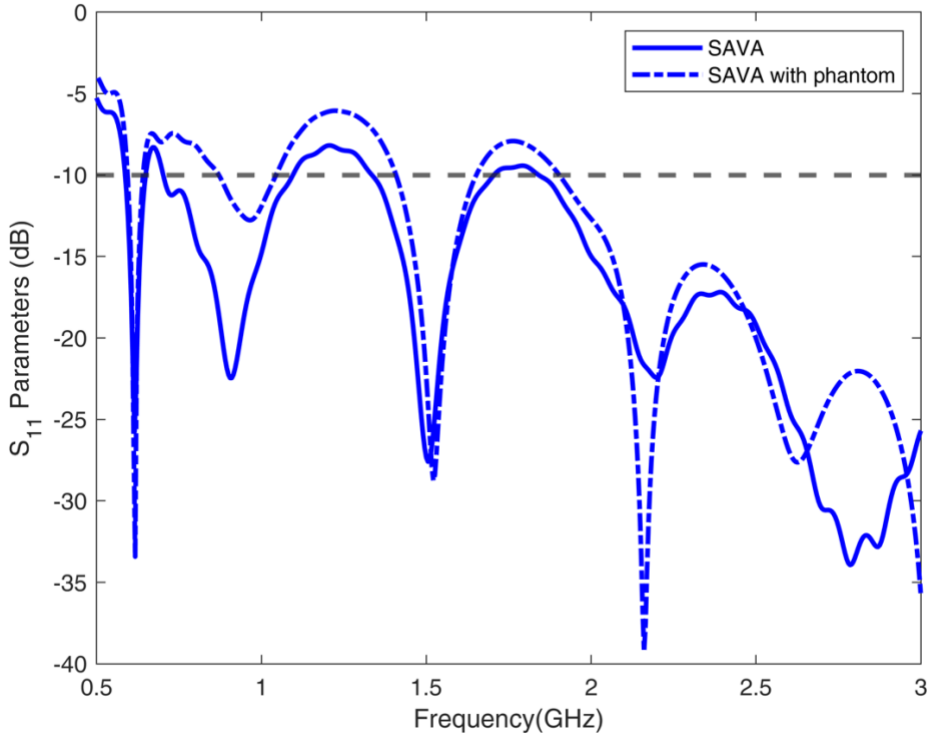

Figure 4-15 Simulated S11 parameters of the AVA-CL antenna immersed in the coupling medium (ε_r=23) when the antenna radiates in the coupling medium and when it is positioned in front of abdomen phantoms

The E-field distribution of the SAVA is shown in Figure 4-16. The up row shows the antenna in the coupling medium, and the down row shows the antenna in front of the phantom inside the matching medium. It can be seen that the E-field amplitude decreases as frequency

increases. This is due to the fact that the losses in the abdomen tissue (skin, fat, muscle, and liver) increase at higher frequencies. The electromagnetic power can only penetrate into a shallow part of the liver phantom when the frequency goes above 3 GHz but a proper coverage of the region of interest is achieved at 2GHz. This behavior confirms once again that the useful bandwidth for the MWI system is up to about 2 GHz, as derived from the analysis in section 3.4.

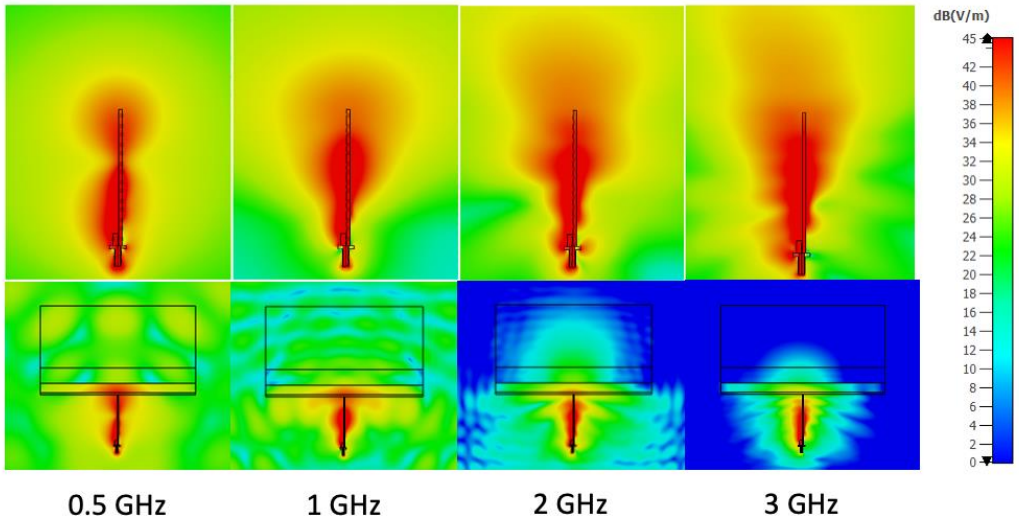

Figure 4-16 Slot-loaded antipodal Vivaldi antenna's E-field distribution

The antenna's performance was characterized in the array configuration (Figure 4-17). In particular, two SAVA were placed parallel in the coupling medium whose dielectric properties were $\varepsilon_r = 23$, $\sigma = 0.07\ S/m$. The distance between the antennas was 23mm, which corresponded to a distance larger than a quarter of the wavelength ($\lambda/4$) at 1 GHz in the coupling medium. The S-parameters of the antennas are shown in Figure 4-18. It can be seen that the antenna's lowest resonance at 600 MHz remains even with the presence of another antenna (Figure 4-18). The SAVA demonstrates a good performance towards the mutual coupling effect.

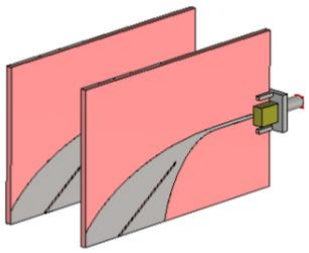

Figure 4-17 Antenna in the array configuration

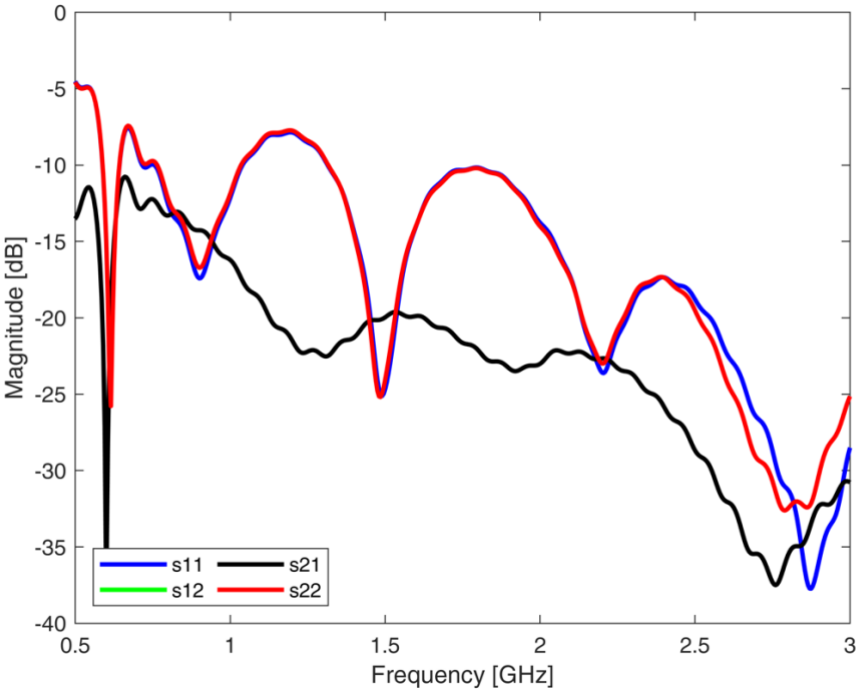

Figure 4-18 Antenna S-parameters in the array configuration

Table 4-4 shows the comparison between the antennas proposed in this chapter and some antennas adopted in other MWI medical applications. It is found that the proposed antennas offer the most compact aperture dimension as compared to other antennas working within similar bandwidth. In particular, the slot-loaded design from SAVA successfully reduced the antenna dimension by 28% as compared to the AVA-RT antenna, for this reason, this antenna was considered in the following.

Table 4-4 Antenna Comparison

Ref	Antenna type	Bandwidth [GHz]	Dimensions	Antenna type
SAVA	Vivaldi antenna	0.6-3	40×1.575×65	Liver ablation monitoring
AVA-RT	Vivaldi antenna	0.5-5	60×1.905×60	Liver ablation monitoring
[57]	Patch antenna	0.8-1.2	50×50×70	Brain imaging
[93]	Horn antenna	1-11	25×20×13	Breast imaging
[110]	Bowtie antenna	0.45-1.45	50×50×1.27	Breast imaging

4.4.3. Experimental Validation of the Antenna in the Realized Coupling Medium

This section shows the experimental validation of the SAVA. The antenna's performance was characterized both by stand-alone and in the array configuration.

The fabricated antenna is shown in Figure 4-19 (a). The antenna's matching was measured by connecting one SAVA to the vector network analyzer (P5002A Keysight Streamline, 9 kHz to 9 GHz) and placing the antenna in a container filled with the coupling medium (in section 3.5). The coupling medium was made on the same day of the experiment. The comparison between simulations and measurements results is reported in Figure 4-20, where a quite good agreement is achieved. However, above 2 GHz, a discrepancy between the simulation and the measurement result is observed, this could due to the fabrication bias of the antenna, which is more results-sensitive at higher frequencies. It is worth mentioning that the antenna was simulated in the coupling medium whose dielectric properties are those measured on day 0 in section 3.5. From the S-parameter measured in the coupling medium, a matching from 600 MHz to 3 GHz is obtained, with the possibility of working even at higher frequencies.

As it has been discussed in section 4.2.3, the antenna is experiencing a mismatching issue when fed by an SMA connector and placed inside the coupling medium. Similar to the simulation result, the same mismatching issue was observed during the antenna measurement.

This issue was fixed by applying epoxy resin to the connector pin to isolate it from the coupling medium, as is shown in Figure 4-19 (b).

(a) (b)

Figure 4-19 (a) Fabricated antenna sample; (b) SMA connector pin covered by epoxy resin

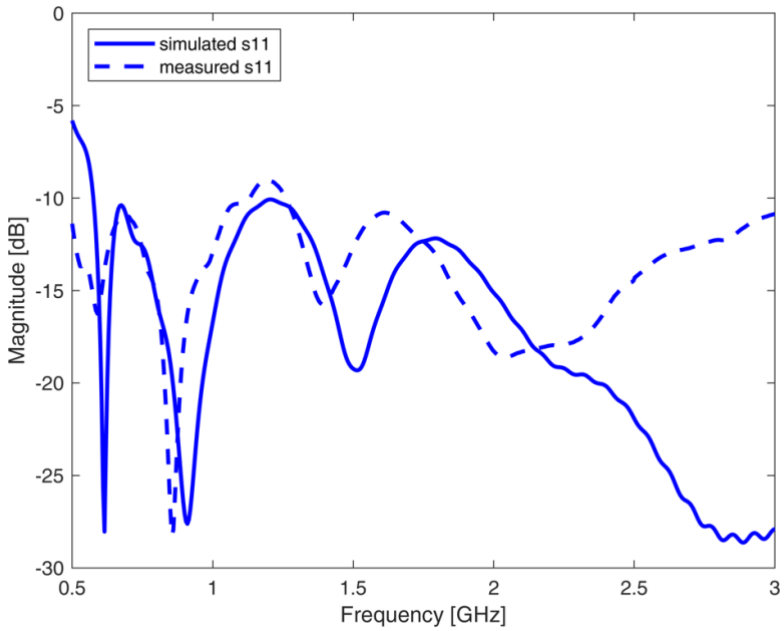

Figure 4-20 Simulated and measured S-parameter of one SAVA in the coupling medium.

The E-field distribution of the antenna placed inside the coupling medium is shown in Figure 4-21. It can be seen that the E-field amplitude decreases as frequency increases. This is due to the fact that the coupling medium is lossier at higher frequencies.

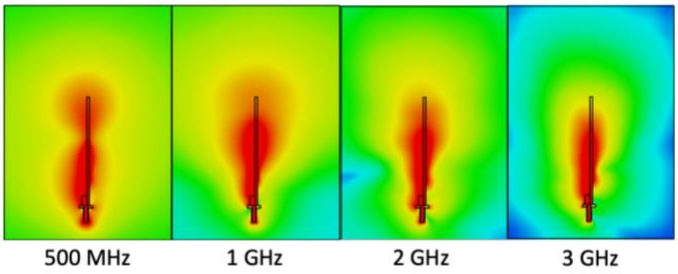

Figure 4-21 Slot-loaded antipodal Vivaldi antenna's E-field distribution in the realized coupling medium at different frequencies

In order to verify the antenna's performance in the array configuration, the antenna's matching was evaluated when placing two antennas close to each other (see Figure 4-22 (a)), which is the same as the configuration in Figure 4-17. The distance between each antenna was 23 mm, which is larger than a quarter wavelength at 1 GHz in the coupling medium. The experimental set-up is shown in Figure 4-22 (b).

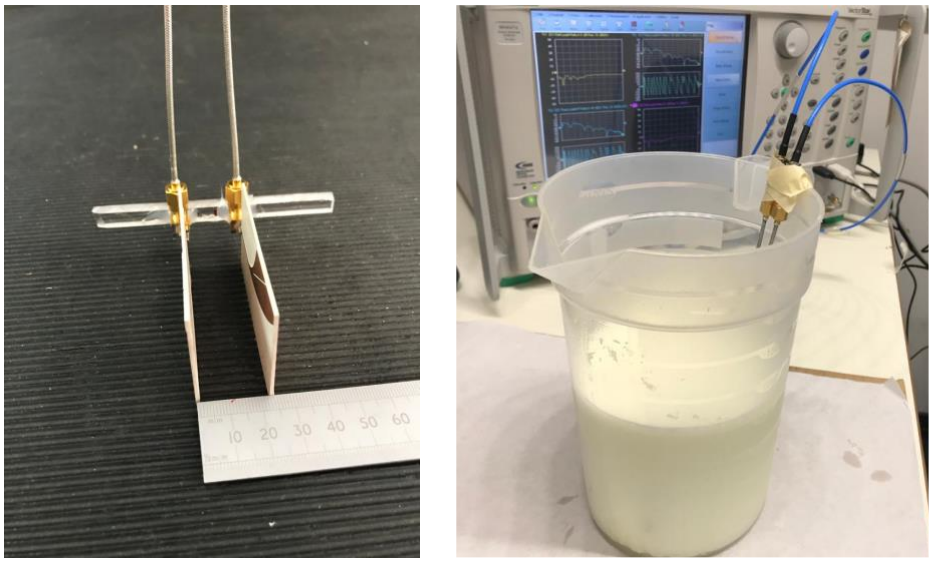

(a) (b)

Figure 4-22 (a) antenna in the array configuration (b) antenna measurement experimental set-up

The simulated and measurement result of the antenna in the array configuration is shown in Figure 4-23. It is found that the SAVA's simulation result agrees with the measurement one. It can be seen that the antenna matching at low frequency, especially around 600 MHz, remains even with the presence of another antenna. This slot-loaded antipodal Vivaldi antenna demonstrates a very good performance towards mutual coupling.

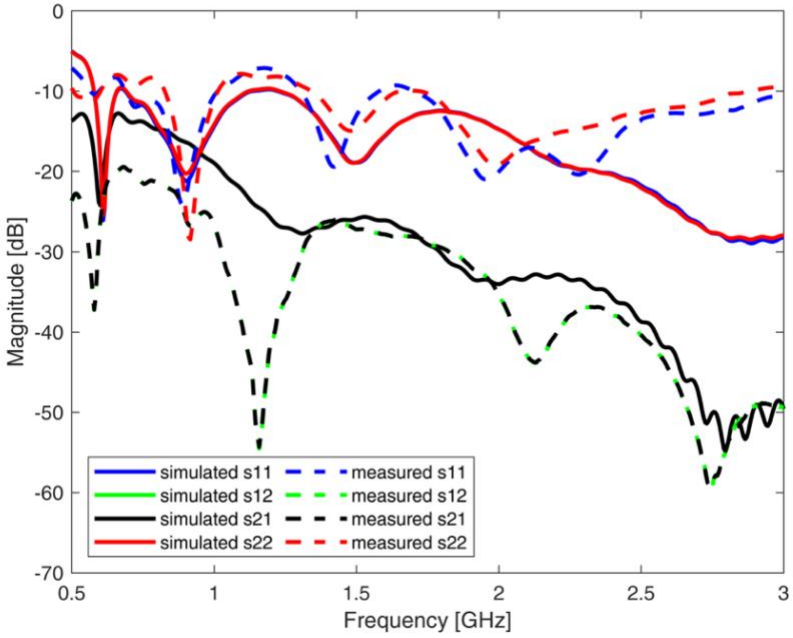

Figure 4-23 The simulation and measurement result of two SAVA in an array configuration in the coupling medium.

4.5. Summary

This chapter provides the design of three antennas for the development of a microwave imaging system for monitoring thermal ablation treatments of liver tumors. Following the optimal system working conditions given in chapter 3, the design was carried out considering the antennas located in a coupling medium whose dielectric properties are ε_r=23, σ=0.07 S/m.

An antipodal Vivaldi antenna based on RT/duriod 6010LM substrate materials (AVA-RT) was designed as the initial approach.

To increase the antenna radiation inside the tissue, a study was made introducing a high permittivity dielectric lens in the antenna aperture. The antipodal Vivaldi antenna with a cone-shaped lens (AVA-CL) shows the highest and most stable radiation from 2 to 5 GHz as compared to the other three antennas. The ceramic lens proved capable of enhancing the antenna radiation without changing the antenna matching.

Finally, with respect to the miniaturization of the AVA-RT antenna, a slot-loaded antipodal Vivaldi antenna (SAVA) was proposed. The presence of the slot proved to enhance the antenna's matching at lower frequencies without increasing its overall dimension. The simulated S-parameter showed a good matching from 600 MHz up to 3 GHz. A comparison of the SAVA and antennas' configurations from other literature showed that the SAVA has the most compact aperture dimension, and it is suitable to be arranged into the array configuration needed by a microwave imaging device for monitoring liver ablation. The SAVA is chosen as the final configuration to realize the MWI system because it is easy to fabricate and demonstrates good radiation in the 0.5-2 GHz frequency band.

Finally, the SAVA was fabricated, and the antenna's performance was characterized in the realized coupling medium. The measured S-parameter of the single antenna well agrees with the simulation results, showing a matching from 600 MHz up to 3 GHz, with the possibility to work even at a higher frequency. The antenna matching in the array configuration proves the effectiveness of the slot-loaded design by also revealing a good performance toward the mutual coupling. The good matching at low frequency is maintained even with the nearby presence of another antenna. All the above features reveal that the antenna is suitable to be arranged into the array configuration needed by a microwave imaging device for monitoring liver ablation.

Chapter 5

In-Silico Validation of the Microwave Imaging Device

Parts of this chapter was published as:

- [J-2] M. Wang, R. Scapaticci, M. Cavagnaro and L. Crocco, "Towards a Microwave Imaging System for Continuous Monitoring of Liver Tumor Ablation: Design and In Silico Validation of an Experimental Setup," Diagnostics. 2021; 11(5):866.

5.1. Introduction

This chapter presents the in-silico assessment of the MWI device for monitoring liver ablation, with the aim of evaluating its performances before the realization of the experimental setup. To this end, an imaging experiment involving eight slot-loaded Vivaldi antennas in an array configuration and a practically realizable liver phantom mimicking the evolving treatment was simulated. The antenna used in the in-silico assessment is the slot-loaded antipodal Vivaldi antenna (SAVA) that was developed in section 4.4. The antennas were placed in the coupling medium proposed and realized in section 3.5.

Since to realize a phantom for experimental assessment of the MWI system it is necessarily needed the use of materials (such as acrylonitrile butadiene styrene (ABS)) that have dielectric properties significantly different from those of the abdomen tissue, such materials could affect the evaluation of the performances of the MWI system in a non-realistic way. Accordingly, numerical simulations were herein carried out to understand the effect of the ABS shells containing tissue-mimicking materials by comparing the imaging results in the presence and absence of them.

As a result, the 3D images obtained in an experimental set-up simulating the working conditions of the considered MWI device show that even in the presence of the unavoidable measurement noise on data and without the aid of preparatory a priori information (e.g., an image of the scenario under test obtained with another imaging modality), it is possible to localize the changes occurring within the ablated region and appraise its extent in real-time. Finally, the results of the in-silico experiments also allow foreseeing in which directions the system can be improved, both in terms of hardware and processing of the data.

5.2. Microwave Imaging Device Set-up

5.2.1. Description of the Measurement Configuration

The main design guidelines for the MWI system for liver ablation monitoring were discussed in chapter 3. In particular, it was concluded that the 0.5–2 GHz frequency band and a low loss coupling medium with a permittivity value equal to $\varepsilon_r = 23$ is a good trade-off between penetration depth, imaging resolution, and antenna dimension. Then, a suitable antenna for such an MWI system was designed, the slot-loaded Vivaldi antenna (SAVA). The SAVA has a dimension of 40 × 65 mm^2 and a working frequency from 0.5 to 3 GHz, with the possibility to work even at higher frequencies. The antenna radiates a linearly polarized field and has an end-fire radiation pattern so that several radiating elements can be allocated in an array configuration.

The experimental setup proposed for the first experimental validation of the MWI system for monitoring thermal ablation of liver tissue is shown in Figure 5-1(a) (top view - projection in the y-z plane). Due to fabrication difficulties, the proposed set-up does not considers all the layers considered in the abdomen model in Chapter 3. Instead, the setup consists of a container made of acrylonitrile butadiene styrene (ABS) and has a size of 210 × 210 × 210 mm^3, (width × length × height). The container is filled with the coupling medium designed in section 3.5. Since the proposed coupling medium aimed at maximizing the EM power transmitted to the liver layer, it can be considered equivalent to the layered abdomen model consisting of skin, fat, muscle, and liver. The antenna array was inserted into the container, completely immersed into the coupling medium, and placed close to one side of the container.

In particular, the MWI device proposed in this chapter consists of an array of 8 antennas, which represents a good trade-off among system complexity, mutual coupling, and imaging capabilities. The following two measurement configurations were studied, looking for the one which could yield better results:

- One-row measurement configuration: 8 antennas placed horizontally in the same level. The distance between each antenna is 23 mm, which corresponds to a distance larger than a quarter of the wavelength ($\lambda/4$) at 1 GHz in the coupling medium (Figure 5-1(b)).
- Two-rows measurement configuration: the 8 antennas were placed in a staggered manner in two groups of 4 antennas placed on two lines. The distance between the antennas is 20 mm along the x-axis and 23 mm along the y-axis (Figure 5-1 (c)).

Finally, a phantom is located 35 mm away from the antennas array, still completely immersed in the coupling medium. In Figure 5-1, the region of interest (ROI) for the imaging system, which has a dimension of 120 mm × 102 mm × 102 mm (y-x-z), is marked.

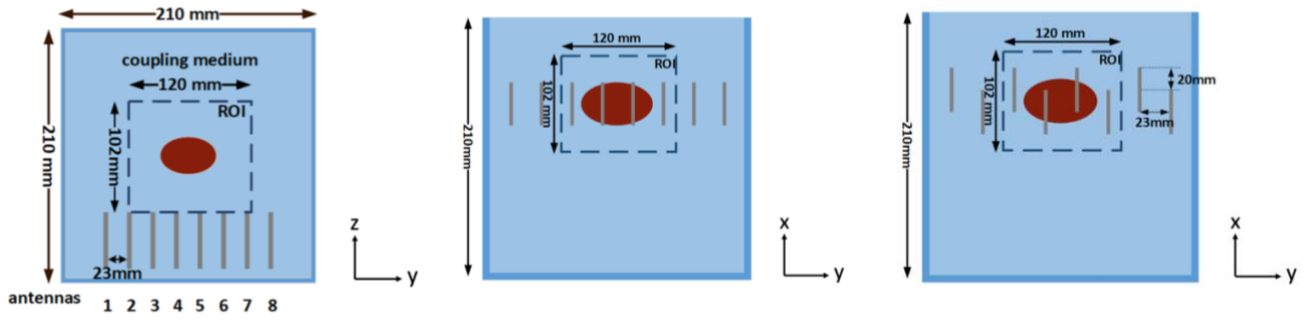

(a) (b) (c)

Figure 5-1 (a) Top view of the setup configuration; (b) side view of the one-row configuration; (c) side view of the two-rows configuration

In this MWI device, all antennas worked both as transmitters and receivers, to implement a multi-static measurement configuration in which while one of the antennas is activated, the rest of the antennas record the signals scattered by the observed region.

5.2.2. Description of the Phantom

As the ablation zone typically shows an ellipsoidal shape, a simple ellipsoidal structure was designed to mimic the thermally ablated area evolution during the ablation treatment [144]. The dimensions of the phantom were translated from the experimental results in [144], while the dielectric properties of the pre-ablated liver and the coagulated region were taken from the

data in Figure 3-8. The dielectric properties of the carbonized liver were taken from [24], which were obtained at a single frequency (ε_r = 8.33, σ = 0.39 S/m, @2.45 GHz). In more detail, the phantom consists of two nested ellipsoids, the outer one having axes with dimensions of 60 × 40 × 40 mm^3 (y-x-z) and the inner one has dimensions of 34 × 13 × 13 mm^3 (y-x-z). The origin of the z-axis is positioned at the tip of the antennas.

By filling the two ellipsoidal regions with different materials, it was possible to simulate three different stages of the treatment, namely (Figure 5-2):

(a) Pre-ablation treatment scenario: both ellipsoids are filled with the untreated liver tissue mimicking material (phantom a1 in Figure 5-2);

(b) Ongoing ablation treatment scenario: the outer ellipsoid is filled with the untreated liver and the inner one with coagulated tissue mimicking material (phantom b1 in Figure 5-2);

(c) Post-ablation treatment scenario: the outer ellipsoid is filled with the coagulated tissue, and the inner one is filled with the carbonized tissue mimicking material (phantom c1 in Figure 5-2).

Since the actual phantom will be fabricated with 3D-printed ABS structures (ε_r = 3, σ = 4 × 10^{-3} S/m) whose thickness is 1.5mm, two sets of numerical phantoms were considered in this study, one without the ABS shells and one with the ABS shells. Phantoms labeled as (a1), (b1), and (c1) in Figure 5-2 refer to ABS-free phantoms (which is close to an ex-vivo ablation

experiment), whereas phantoms labeled as (a2), (b2), and (c2) in Figure 5-2 include the ABS shells.

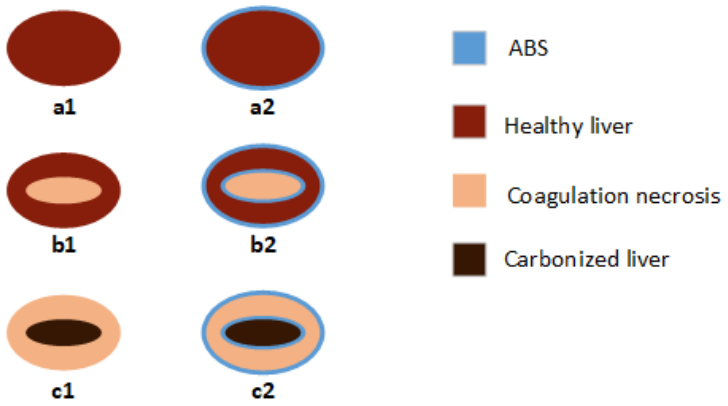

Figure 5-2 The different phantoms considered in the numerical study

In practice, the phantom should be connected to a rack through three pipelines for filling the ellipsoids with the different tissue-mimicking materials and hang above the tank. The cut plane of phantom C2 is shown in Figure 5-3 (a), where dark brown indicates the carbonized liver and light pink indicates coagulation necrosis. Figure 5-3 (b) shows the experimental set-up with the C2 phantom in front of the two-rows antenna array.

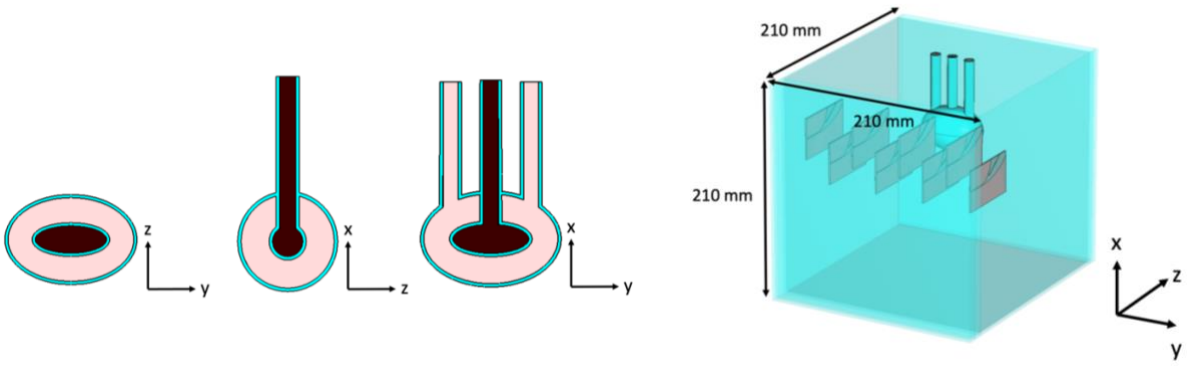

(a) (b)

Figure 5-3 (a) C2 phantom geometry; (b) the experimental setup: the two-row configuration and the C2 phantom

Finally, the initial or reference scenario when 8 SAVAs are simulated when no phantom is present in the container is denoted as s0.

5.3. Electromagnetic Simulations

The MWI device with different phantom configurations (s0, a1, a2, b1, b2, c1, c2) was simulated using the CST software (Dassault Systèmes, Vélizy-Villacoublay, France). In particular, as concerns the relevant MWI quantities, five different frequencies were considered: 600 MHz, 800 MHz, 1000 MHz, 1200 MHz, and 1400 MHz. At each frequency, the incident field E_{inc} of the MWI system (s0 configuration) and the scattering matrix of different simulation configurations (s0, a1, a2, b1, b2, c1, c2) were computed. These simulated fields and scattering parameters provide the quantities needed to mimic the imaging experiments with the proposed setup. For each frequency f of s0 scenario, the simulation provides the incident field $\underline{E}_{inc}(\underline{r}, f) = \underline{E}_{ix}(\underline{r}, f), \underline{E}_{iy}(\underline{r}, f), \underline{E}_{iz}(\underline{r}, f)$ inside the ROI, i.e., the field radiated by each transmitter when no phantom is present (initial state, s0). Moreover, the 8 × 8 scattering matrix **S** encodes the scattering parameters of the antennas in the MWI array. In particular, the elements on the diagonal of **S** are the eight reflection parameters (one for each antenna in the array, S_{ii}), while the off-diagonal elements are the 56 transmission parameters (accounting for all possible antenna combinations in the array, S_{ij}).

The computational time of the forward simulation for each scenario are given in Table 5-1.

Table 5-1 The computational time of the forward simulation for each scenario

Simulation scenario	**a1**	**a2**	**b1**	**b2**	**c1**	**c2**	**s0**
Simulation time	4h,17m,12s	4h,17m,12s	4h,17m,12s	4h,17m,12s	4h,17m,12s	4h,17m,12s	4h,17m,12s

After the forward modeling simulation, the E_{inc} of the ROI was discretized into cubic voxels that have dimensions of 3 × 3 × 3 mm^3 (x−y−z). The total voxel number was 50,225 (35 × 41 × 35, x−y−z). Moreover, to simulate measurement noise, the simulated scattering parameters were corrupted with an additive Gaussian noise with SNR = 50 dB, which is fully consistent

with the performance of commercial vector network analyzers (VNAs) in terms of noise floor and dynamic range.

5.4. Image Formation Algorithm

Algorithms used for microwave imaging can be broadly divided into two main classes: quantitative methods and qualitative methods [30]. Quantitative methods are implemented in the frequency domain, aiming to identify the dielectric properties of the target by solving the inverse scattering problem [65]. Quantitative methods provide comprehensive information of the target under inspection (location, shape, dielectric properties, etc.). However, they are usually computationally expensive and require an initial guess on the target's feature (small, large, lossy, PEC, strong scatter, weak scatter, etc.) to achieve accurate results [30]. Qualitative methods, on the other hand, are implemented either in frequency or in the time domain. Instead of focusing on revealing the dielectric properties of the target, they seek the presence and the location of the target [145]. To this end, they resort to approximations of the scattering phenomenon or rely on the solution of an auxiliary problem, in order to achieve a simplification of the imaging problem to be solved. Qualitative methods are effective and less time-consuming as compared to quantitative methods. Hence, despite they can provide only limited information, they are more of interest for MWI imaging applications wherein real-time images are needed.

Hence, despite they can provide only limited information, they are more of interest for MWI imaging applications wherein real-time images are needed.

In terms of the algorithm that can be used for the MWI system for liver ablation monitoring, the study in [146] compared the performance of two qualitative approaches: distorted Born approximation (DBA) [30] and linear sampling method (LSM). Due to the limitation in aspect imposed by the problem geometry (the abdomen can be probed only from one side and only for a limited portion), better performance is expected from DBA as compared to LSM. In fact, LSM only provides a satisfying result when the target is illuminated from all directions. The

outcome of that study verified this point, demonstrating that the DBA algorithm could provide more accurate imaging results as compared to the LSM, by using the same measurement configuration to image the evolution of the ablation zone. It is worth noting here that the monitoring of MWA can be performed with a qualitative approach in terms of extension of the thermally ablated area and not in terms of variations of temperature during the treatment. As a consequence, a qualitative inversion is of interest here.

In this work, the image reconstruction was carried out through a differential MWI approach similar to the one used in [34]. In such an approach, the imaging task is faced by exploiting the DBA [30]. This approach is suitable for the imaging of small size targets, with low dielectric properties contrast as compared to the background medium. In DBA, the total field induced by each antenna in the ROI ($\underline{E}_{tot}$) can be approximated with the incident field ($\underline{E}_{inc}$), say $\underline{E}_{tot} \cong \underline{E}_{inc}$. By doing so, the underlying imaging task is reduced to a linear ill-posed inverse problem [147]. Such a simplification has the remarkable consequence of reducing the computational complexity, hence enabling performing real-time imaging for the thermal ablation treatment. On the other hand, this approach can only provide information on the morphology (i.e., presence, position, extent) of the region wherein the contrast variation is occurring since the quantitative estimation of the tissue properties is only achieved when the enforced approximation is completely fulfilled.

It is worth mentioning that if the goal of the imaging task is to obtain an estimate of the permittivity in the treated tissue, the iterated (non-real-time) version of the DBA as in [123] could be appropriate. However, the goal of this thesis is to develop an MWI device for monitoring the treatment procedure, which lasts no more than 10 mins. A suitable algorithm would be one that can determine the position and size of the treated tissue in a timely manner.

To form the MWI images, the input datum of the imaging procedure was given by the differential scattering parameters calculated as the difference between the (noise corrupted) scattering parameters simulated in two different scenarios. From all the simulated scenarios, ten differential data sets were generated, namely: aX-s0, bX-s0, cX-s0, bX-aX, cX-bX, where X is

equal to 1 or 2 according to the considered phantom (see Figure 5-2). The data sets aX-s0, bX-s0, and cX-s0 account for the changes that occurred with respect to the reference scenario, and therefore the goal was to image the extent of the outer ellipsoid. In the meanwhile, the bX-aX data set is representative of a scenario in which the changes occur only in the inner ellipsoid, wherein the tissue ablated in the initial part of the treatment is located. Finally, cX-bX accounted for the difference between the intermediate and final stages of the treatment, and the goal was to image the external ellipsoid and possibly the transition from necrosis to carbonization occurring in the inner part.

The generic data-set can be denoted as $\mathbf{\Delta S}$; it is made by a 320-elements vector containing the complex values of the differential scattering parameters (considering the available 5 frequencies and 64 scattering parameters for each frequency). This vector is obtained by reshaping into a vector the five available 8 × 8 differential scattering matrices.

The kernel of the imaging algorithm is given by a 320 × 50225 matrix, $\mathbf{K}$, whose generic element, $\mathbf{K}_{mn}$, is given by:

$$\boldsymbol{K_{mn}} = \frac{-\boldsymbol{j}}{\boldsymbol{4}}\boldsymbol{\omega_f}\boldsymbol{\varepsilon_{eqCM}}\underline{\boldsymbol{E}}_{\boldsymbol{i}}(\boldsymbol{r_n}, \boldsymbol{p}) \cdot \underline{\boldsymbol{E}}_{\boldsymbol{i}}(\boldsymbol{r_n}, \boldsymbol{q}) \qquad (5\text{-}1)$$

where n = 1, …, 50225 denotes the n-th voxel of the ROI, ω_f is the angular frequency, with f = 1,...,5 denoting the relevant frequency, $\varepsilon_{eqCM} = \varepsilon_r\varepsilon_0 + j\frac{\sigma}{\omega}$ is the complex equivalent permittivity of the coupling medium, p = 1,...,8 denotes the transmitting antenna in the array, and q = 1,...,8 denotes the receiving antenna. The f, p, and q indices are organized in the same way as the data vector $\mathbf{\Delta S}$.

Let $\mathbf{\Delta x}$ denote a 50225 × 1 vector, whose elements are the values of the unknown contrast in the voxels of the ROI, i.e., the variation of the dielectric properties within the ROI for the different data sets.

With respect to the above, the matrix equation to be solved reads:

$$\mathbf{\Delta S} = \mathbf{K}\mathbf{\Delta x} \qquad (5\text{-}2)$$

Since the kernel matrix **K** is ill-conditioned, Equation (5-3) cannot be solved via direct matrix inversion but must be solved in a generalized sense, introducing some form of regularization. To this end, it is possible to define the singular value decomposition (SVD) of **K** as [119]:

$$\mathbf{K} = \mathbf{U} \cdot \sum \cdot \mathbf{V}^{\boldsymbol{H}} \tag{5-3}$$

where **U** is the matrix of the left singular vectors of **K**, **V** is the matrix of the right singular vectors of **K**, $\sum$ is a diagonal matrix of the singular values, and $^{\boldsymbol{H}}$ stands for the conjugate transpose. The diagonal of $\sum$ is populated with the singular values σ_i of **K**, which are real scalars, approaching zero as: $\sigma_1 \geq \sigma_2 \geq \cdots \geq 0$. Once **K** is evaluated, the problem is solved in a regularized sense using the truncated singular value decomposition (TSVD) algorithm [34] that provides an explicit inversion formula for Equation (5-3) that reads:

$$\Delta\mathbf{x} = \mathbf{V}\boldsymbol{\Sigma}_{\boldsymbol{\nu}}^{\mathbf{-1}}\mathbf{U}^{\boldsymbol{H}}\Delta\mathbf{S} \tag{5-4}$$

where $^{\mathbf{-1}}$ denotes the inverse of the matrix, and $\boldsymbol{\Sigma}_{\boldsymbol{\nu}}$ is the same matrix as $\boldsymbol{\Sigma}$ except that it contains only the singular values that have an index that is lower than the threshold index ν (the other singular values are replaced by zeroes). The threshold ν acts as a regularization parameter. Such a regularization parameter is chosen as a trade-off between the accuracy and the stability of the approximation, depending on the noise level. In particular, larger values of ν lead to higher accuracy but lower stability of the estimated solution [119]. Typically, the candidate values of ν correspond to the indices where the singular value curve presents a change in slope.

As the imaging algorithm provides qualitative information only, the estimated $\Delta\mathbf{x}$ is turned into its normalized absolute value, **I**, which represents the final output of the imaging procedure.

$$\mathrm{I} = \frac{\Delta\mathbf{x} - \Delta\mathbf{x}_{\boldsymbol{min}}}{\Delta\mathbf{x}_{max} - \Delta\mathbf{x}_{min}} \tag{5-6}$$

The SVD also provides a way to appraise the achieved results with respect to the best possible result that can be obtained by means of the adopted reconstruction algorithm. Such an ideal reconstruction, say $\Delta\mathbf{x}_{\boldsymbol{ID}}$, is computed for each scenario as:

$$\Delta \mathbf{x}_{\boldsymbol{ID}} = \mathbf{V}_{\boldsymbol{\nu}} \ \mathbf{V}_{\boldsymbol{\nu}}^{\boldsymbol{H}} \ \Delta \mathbf{x}_{\boldsymbol{GT}} \quad (5\text{-}7)$$

where $\Delta \mathbf{x}_{\boldsymbol{GT}}$ is the ground truth (i.e., the contrast used to generate the data), and $\mathbf{V}_{\boldsymbol{\nu}}$ is a $N \times \nu$ matrix whose columns are the first ν right singular vectors of **K**. The quality of the reconstruction is finally appraised by means of the mean square error (MSE) defined as:

$$MSE = \frac{1}{n} \sum\nolimits_{\boldsymbol{voxels}} |\mathbf{I}_{\boldsymbol{ID}} - \mathbf{I}|^{\mathbf{2}} \quad (5\text{-}8)$$

where $\mathbf{I}_{\boldsymbol{ID}}$ denotes the normalized absolute value of $\Delta \mathbf{x}_{\boldsymbol{ID}}$. A lower MSE value usually indicates that the reconstruction of the image is closer to the ground truth.

5.5. In-silico Validation of the MWI system

5.5.1. Selection of Measurement Configuration

As it was mentioned in section 5.2.1, two measurement configurations were studied: the one-row configuration and the two-rows configuration. The study in [120] shows that when using the same number of antennas, a staggered antenna array configuration could reduce the system discretization error, thus leading to a better imaging of the ROI. Therefore, an analysis of the TSVD threshold index on the two measurement configurations was performed, and their plot of the normalized singular values σ_n in the dB scale is reported in Figure 5-4.

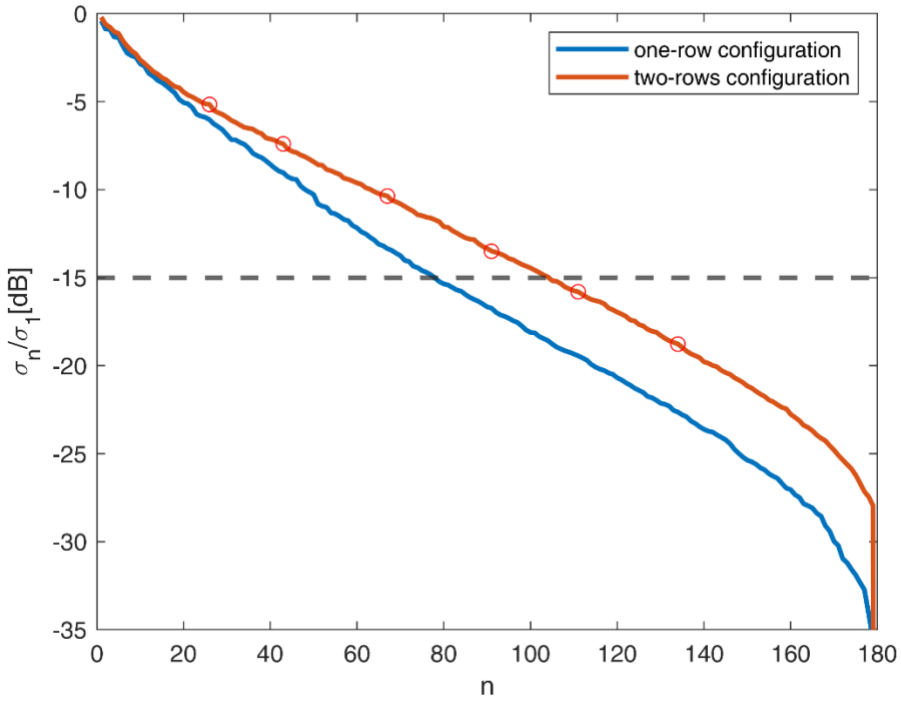

Figure 5-4 The normalized singular values in two measurement configurations.

TSVD threshold index has to be appropriately selected in order to make the proper reconstruction. The TSVD threshold index was selected according to the following observation: the energy of the differential signals was, on average, approximately −15 dB (see the following paragraph and Table 5-3). The threshold number should be selected as a trade-off to mitigate the impact of the noise on the results and improve their accuracy. In another way: to retain as many singular values as possible in the TSVD formula (5-5) while avoiding instabilities due to noise. In this case, the threshold index was set at $\nu = 92$, as this corresponded to the point at which the change in the slope of the singular value curve occurred just above the level of the noise expected on the differential signal (see Figure 5-4). Selecting lower truncation indices (e.g., 27, 44, 68) would entail a loss of a significant part of the available information, while selecting higher thresholds (e.g., 112, 135) would lead to results dominated by the presence of noise and, hence, unstable. Note that even if the considered noise level was reasonable if compared to the

noise floor of a typical VNA, the above observations also suggest that a noise level slightly larger than -50dB can be tolerated.

Finally, it is observed from Figure 5-4 that, if selecting the same singular values, the two-rows measurement configuration corresponds to a higher signal level than the single row configuration. This indicates that the system is more stable against noise and it could retrieve more information along the x-axis as compared to the one-row configuration. Following this result, and for the sake of simplicity and brevity, in the following the results achieved from the staggered two rows configurations will be reported only.

5.5.2. Signal Level

The first analysis carried out in this study is concerned with the comparison of the signal level associated with the scattering matrices simulated in the different scenarios. To this end, the L2 norm of each matrix, i.e.,

$$S = \sqrt{\sum_{i,j=1}^{8} |S_{ij}|^2} \quad (5\text{-}5)$$

was computed. The obtained values are reported in Table 5-2.

Table 5-2 L2 norm of scattering matrices of the simulated data set.

Frequencies (MHz)	**a1**	**a2**	**b1**	**b2**	**c1**	**c2**	**s0**
600	0.2316	0.2291	0.2315	0.2291	0.2303	0.2293	0.228
800	0.4935	0.4932	0.4934	0.4932	0.4934	0.4933	0.4933
1000	0.3848	0.3849	0.3848	0.3849	0.3848	0.3851	0.3849
1200	0.3731	0.3751	0.3732	0.3749	0.3727	0.3735	0.3725
1400	0.2576	0.2562	0.2575	0.2569	0.2574	0.2572	0.2552

The analysis of the norm of the scattering matrices (Table 5-2) shows that the signal level in all experiments is similar. This observation is linked to the reduced penetration depth and, as a consequence, sensibility of the imaging approach. From Table 5-1 it can be seen that the phantom in the two scenarios (i.e., presence or absence of ABS shells) can be considered equivalent as far as the expected signal level is concerned. In fact, the reference scenario s0 gives a comparable signal level to aX, bX, and cX scenarios (X = 1, 2). Therefore, the measured signal is dominated by the antenna crosstalk, and the useful information is embedded in the differential data.

For such a reason, it is crucial to analyze the norms of the differential scattering matrices, i.e., the matrices calculated aX-s0, bX-s0, cX-so, bX-aX, cX-bX (X = 1,2). So, the L2 norm of the differential scattering matrices $\mathbf{\Delta S}$ was computed. In this case, to provide a homogeneous evaluation, the norm was normalized to the s0 data set and expressed in dB. The values of the norm are reported in Table 5-3 concerning the different cases with respect to the reference scenario (Table 5-3) and the differences due to the presence of the ABS shells.

Table 5-3 L2 norm (in dB) of the differential scattering matrices of the simulated data sets aX-s0, bX-s0, and cX-s0, bX-aX and cX-bX, with X being equal to 1 or 2, normalized to the s0 data set. Refer to Figure 5-2 for the different cases.

Frequencies (MHz)	$\frac{a_1 - s_0}{s_0}$	$\frac{a_2 - s_0}{s_0}$	$\frac{b_1 - s_0}{s_0}$	$\frac{b_2 - s_0}{s_0}$	$\frac{c_1 - s_0}{s_0}$	$\frac{c_2 - s_0}{s_0}$	$\frac{b_1 - a_1}{s_0}$	$\frac{b_2 - a_2}{s_0}$	$\frac{c_1 - b_1}{s_0}$	$\frac{c_2 - b_2}{s_0}$
600	-9.1691	-8.3483	-9.378	-8.3539	-10.6265	-8.3711	-22.4271	-24.3187	-14.2327	-15.331
800	-13.6496	-19.8876	-13.8819	-19.8217	-15.6235	-16.7927	-23.8928	-25.5669	-17.2809	-16.0611
1000	-13.3061	-14.3102	-12.964	-14.2904	-16.1749	-17.329	-22.7961	-24.2293	-15.7438	-14.7183
1200	-14.6999	-15.1735	-14.029	-15.2162	-15.5892	-17.8561	-22.2344	-23.044	-18.3703	-15.4217
1400	-14.2597	-18.7633	-13.7562	-12.6105	-13.6149	-14.5755	-20.8188	-20.5474	-18.5486	-15.2951

Comparing the cases with and without ABS shells, it is found that the signal levels in all cases are almost always comparable. It is observed that for the bX–aX cases (X = 1,2), the signal levels are relatively lower as compared to the other 8 cases (aX-s0, bX-s0, cX-so, cX-bX). This is due to the fact that in the bX–aX cases (X = 1,2) the change in the phantom dielectric properties only occurs in the inner ellipsoid (see Figure 5-2). Therefore, it has a lower perturbation on the electromagnetic field. Nevertheless, the results in the table confirm that the designed experiment with the proposed phantom is achievable because the signal level is almost the same with or without the presence of the ABS shells and in the same power level dynamic range of commercial VNAs.

5.5.3. Images Reconstruction

The obtained MWI reconstructions of the staggered two-rows antenna array configuration are shown from Figure 5-5 to Figure 5-14 for all the considered scenarios. In the figures, the cross-sections along the z-axis (i.e., moving from the antenna towards the phantom) are shown. The contour of the phantom was superimposed on the reconstructed images in the relevant cross-sections to improve readability. For the sake of the readability of the results, the visualization of the outcomes was limited to the range y = −60 to 60 mm, x = −51 to 51 mm, and z = 17 to 104 mm. In particular, the voxel layers on the boundary of the ROI close to the antennas were not shown to avoid artifacts that were due to the antennas' presence. The subplots in each figure are shown as slices in the x-y plane for various values of z, with 3 mm intervals. In the panels, the y-axis is the horizontal axis, and the x-axis is the vertical one (see Figure 5-3 for the reference system adopted). Units are in mm. Reconstructed contrast is in normalized amplitude, and the color bar ranges from 0 (white) to 1 (dark red).

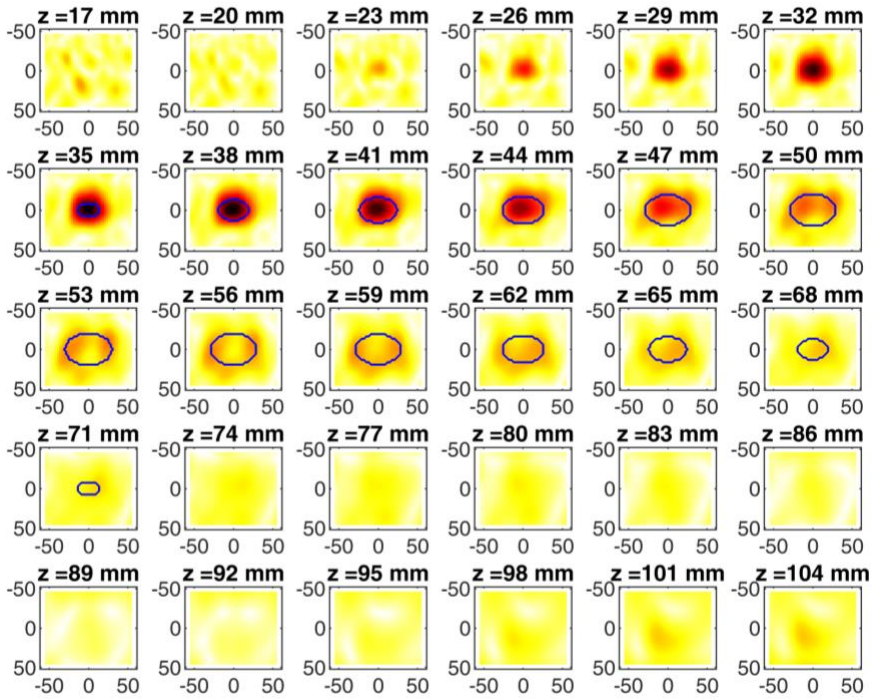

Figure 5-5 MWI reconstructions for the a1-s0 data set

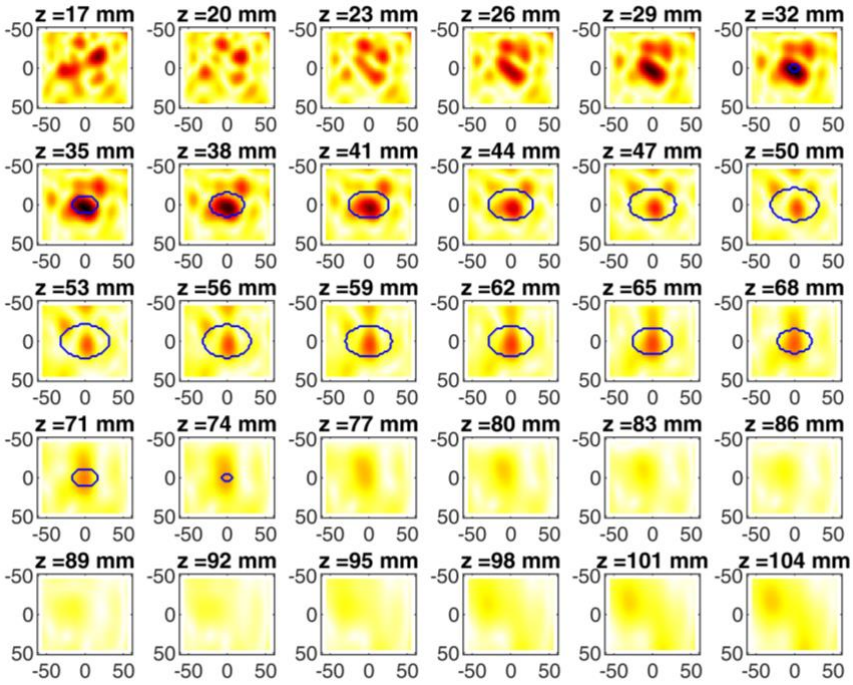

Figure 5-6 MWI reconstructions for the a2-s0 data set

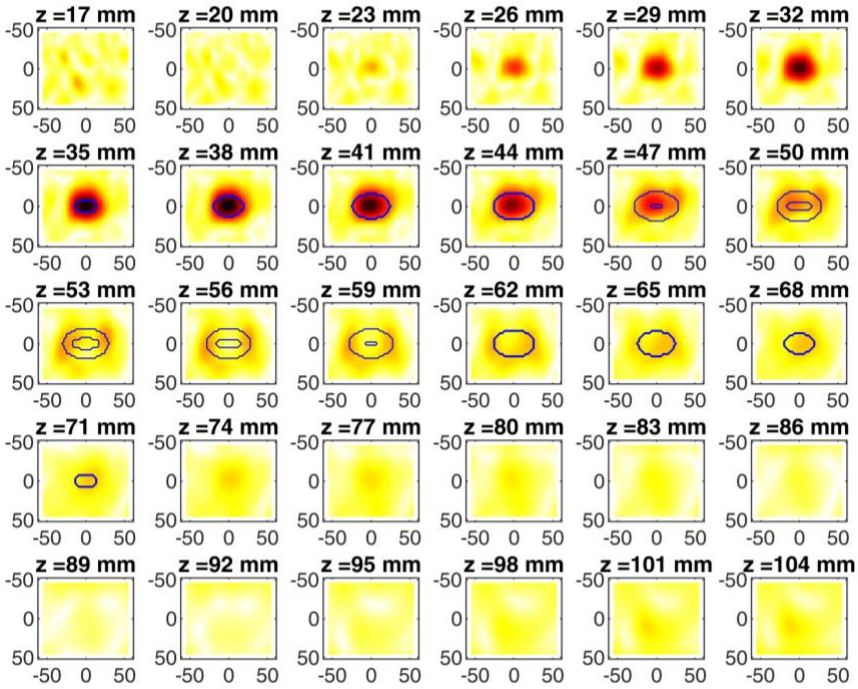

Figure 5-7 MWI reconstructions for the b1-s0 data set.

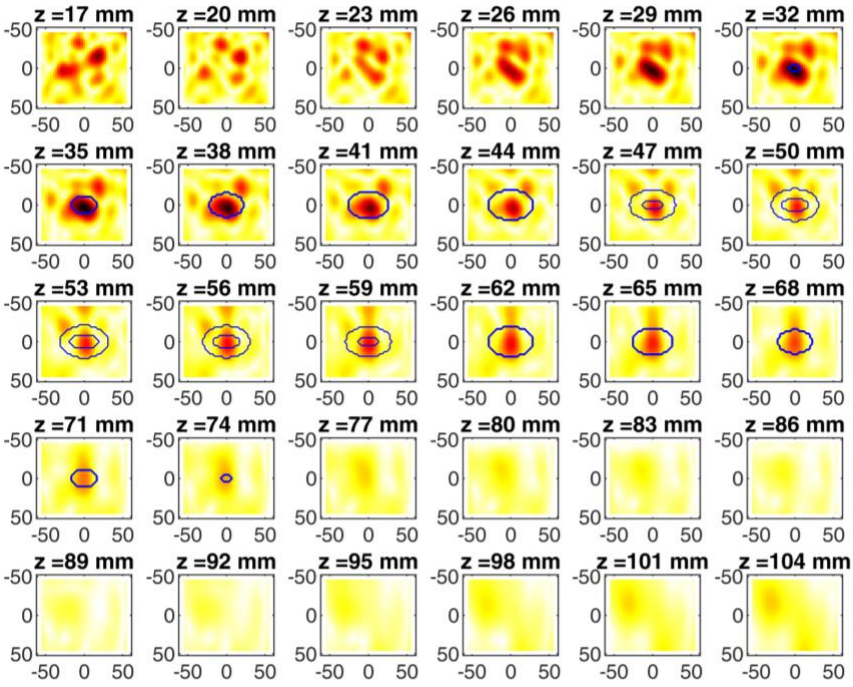

Figure 5-8 MWI reconstructions for the b2-s0 data set

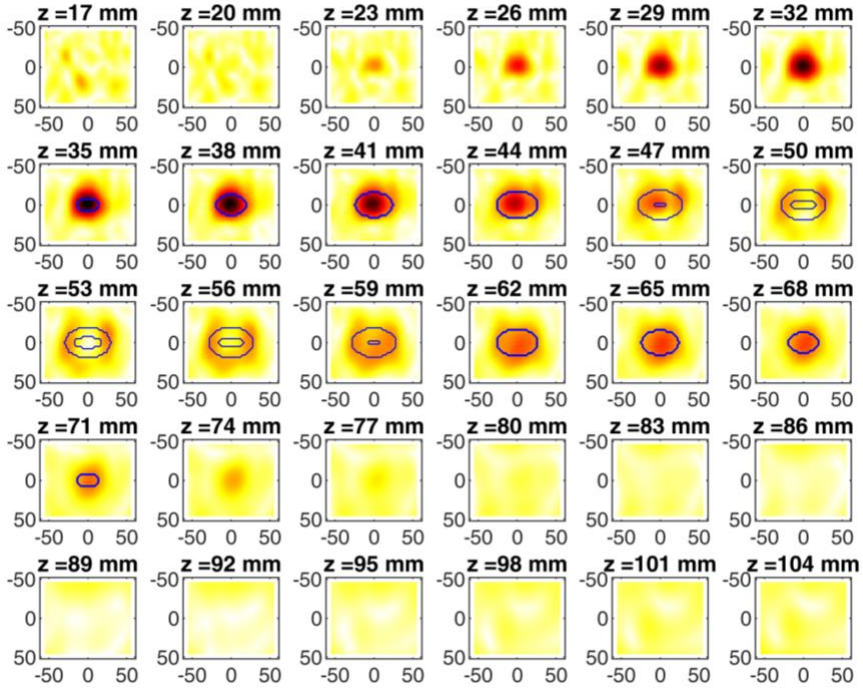

Figure 5-9 MWI reconstructions for the c1-s0 data set

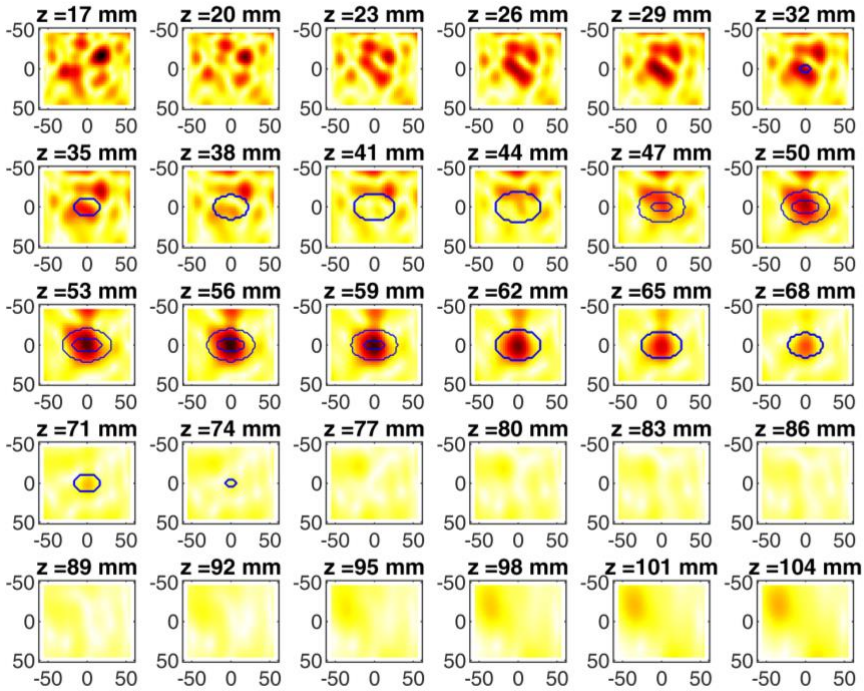

Figure 5-10 MWI reconstructions for the c2-s0 data set

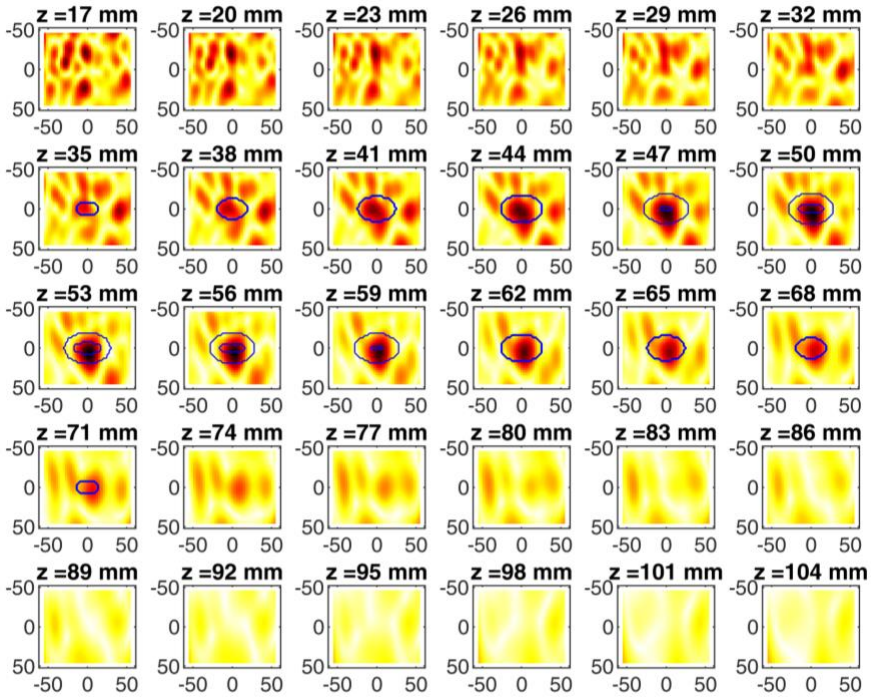

Figure 5-11 MWI reconstructions for the b1-a1 data set

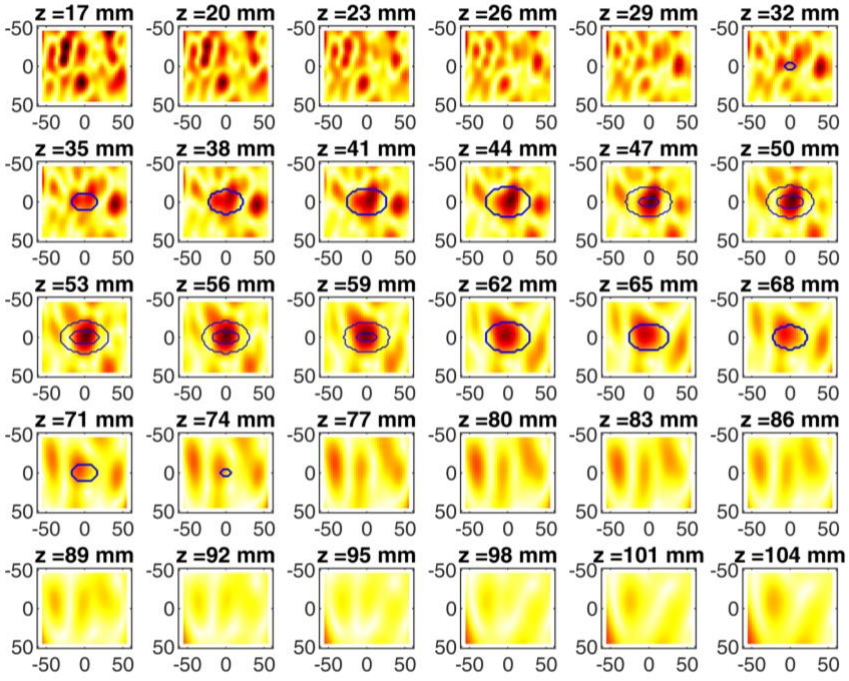

Figure 5-12 MWI reconstructions for the b2-a2 data set

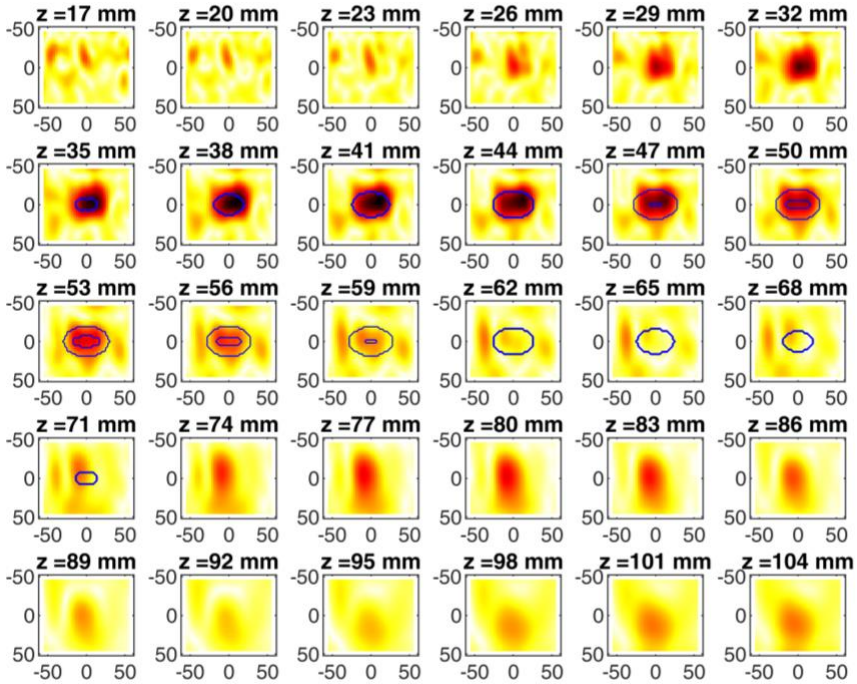

Figure 5-13 MWI reconstructions for the c1-b1 data set

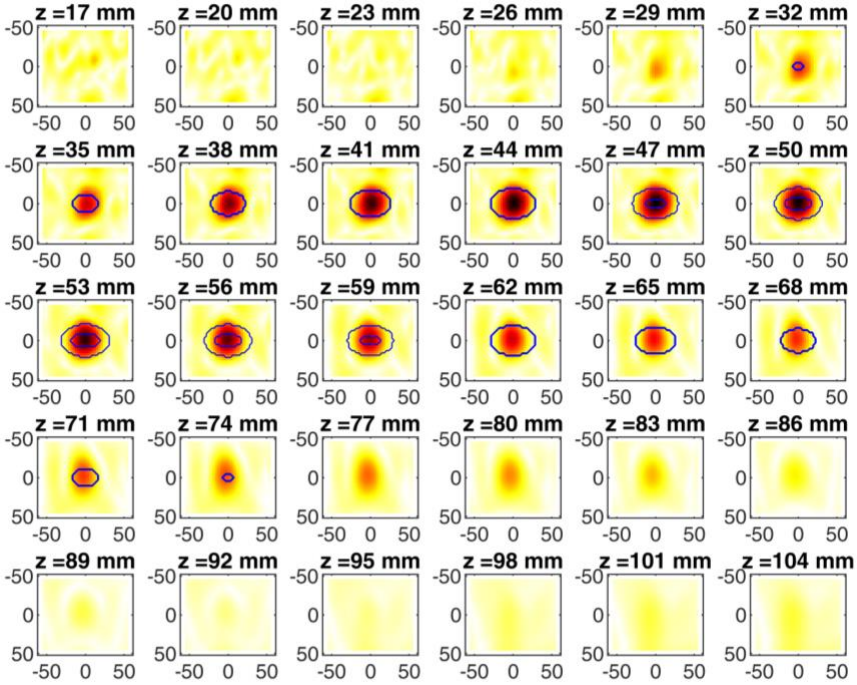

Figure 5-14 MWI reconstructions for the c2-b2 data set

The MSE with respect to the ideal reconstruction (i.e., the one obtained assuming that the DBA was exactly fulfilled) was computed for all cases to appraise the quality of the results. The MSE values are reported in Table 5-4.

Table 5-4 MSE with respect to the ideal reconstruction

a1-s0	**b1-s0**	**c1-s0**	**b1-a1**	**c1-b1**
0.37	0.35	0.28	0.65	0.49
a2-s0	**b2-s0**	**c2-s0**	**b2-a2**	**c2-b2**
0.57	0.57	0.79	0.88	0.29

The analysis of the MSE (Table 5-4) provides a quantitative assessment of the results obtained by applying the TSVD algorithm to the different data sets and shows that they are quite close to the corresponding ideal reconstructions. A lower MSE value was observed for the target without ABS shells, indicating that the reconstruction of the images is closer to the ground truth. On the other hand, a higher MSE value was observed for the case with ABS shells, which has to be attributed to the electromagnetic field perturbation caused by the presence of the ABS shells.

From a qualitative point of view, the results in Figure 5-5 to Figure 5-14 show that regardless of the presence of the ABS shells, the two classes of phantoms lead to comparable results, supporting the validity of the designed experimental setup. In particular:

- In the a1-s0, b1-s0, and c1-s0 cases (Figure 5-5, Figure 5-7, and Figure 5-9), wherein the goal is to image the external ellipsoid, the reconstruction of the target is larger than the ground truth. In particular, the target always appeared at z = 26 mm, that is 6 mm before the actual position, and the reconstruction of the target dimension along the x-y plane is larger than the ground truth contour before z = 53 mm. From z=53 mm to z=71mm the target is over lap with the ground truth. This is because the antenna is illuminating the target from only one side, the signal is weaker from the

back of the target. While for a2-s0, b2-s0, and c2-s0 cases (Figure 5-6, Figure 5-8, and Figure 5-10) the target always appeared in correspondence with the same ground truth contour, and the reconstruction of the target dimension along the x-y plane is similar to the ground truth contour before z = 53 mm.

- For the b1-a1 and b2-a2 cases (Figure 5-11 and Figure 5-12), in agreement with the lower signal level, the images were less clear, especially for the phantom without ABS. This is partially due to the low contrast between the treated and untreated liver tissue, because the dielectric properties variation occurs only at the inner ellipsoid, which has a low perturbation on the e-field distribution as compared to other scenarios. Despite the mentioned difficulties, it was still possible to image the region where the ablation was occurring (i.e., the inner ellipsoid). The target appeared at z = 47 mm, in correspondence of the same section as the inner ellipsoid. For b2-a2 cases, the ABS shell has a higher dielectric contrast with respect to the tissue-mimicking materials. This led to a higher differential signal level and better reconstruction as compared to the b1-a1 scenario.
- Finally, for the c1-b1 and c2-b2 cases (Figure 5-13 and Figure 5-14), similar to aX-s0, bX-s0, and cX-s0 cases (X = 1,2), the reconstruction of the target is larger than the ground truth. In particular, the target on the images shows up before its actual position for the ABS-free phantom, and the reconstruction of the target dimension along the x-y plane is larger than the ground truth contour before z = 53 mm. From z=53 mm to z=59 mm the target is over lap with the ground truth. Whereas slightly better results were obtained in the case in which the ABS shells are present.

In general, in all cases, the features of the evolving scenarios were quite clearly identified in terms of the maximum extent of the region where the variation was occurring. However, due to the limitation of available ports supported by a commercial VNA that is used in the lab, the MWI device in terms of the number of antennas is limited to up to eight antennas. Other limitations of the systems are the measurement configurations (the antennas illuminate the

target only from one side, i.e., the x-y plane). In particular, this latter limitation resulted in an obvious degradation of the estimated shape along the x-z plane, in agreement with the fact that a 3D image is being reconstructed from data measured by a planar array. Moreover, the occurrence of artifacts, which is due to the presence of noise, does not impair the interpretation of the results (but for the bX-aX case). Finally, it is worth remarking that the computational time of the imaging reconstruction is quite low since all 3D images were obtained in 8 seconds by using a desktop PC (CPU: Intel Xeon Gold 6136 3.0 GHz, Dual Core; RAM: 256 GB (16x16 GB) DDR4 2666 MHz). This MWI application is capable of real-time monitoring. As a matter of fact, the only computationally intensive part of the algorithm was the evaluation of the SVD of **K**, which can be done offline, being independent of the scenario.

5.6. Summary

This chapter reports the in-silico validation of a multi-view multi-static MWI system for real-time monitoring of thermal ablation of liver tumors. In particular, the study validated the arrangement of an experimental set-up that is going to be realized. The obtained results confirm that the designed setup can fulfill the purpose, despite the presence of ABS shells in phantom a2, b2, and c2 degrading the image quality as compared to the phantoms without the ABS shells. Moreover, the results also confirm that the MWI device, being made by two rows of antennas, is capable of achieving real-time 3D imaging results conveying information on the position of the ablated area.

The limitations of this study are related to the following aspects:

- MWI system measurement configuration. Unlike the MWI system for breast or brain imaging, and MWI systems proposed for different MWA treatments [122][123][146][148], in which the antennas are placed circularly around the under-examined body, the antennas in this MWI system could only illuminate the target from one side. Being unable to view the ROI from all directions brings difficulties to the reconstruction of 3D imaging.

- The pre-treatment scenario should consider tumor tissue rather than liver tissue to mimic actual clinical conditions. Due to the lack of knowledge of liver tumor dielectric properties, the first stage of validation of an ablation monitoring device typically involves ex-vivo liver samples (e.g., [34] healthy liver tissue was chosen as a pre-treatment scenario in the simulation study).

The conducted analysis showed that several improvements could be implemented on the proposed setup, both from the point of view of the hardware of the system and of the data processing technique. First of all, a larger number of frequency points can be acquired to increase the amount of data and improve rejection to noise. Improvements can also be foreseen for the imaging algorithm, either using a different algorithm, such as the iterated version of the DBA used in [123], or incorporating available a priori information in the electromagnetic model used to build the imaging kernel **K**. In this respect, the use of a pre-operatory image of the scenario can be extremely useful.

Chapter 6

6. Experimental Validation of the Microwave Imaging Device

Parts of this chapter will be published as:

- [C-9] M. Wang, R. Scapaticci, S. Abedi, H. Roussel, N. Joachimowicz, S. Costanzo, M. Cavagnaro, L. Crocco, "A microwave imaging system prototype for liver ablation monitoring: design and initial experimental validation", in 2022 IEEE International Workshop on Antenna Technology, IWAT 2022. Accepted.

6.1. Introduction

The in-silico validation of the microwave imaging system with 8 SAVA antennas demonstrated a satisfying outcome. The successive step was the experimental validation, demonstrated in this chapter.

The experimental validation of the MWI system is a preliminary step towards the realization of the MWI system for clinical purposes. It verifies the feasibility of a MWI system in the scenario which is similar to monitoring the real-time MTA treatment. The in-silico assessment of the MWI system in Chapter 5 considers the system errors by contaminating the simulation data with 50 dB Gaussian noise. The experimental assessment of the MWI system confronts different challenges, leading to the degradation of the imaging results, namely:

- Due to fabrication diversity, different antenna's matching can be observed for each antenna, this inconsistency causing a mismatch between the numerical model of the device and its actual behavior.
- The presence of environmental noise and the crosstalk between channels induces errors in the measurement datasets.
- The dielectric properties difference between those used in the in-silico study and in the real case incurs imaging contrast with bias.

The experimental assessment of the microwave imaging system has been developed as follows: firstly, tissue-mimicking materials were determined. In particular, three different tissue-mimicking materials representing the healthy liver, coagulation necrosis, and carbonized liver were fabricated and characterized. It is worth mentioning that, as this is a initial experimental validation of the MWI system, the goal is to design a set-up with repeatable performances. Therefore, instead of using pre and post-ablated bovine liver tissue, the set-up used tissue mimicking material as phantom. Then, the initial experimental validation of the microwave imaging system was performed. For facility constraints, the experimental set-up did not use 8 SAVA antennas in the array configuration as it was described in chapter 5. Rather,

a simple multi-view mono-static version of the system was considered. In this respect, one antenna immersed inside the tank filled with coupling medium was moved along a linear path collecting the scattering parameters. The scattering parameters of the scenarios with and without the presence of the phantom were measured. Moreover, since it is difficult to move one antenna up and down in the tank during the experiment (mimicking the two-rows measurement configuration in chapter 5), the mono-statistic MWI system only considers a single antenna moving along a linear path along the y-axis. The goal of this experimental validation was mainly to identify the differential signal levels of different scenarios due to the dielectric properties change in the region of interest.

6.2. Characterization of the Tissue Mimicking Material Dielectric Properties

The phantom used in the experimental set-up is the same as the phantom a2, b2, and c2 described in section 5.2.2, which represent the liver tissue at three different ablation stages. The 3D-printed structure, shown in Figure 6-1(a), consists of two nested ellipsoids. By filling the two ellipsoids with different tissue-mimicking materials, the mentioned a2, b2, and c2 phantoms can be represented. The ellipsoidal structure is connected to a rack through three pipelines. By moving the rack back and forth the distance between the antenna and the phantom can be adjusted (Figure 6-1(b)). The tank, rack, and the ellipsoidal phantom are all made of acrylonitrile butadiene styrene material.

(a) (b)

Figure 6-1 (a) Phantom inner structure (b) Phantom and the tank

The tissue-mimicking materials are made of a Triton-X/water/NaCl mixture whose properties can be tuned by adjusting the Triton-X to water ratio. The NaCl in the recipe was used to increase the mixture conductivities. The dielectric properties measurement was performed with the same set-up as the one for coupling medium measurement, as presented in section 3.5. The phantom materials recipes are shown in Table 6-1.

Table 6-1 Tissue mimicking material recipe

	The ratio in mass (g)		
	NaCl	Triton X-100	Distilled Water
Healthy liver	0.39%	32.64%	66.97%
Coagulation necrosis	0	49.96%	50.04%
Carbonized liver	0	85.89%	14.11%

The measured dielectric properties of tissue-mimicking materials are shown in Figure 6-2. In particular, each tissue-mimicking material was measured three times, and the average results of the three measurements were reported. In the figure, the reference dielectric properties of the liver tissue are reported also. In particular, the healthy liver and the coagulation necrosis properties are from Figure 3-8. The carbonized liver tissue properties, obtained at 2.45 GHz, are from the literature [24].

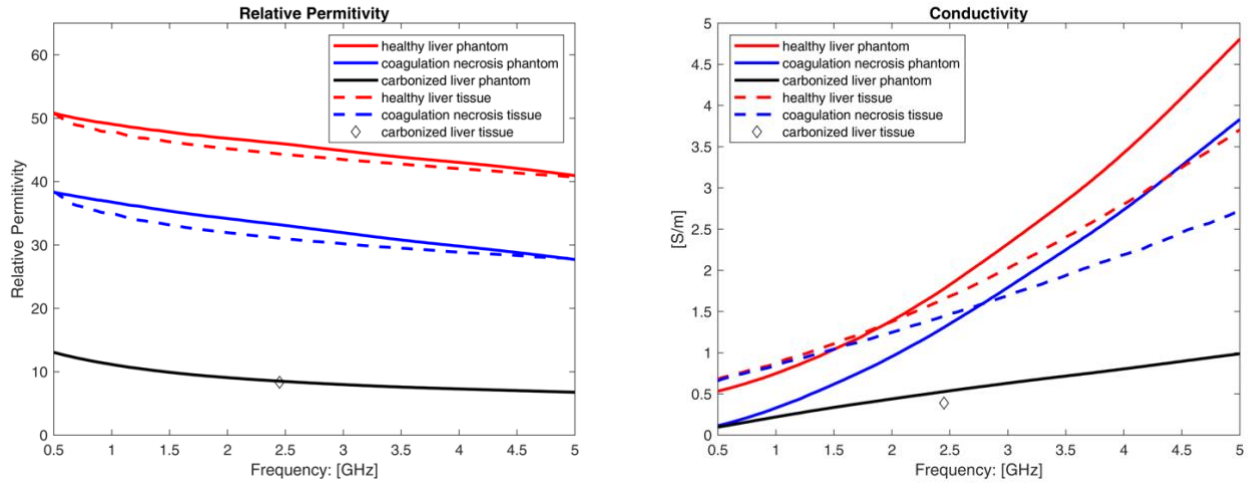

(a) (b)

Figure 6-2 Dielectric properties of tissue-mimicking material

To further understand the difference between the phantom dielectric properties and the corresponding tissue (i.e., healthy liver [136], coagulation necrosis [136], and carbonized liver [24]), their properties difference along the frequency band 500 MHz - 5 GHz were evaluated. The mean values and standard derivations of the difference are reported in Table 6-2. Since the literature [24] provided the carbonized liver properties at a single frequency (2.45 GHz), the measured value at this frequency is compared only. It is found that the permittivity difference between the phantom and the corresponding tissue is within 5%. However, the conductivity difference is up to 36%; unfortunately, due to the limitation of the materials used to make the phantoms, it is not possible to decrease this difference by modifying the ratio of ingredients. Besides, the conductivity of the phantom could only be increased by adding more NaCl into the recipe.

Table 6-2 Dielectric difference between the phantom material and the corresponded tissue

Tissue mimicking phantom	relative permittivity difference		conductivity difference	
	Mean	STD	Mean	STD
Healthy liver	0.0267	0.0084	0.1531	0.1535
Coagulation necrosis	0.0466	0.0211	0.304	0.2059
Carbonized liver	0.0214	N/A	0.3567	N/A

6.3. Initial Experimental Validation of the Microwave Imaging System

The top-view of the configuration adopted for the experiment is shown in Figure 6-3 (a). In this setup, the antenna is immersed into a tank filled with the realized coupling medium and moved along a linear path parallel to the longitudinal axis of an ellipsoidal phantom mimicking the liver tissue during the ablation treatment procedure. The antenna recorded the scattering parameters at 8 different positions, as is shown in Figure 6-3 (a), which is the same as the configuration of MWI in section 5.2.2. In particular, the distance between each position is 23 mm, and the phantom is placed 35 mm away from the antenna tip.

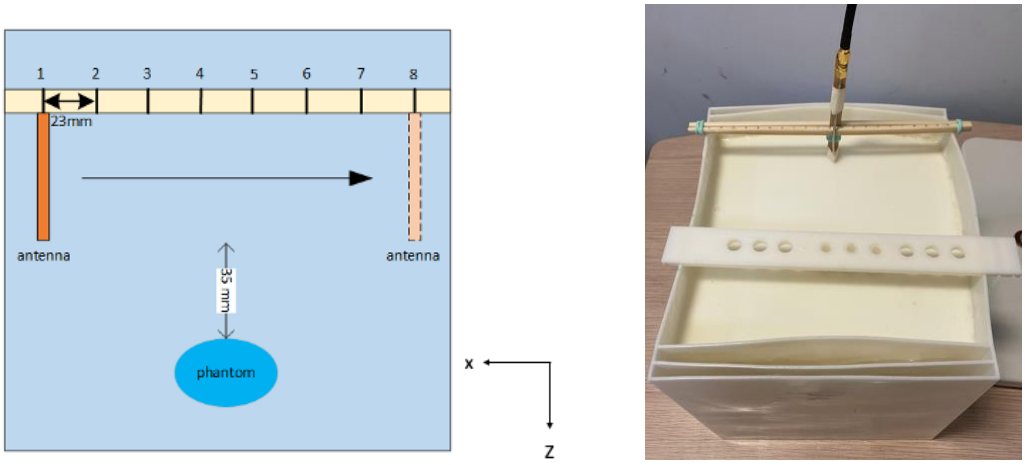

(a) (b)

Figure 6-3 (a) Scheme of the mono-static MWI system configuration (b) Experimental implementation of the mono-static MWI system

6.3.1.1. Signal Level

The scattering parameters were recorded at 8 different positions for the following scenarios: ROI with phantoms (a2, b2, c2) and ROI without phantom (s0). For each position, the S-parameters were recorded 5 times without the phantom, and 5 times with the presence of the phantom. The S-parameters results were averaged in the data processing.

Figure 6-4, Figure 6-5, and Figure 6-6 demonstrate the antenna's S-parameters at position 4, with and without the presence of a2, b2, and c2 phantom, reporting both the numerical data and the measured ones. Additionally, in the figures, the numerical and experimental differential signals are reported. It is found from the figures that the antenna's simulation result agrees with the measurement result in all scenarios, especially from 500 MHz to 2 GHz. The simulation and the measurement differential signal curves are slightly different from each other. This could be due to the inaccurate antenna placement during the experiment. Since the coupling medium is not transparent, it is difficult to confirm if the antenna is always in parallel to each other at different positions. However, the differential signal levels of the simulation and measurement are similar, in the range from -30dB to -70dB. Such a signal level is above the dynamic range of a commercial VNA.

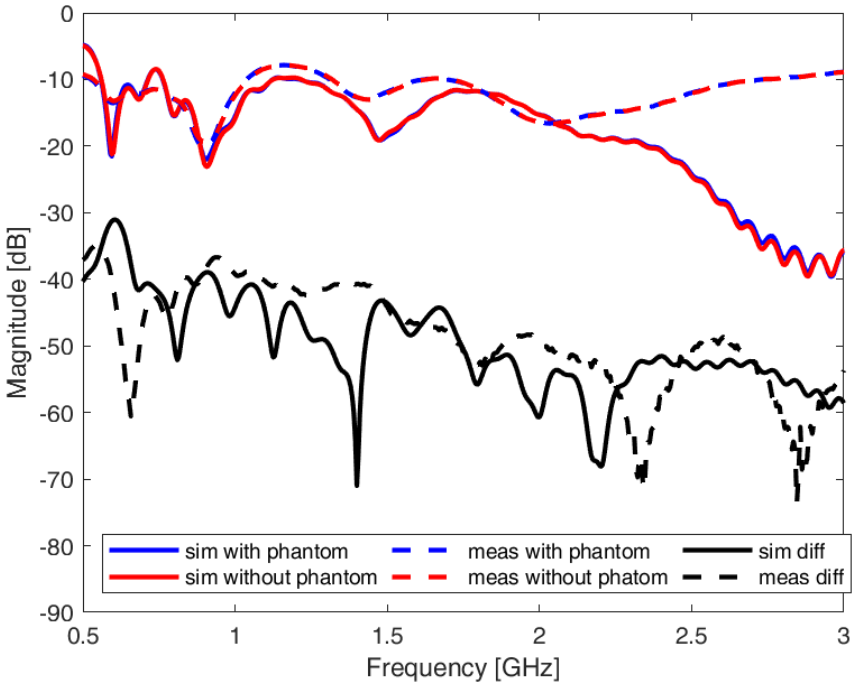

Figure 6-4 Antenna S-parameters with and without a2 phantom, and differential signals level of 'a2-s0' at position 4

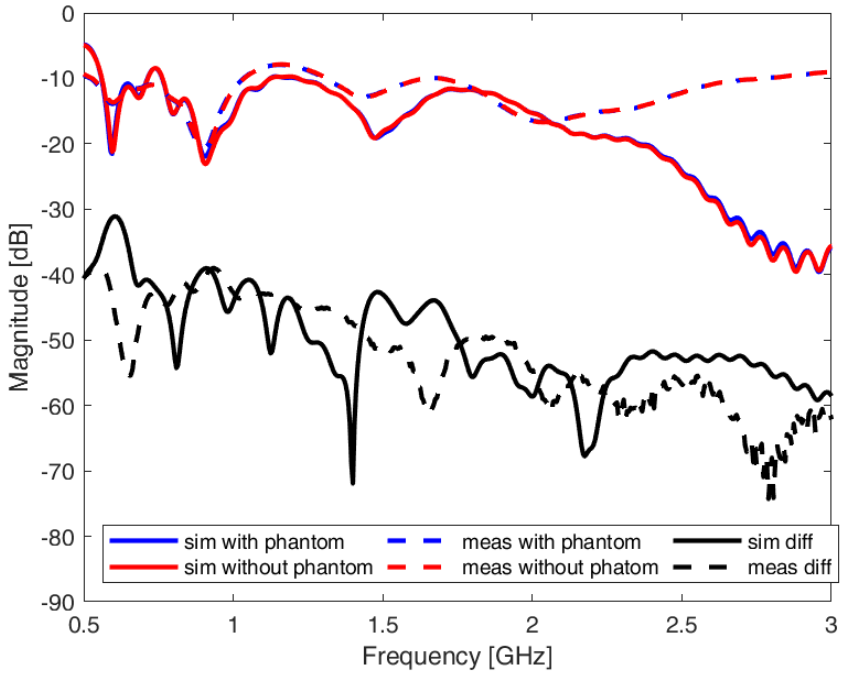

Figure 6-5 Antenna S-parameters with and without b2 phantom, and differential signals level of 'b2-s0' at position 4

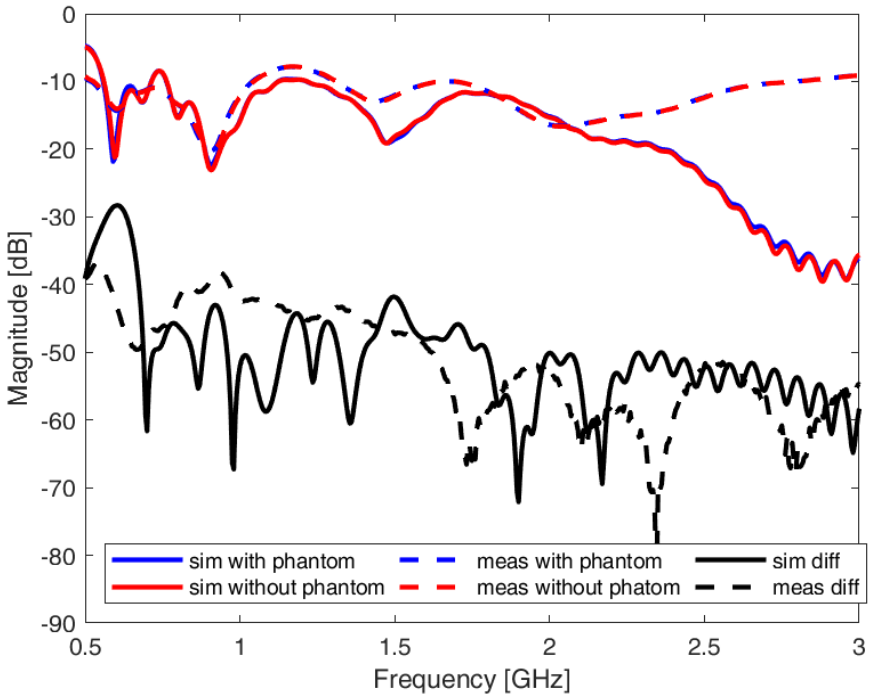

Figure 6-6 Antenna S-parameters with and without c2 phantom, and differential signals level of 'c2-s0' at position 4

The antenna's measured differential signal level at all positions with the following scenarios 'a2-s0', 'b2-s0', 'c2-s0', 'a2-b2', and 'b2-c2' are shown from Figure 6-7 to Figure 6-11. It is found from the figures that the measured differential signal levels of all scenarios are above -90dB, which is within the dynamic range of commercial VNAs. In particular, it is found that for all cases the differential signal level is above -50dB from 0.5 to 1.6 GHz, which is the frequency range of interest for image reconstruction.

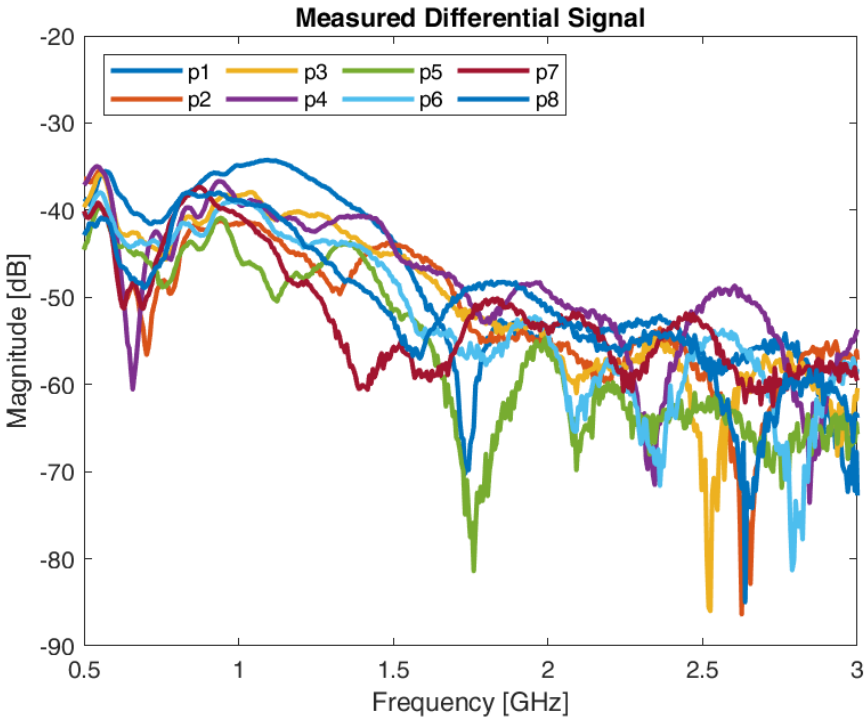

Figure 6-7 Measured differential signal of 'a2-s0' at all positions

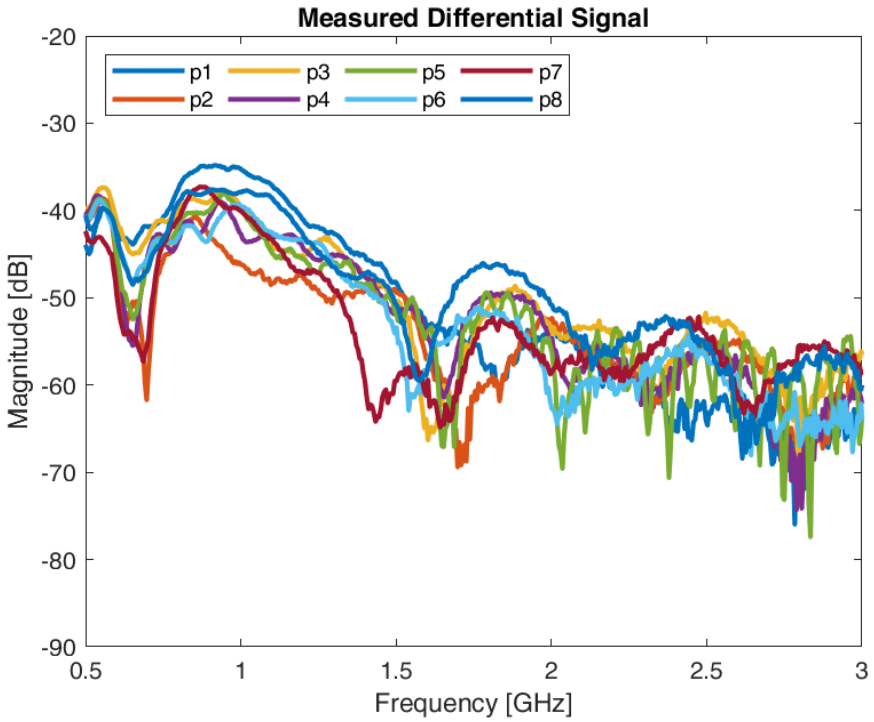

Figure 6-8 Measured differential signal of 'b2-s0' at all positions

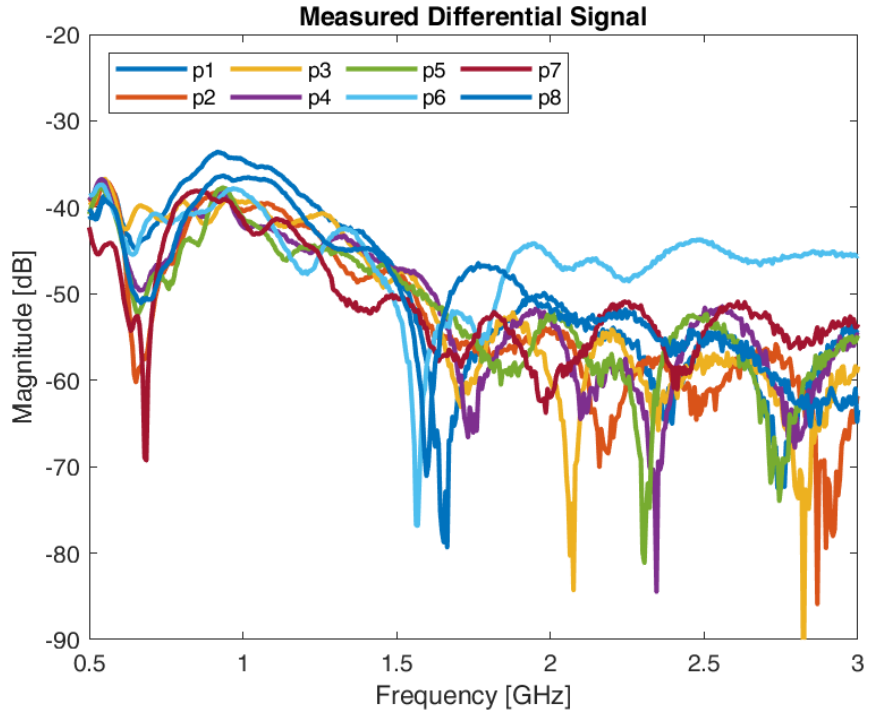

Figure 6-9 Measured differential signal of 'c2-s0' at all positions

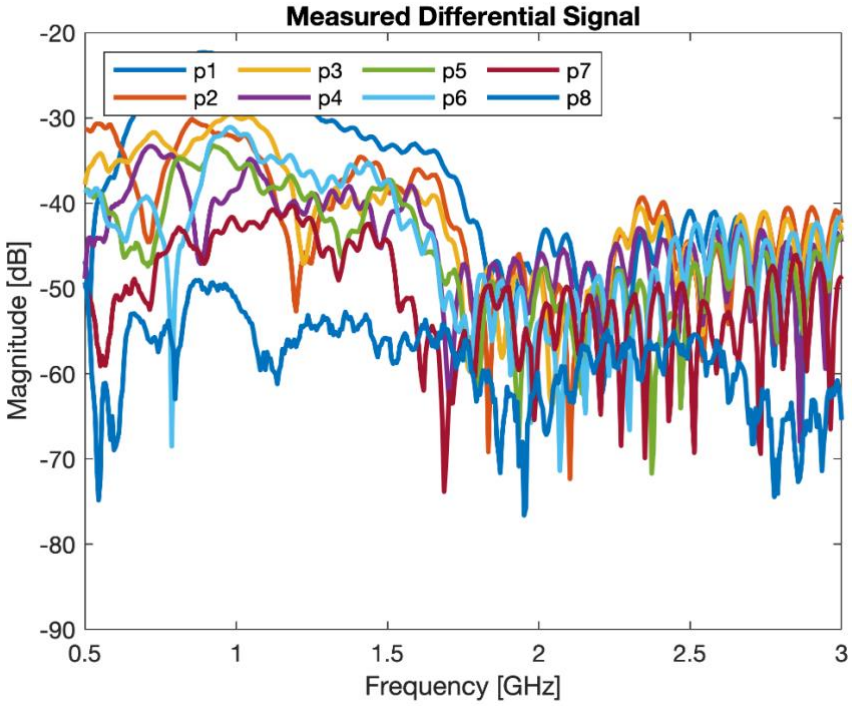

Figure 6-10 Measured differential signal of 'a2-b2' at all positions

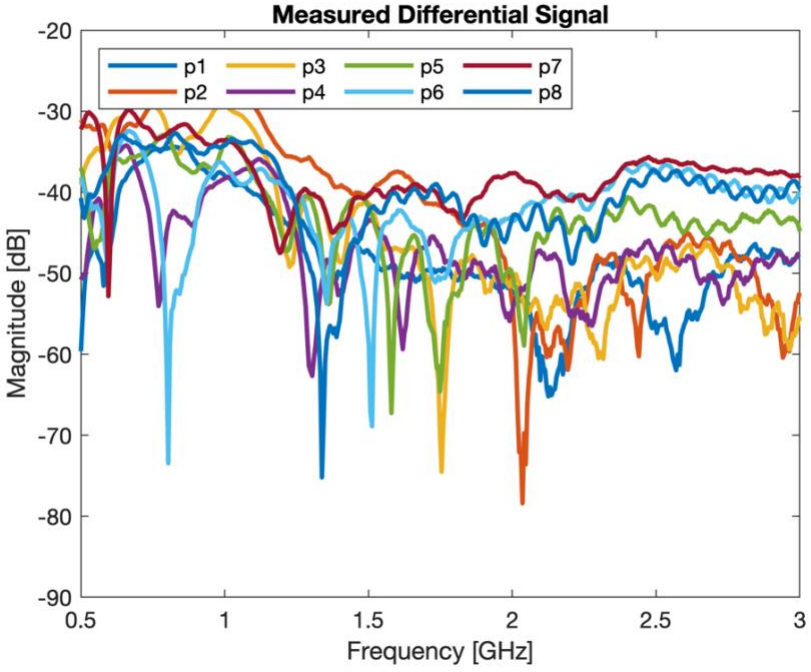

Figure 6-11 Measured differential signal of 'b2-c2' at all positions

6.3.1.2. Image Reconstruction

The algorithm used for processing the experimental data is the truncated singular value decomposition (TSVD) exploiting the distorted Born approximation (DBA), which is the same algorithm as the one used in Chapter 5 to process the simulation data. As it was discussed in the previous section, the differential signal level is higher below 1.6 GHz while at higher frequencies it is heavily corrupted by the noise. Therefore, the considered bandwidth for the data processing is from 0.7 to 1.6 GHz.

As it was demonstrated in equation (5-2), the linear inversion strategy based on the TSVD has been exploited. In Chapter 5, the kernel **K** in the equation is the simulated incident field in the region of interest. In this section, the kernel **K** in the analysis of the experimental data has been assumed as a simple 2D case: 8 point souces were acting as the antennas in the ROI. Neither the presence of the box nor the antenna behavior was considered. The unknown contrast in the ROI**, Δx,** was derived from the measured properties of the coupling medium in section 3.5. It is worth mentioning that each reconstruction is normalized with respect to the maximum value, thus providing a qualitative map of the intensity of the changes with respect to the scenario assumed as a reference. The results are given as 2D images corresponding to the yz-transverse cut of the investigated region in the x = 0 mm plane, which corresponds to the center of the antenna aperture. While in principle it could be possible to provide a 3D reconstruction, only the 2D result is reported, since this is more consistent with the fact that data were acquired using only one antenna moving along the y-axis.

Similar to the in-silico study data in chapter 5, the reconstructions of the experimental data of the five scenarios: a2-s0, b2-s0, c2-s0, a2-b2, b2-c2, are reported in Figure 6-12 (corresponding to the y-z plane in Figure 6-3, the unit of the y-axis and z-axis are in [mm]). In particular, The data sets a2-s0, b2-s0, and c2-s0 account for the changes that occurred with respect to the reference scenario (s0). The a2-b2 data set is representative of a scenario in which the changes occur only in the inner ellipsoid, b2-c2 accounted for the difference between the intermediate and final stages of the treatment. A rectangular mask in the region of interest has been used to

highlight the target area. The red contour in the figure indicates the ground truth of the outer ellipsoid, and the black contour in the figure indicates the ground truth of the inner ellipsoid. It is found that the reconstruction of the position and dimension of the target overlaps with the ground truth. The results show that the mono-statistic MWI system is capable of detecting the differential signal caused by the changing of dielectric properties in the region of interest. However, the variation of the inner ellipsoid is hard to identify. Thus, while proving the concept, the mono-statistic MWI system is unable to reveal the ablation stages during the treatment.

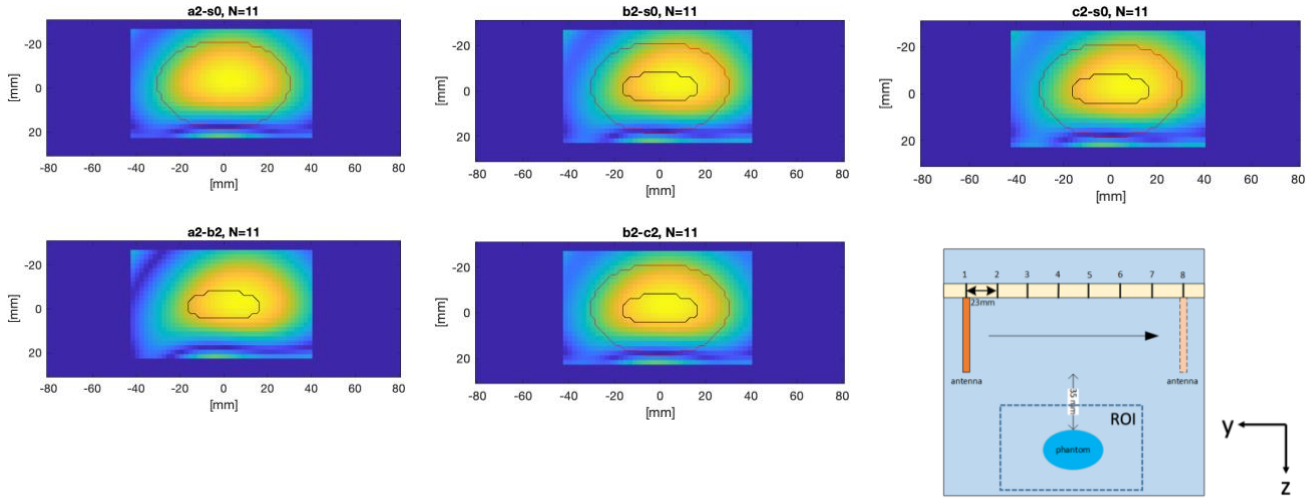

Figure 6-12 Reconstructions of target from five differential scenarios and the position of the ROI in the experimental set-up.

6.4. Summary

This chapter demonstrates the initial experimental validation of an MWI system to monitor liver thermal ablation. A multi-view, mono-statistic MWI system was realized. In particular, a slot-loaded antipodal Vivaldi antenna was moved linearly in front of an ablated liver phantom to measure the S-parameters at 8 different positions.

The measured S-parameters are in close agreement with the simulation results. Additionally, the differential signal level of the S-parameters stays well above the noise floor of the VNA for

all positions, thus being reliably measured. In particular, the differential signal level is above -50 dB in the frequency of interest (0.7-1.6 GHz). The reconstruction of the ROI shows that it is possible to reveal the position and dimensions of the target for all five scenarios considered. However, it was difficult to appreciate the variation of the inner ellipsoid. Nevertheless, this initial experiment paves the way for future realizations of a multi-view multi-statistic MWI system.

Chapter 7

7. Conclusions and Recommendations for the Future Work

7.1. Conclusions

The aim of the present work was the development of an experimental system for real-time monitoring of thermal ablation procedures by way of microwave imaging. Over the years, real-time monitoring of liver thermal ablation treatments has been considered a challenging task because conventional modalities such as X-ray, CT, PET/CT, MRI, and Ultrasound all have their constraints. Therefore, the successful execution of thermal ablation treatment still heavily relies on the clinician's experience. Microwave imaging is a modality that has the advantages of being non-invasive, based on non-ionizing radiation, portable, cost-effective, and capable of real-time monitoring. It is a modality that has been enormously investigated in recent decades and demonstrates promising results for biomedical applications. To the existing knowledge, it is the first time that a microwave imaging system has been developed for real-time monitoring.

7.1.1. Adding-Values and Novelties of the Thesis

Besides the general aim of the work, during the study, several aspects lead to original contributions, as listed in the following.

- **The design guidelines of an MWI system for liver thermal ablation monitoring were given**. It is well understood that due to the high electromagnetic power loss inside the biological tissues, only a limited frequency bandwidth is suitable for biomedical applications. The goal of the guideline is to precisely determine the useful frequency band and coupling medium properties that can be utilized for the MWI system. To this end, the abdomen was modeled as a layered structure, which in turn was represented by a transmission-line model. Similarly, the incident electromagnetic field was modeled through a plane wave impinging orthogonally on the layered phantom. As a result, numerical analysis on the transmission line model was carried out. The results bring to light that if selecting a certain working bandwidth (0.5-2 GHz) and coupling medium (ε=23, σ=0.07 S/m @ 1 GHz), the electromagnetic power transmitted from the EM source to the target under investigation can be maximized.

This study provides a rational approach towards the MWI system design rather than the direct utilization of wideband apparatuses in the MWI system and then selecting a certain frequency range through a trial and error process. It is worth mentioning that such a design guideline could not only be used for the system in this thesis but also be applicable to other biomedical imaging applications, such as brain or breast imaging.

- **Aiming for the optimal performance of the MWI system, the apparatuses were specially designed within the guidelines**. Three antipodal Vivaldi antennas were designed in the proposed working frequency and to work in the coupling medium. The study on different substrate materials shows that the antenna with RT/Duroid 6010 LMD material has the most promising results when working inside the coupling medium. An antipodal Vivaldi antenna (AVA) was designed using such material. Furthermore, an antipodal Vivaldi antenna with ceramic lens (AVA-CL) was proposed aiming for improving antenna radiation to the abdomen phantom. However, the large aperture dimension of such an antenna and the fabrication difficulties make it hardly considered as a feasible candidate for the MWI system. To further reduce the antenna's overall dimension, a slot-loaded antipodal Vivaldi antenna (SAVA) was designed. It demonstrates the most appealing features of the MWI system. SAVA showed a reduction of 28% in dimension as compared to AVA. Besides, the uncomplicated slot-loaded design is easy to fabricate and demonstrates a good performance towards reducing the mutual coupling effect between neighboring antennas. Finally, the antenna was fabricated and its performance was characterized in the coupling medium. The antenna's simulation and measurement results demonstrated a good agreement with each other.
- **The antenna mismatching issue when placed inside the coupling medium was solved**. The antenna has a mismatching issue when feeding by an SMA connector and placed inside the coupling medium. A simple but effective solution was proposed to

fix this problem: covering the connector pin with epoxy resin. According to the existing knowledge, it is the first time that such a problem was pinpointed and solved.

- **The experimental set-up of the MWI system was in-silico validated with the proposed apparatuses**. In particular, the initial MWI system experiment consists of eight slot-loaded antipodal Vivaldi antennas placed in a staggered configuration inside a tank filled with the coupling medium. A 3D-printed shell filled with tissue-mimicking materials represented the liver tissue during ablation. As the goal of the system is to provide real-time imaging, a computationally efficient qualitative MWI algorithm was used, the truncated singular value decomposition (TSVD) exploiting the distorted Born approximation (DBA) to elaborate the data sets. The reconstruction of 3D images of the domain of interest shows that the MWI system is capable of revealing the position of the target accurately in a timely manner. Furthermore, by processing the differential dataset between two different states, it is possible to identify the inner core of the ablation zone, hence indicating the specific ablation stages.
- **An initial experimental assessment was performed to validate the feasibility of the MWI system**. To this end, a simple multi-view mono-statistic MWI system consisting of one antenna moving linearly along the y-axis in front of the phantom was realized. The 2D imaging results show that it is possible to localize the phantom position and the dimension in a satisfactory way, in agreement with the in-silico analysis.

7.2. Recommendations for Future Work

The work proved both numerically and experimentally the capability of a MWI system to perform monitoring of liver thermal ablation. As the final goal of such a system is to provide real-time monitoring of the liver thermal ablation treatment in a clinical setting, there are several research directions that can be investigated in the future to look for improvements of the system performances, such as:

- **Investigation of different measurement configurations to improve the imaging results.** Due to the limitations of the hardware (fabricated antenna number, VNA port number, 3D-printed tank dimension, etc.), this thesis only demonstrates the results of an MWI system consisting of no more than 8 antennas. In principle, the imaging resolution and quality can be improved by using more antenna elements in the system. Additionally, the experimental validation was performed with one antenna only, moved in a linear fashion. Other measurement configurations consisting of more antenna elements should be studied in the future. In addition, it has to be considered that data acquisition must be fast enough to allow the whole MWI acquisition and processing procedure to be real-time.
- **Improvements in the data processing**. A greater number of frequency points can be acquired to increase the amount of data and improve rejection to noise. Improvements can also be foreseen for the imaging algorithm, either using a different algorithm, such as the iterated version of the dynamic bandwidth allocation, or incorporating available a priori information (e.g. a preparatory image) in the electromagnetic model used to build the imaging kernel **K**.
- **Ex-vivo experimental assessment**. In this study, the target in the experimental assessment of the MWI system is a 3D-printed phantom filled with tissue-mimicking material. Such a phantom can roughly represent the ablation zone in a realistic way. However, the final goal of the MWI system is to monitor a target whose properties evolve in real-time. Therefore, an investigation devoted to monitoring ex-vivo thermal liver ablation treatment with the proposed MWI system should be performed.
- **Integrating the MWI system into a wearable device.** The proposed MWI system consists of an antenna array immersed in the liquid coupling medium. Such a design can be difficult to implement in a clinical setting. The system could be redesigned to be more patient-friendly. Improvements could be made by designing a wearable waistband consisting of antennas embedded in a solid coupling medium.

References

[1] H. Sung, J. Ferlay, R. L. Siegel, M. Laversanne, I. Soerjomataram, A. Jemal, & F. Bray, "Global cancer statistics 2020: GLOBOCAN estimates of incidence and mortality worldwide for 36 cancers in 185 countries," *CA: a cancer journal for clinicians*, 71(3), 209-249, 2021.

[2] P. Srivatanakul, H. Sriplung, & S. Deerasamee, "Epidemiology of liver cancer: an overview," *Asian Pacific journal of cancer prevention*, *5*(2), 118-125, 2004.

[3] C. Y. Liu, K. F. Chen, & P. J. Chen, "Treatment of liver cancer,". *Cold Spring Harbor perspectives in medicine*, *5*(9), a021535, 2015.

[4] S. A. Wells, J. L. Hinshaw, M. G. Lubner, T. J. Ziemlewicz, C. L. Brace, & F. T. Lee, "Liver ablation: best practice," *Radiologic Clinics*, *53*(5), 933-971, 2015.

[5] M. Ahmed, L.Solbiati, C. L.Brace, D. J. Breen, M. R. Callstrom, J. W.Charboneau, ... & S. N. Goldberg, "Image-guided tumor ablation: standardization of terminology and reporting criteria—a 10-year update," *Radiology*, *273*(1), 241-260, 2014.

[6] C. L. Brace, "Microwave ablation technology: what every user should know," *Current problems in diagnostic radiology* 38.2: 61-67, 2009.

[7] J. L. Hinshaw, & F. T. Lee Jr, "Cryoablation for liver cancer," *Techniques in vascular and interventional radiology*, *10*(1), 47-57, 2007.

[8] J. P. Erinjeri, & T. W. Clark, "Cryoablation: mechanism of action and devices," *Journal of Vascular and Interventional Radiology*, *21*(8), S187-S191, 2010.

[9] M. F. Meloni, J. Chiang, P. F. Laeseke, C. F. Dietrich, A. Sannino, M. Solbiati, ... & F. T. Lee Jr, "Microwave ablation in primary and secondary liver tumors: technical and clinical approaches," *International Journal of Hyperthermia*, *33*(1), 15-24, 2017.

[10] S. Mulier, Y. Ni, L. Frich, F. Burdio, A. L. Denys, J. F. De Wispelaere, ... & L. Michel, "Experimental and clinical radiofrequency ablation: proposal for standardized description of coagulation size and geometry," *Annals of surgical oncology*, *14*(4), 1381-1396, 2007.

[11] E. K. Abdalla, J. N. Vauthey, L. M. Ellis, V. Ellis, R. Pollock, K. R. Broglio,... & S. A. Curley, "Recurrence and outcomes following hepatic resection, radiofrequency ablation, and combined resection/ablation for colorectal liver metastasee," *Annals of surgery*, *239*(6), 818, 2004.

[12] D. A. North, R. T. Groeschl, D. Sindram, J. B. Martinie, D.A. Iannitti, M. Bloomston, C. Schmidt, W. S. Rilling, T. C. Gamblin, R. C. Martin, "Microwave ablation for hepatic malignancies: a call for standard reporting and outcomes," *The American Journal of Surgery*, 208(2), 284-294, 2014.

[13] A. G. Webb, "Introduction to biomedical imaging," *John Wiley & Sons*, 2017.

[14] M. A. Brown, & R. C. Semelka, "MRI: basic principles and applications," *John Wiley & Sons*, 2011.

[15] V. Lopresto, R. Pinto, L. Farina & M. Cavagnaro, "Treatment planning in microwave thermal ablation: clinical gaps and recent research advances," *International Journal of Hyperthermia*, 33(1), 83-100. 2017.

[16] P. Bruners, G. D. Pandeya, E. Levit, E. Roesch, T. Penzkofer, P. Isfort, ... & A. H. Mahnken, "CT-based temperature monitoring during hepatic RF ablation: Feasibility in an animal model," *International Journal of Hyperthermia*, *28*(1), 55-61, 2012.

[17] L. Shi, & S. Tashiro, "Estimation of the effects of medical diagnostic radiation exposure based on DNA damage," *Journal of radiation research*, 59(suppl_2), ii121-ii129, 2018.

[18] B. Quesson, J. A. de Zwart, & C. T. Moonen, "Magnetic resonance temperature imaging for guidance of thermotherapy," *Journal of Magnetic Resonance Imaging: An Official Journal of the International Society for Magnetic Resonance in Medicine*, *12*(4), 525-533, 2000.

[19] R. C. Conceição, J. J. Mohr & M. O'Halloran (Eds.), "An introduction to microwave imaging for breast cancer detection". Basel, Switzerland:: *Springer International Publishing,* 2016.

[20] N. K. Nikolova, "Microwave imaging for breast cancer," *IEEE microwave magazine*, 12(7), 78-94, 2011.

[21] R. Scapaticci, L. Di Donato, I. Catapano, & L. Crocco, "A feasibility study on microwave imaging for brain stroke monitoring," *Progress In Electromagnetics Research* B, 40, 305-324, 2012.

[22] M. Haynes, J. Stang, & M. Moghaddam, "Real-time microwave imaging of differential temperature for thermal therapy monitoring," *IEEE Transactions on Biomedical Engineering*, 61(6), 1787-1797, 2014.

[23] B. Amin, A. Shahzad, L. Crocco, M. Wang, M. O'Halloran, A. González-Suárez, & M. A. Elahi, "A feasibility study on microwave imaging of bone for osteoporosis monitoring," *Medical & Biological Engineering & Computing*, 59(4), 925-936, 2021.

[24] V. Lopresto, R. Pinto, G. A. Lovisolo, & M. Cavagnaro, "Changes in the dielectric properties of ex vivo bovine liver during microwave thermal ablation at 2.45 GHz," *Physics in Medicine & Biology*, 57(8), 2309, 2012.

[25] R. Scapaticci, V. Lopresto, R. Pinto, M. Cavagnaro, & L. Crocco, "Monitoring thermal ablation via microwave tomography: An ex vivo experimental assessment," *Diagnostics*, 8(4), 81, 2018.

[26] G. C. Giakos, M. Pastorino, F. A. B. R. I. Z. I. O. Russo, S. Chowdhury, N. Shah, & W. Davros, "Noninvasive imaging for the new century," *IEEE Instrumentation & Measurement Magazine*, 2(2), 32-35, 1999.

[27] J. B. Campbell, & R. H. Wynne, "Introduction to remote sensing," *Guilford Press*, 2011.

[28] X. Zhuge, & A. G. Yarovoy, "A sparse aperture MIMO-SAR-based UWB imaging system for concealed weapon detection," *IEEE Transactions on Geoscience and Remote Sensing*, 49(1), 509-518, 2010.

[29] R. Persico, "Introduction to ground penetrating radar: inverse scattering and data processing," *John Wiley & Sons*, 2014.

[30] M. Pastorino, "Microwave imaging," Vol. 208, *John Wiley & Sons,* 2010.

[31] R. Benny, T. A. Anjit, & P. Mythili, "An overview of microwave imaging for breast tumor detection," *Progress In Electromagnetics Research* B, 87, 61-91, 2020.

[32] D. O. Rodriguez-Duarte, J. A. T. Vasquez, R. Scapaticci, L. Crocco, & F. Vipiana, "Assessing a microwave imaging system for brain stroke monitoring via high fidelity numerical modelling," *IEEE Journal of Electromagnetics, RF and Microwaves in Medicine and Biology*, 2021.

[33] M. Lazebnik, D. Popovic, L. McCartney, C. B. Watkins, M. J. Lindstrom, J. Harter, ... & W. Temple, "A large-scale study of the ultrawideband microwave dielectric properties of normal, benign and malignant breast tissues obtained from cancer surgeries," *Physics in medicine & biology*, 52(20), 6093, 2007.

[34] R. Scapaticci, V. Lopresto, R. Pinto, M. Cavagnaro, & L. Crocco, "Monitoring thermal ablation via microwave tomography: An ex vivo experimental assessment," *Diagnostics*, 8(4), 81, 2018.

[35] D. L. Colton, R. Kress, & R. Kress, "Inverse acoustic and electromagnetic scattering theory," Vol. 93, pp. xii+-334, *Berlin: Springer*, 1998.

[36] A. Abubakar, & P. M. van den Berg, "Iterative forward and inverse algorithms based on domain integral equations for three-dimensional electric and magnetic objects," *Journal of computational physics*, *195*(1), 236-262, 2004.

[37] J. Hadamard, "Lectures on Cauchy's Problem in Linear Partial Differential Equations," *Yale University Press, New Haven*, 1923.

[38] R. Scapaticci, J. Tobon, G. Bellizzi, F. Vipiana, & L. Crocco, "Design and numerical characterization of a low-complexity microwave device for brain stroke monitoring," *IEEE Transactions on Antennas and Propagation*, 66(12), 7328-7338, 2018.

[39] J. M. Beada'a, A. M. Abbosh, & P. Sharpe, "Planar array of corrugated tapered slot antennas for ultrawideband biomedical microwave imaging system," *International Journal of RF and Microwave Computer-Aided Engineering*, 23(1), 59-66, 2013.

[40] X. Li, S. K. Davis, S. C. Hagness, D. W. Van der Weide, & B. D. Van Veen, "Microwave imaging via space-time beamforming: Experimental investigation of tumor detection in multilayer breast phantoms," *IEEE Transactions on Microwave Theory and techniques*, 52(8), 1856-1865, 2004.

[41] P. M. Meaney, D. Goodwin, A. H. Golnabi, T. Zhou, M. Pallone, S. D. Geimer, G. Burke, and K. D. Paulsen, "Clinical Microwave Tomographic Imaging of the Calca neus: A First-in-Human Case Study of Two Subjects," *IEEE Transactions on Biomedical Engineering*, vol. 59, pp. 3304–3313, 2012.

[42] P. M. Meaney, M. W. Fanning, D. Li, S. P. Poplack, & K. D. Paulsen, "A clinical prototype for active microwave imaging of the breast," *IEEE Transactions on Microwave Theory and Techniques*, 48(11), 1841-1853, 2000.

[43] T. Zhou, P. M. Meaney, M. Pallone, D. Geimer, and K. D. Paulsen, "Microwave tomo-graphic imaging for osteoporosis screening: a pilot clinical study," *In 2010 Annual International Conference of the IEEE Engineering in Medicine and Biology*, pp. 1218–1221, 2010

[44] N. R. Epstein, P. M. Meaney, & K. D. Paulsen, "Microwave tomographic imaging utilizing low-profile, rotating, right angle-bent monopole antennas," *International Journal of Antennas and Propagation*, 2014.

[45] C. Gilmore, A. Zakaria, J. LoVetri, & S. Pistorius, "A study of matching fluid loss in a biomedical microwave tomography system," *Medical physics,* 40(2), 023101, 2013.

[46] E. Porter, E. Kirshin, A. Santorelli, M. Coates, & M. Popović, "Time-domain multistatic radar system for microwave breast screening," *IEEE Antennas and Wireless Propagation Letters*, 12, 229-232, 2013.

[47] G. N. Bindu, A. Lonappan, V.Thomas, C. K. Aanandan, & K. T. Mathew, "Dielectric studies of corn syrup for applications in microwave breast imaging," *Progress In Electromagnetics Research*, 59, 175-186, 2006.

[48] P. M. Meaney, T. Zhou, D. Goodwin, A. Golnabi, E. A. Attardo, & K. D. Paulsen, "Bone dielectric property variation as a function of mineralization at microwave frequencies," *Journal of Biomedical Imaging*, 2012.

[49] O. Karadima, M. Rahman, I. Sotiriou, N. Ghavami, P. Lu, S. Ahsan, & P. Kosmas, "Experimental Validation of Microwave Tomography with the DBIM-TwIST Algorithm for Brain Stroke Detection and Classification," *Sensors*, 20(3), 840, 2020.

[50] V. Hamsakutty, A. Lonappan, V. Thomas, G. Bindu, J. Jacob, J. Yohannan, & K. T. Mathew, "Coupling medium for microwave medical imaging applications," *Electronics Letters*, *39*(21), 1498-1499, 2003.

[51] J. Bourqui, M. Okoniewski, & E. C. Fear, "Balanced antipodal Vivaldi antenna with dielectric director for near-field microwave imaging," *IEEE Transactions on Antennas and Propagation*, *58*(7), 2318-2326, 2010.

[52] D. Oloumi, P. Boulanger, A. Kordzadeh, & K. Rambabu, "Breast tumor detection using UWB circular-SAR tomographic microwave imaging," *In 2015 37th Annual International Conference of the IEEE Engineering in Medicine and Biology Society (EMBC),* pp. 7063-7066, IEEE, 2015, August.

[53] G. Ruvio, & M. J. Ammann, "A miniaturized antenna for UWB-based breast imaging," *In 2009 3rd European Conference on Antennas and Propagation* (pp. 1864-1867), IEEE, 2009, March.

[54] J. Stang, M. Haynes, P. Carson, &, M. Moghaddam, "A preclinical system prototype for focused microwave thermal therapy of the breast," *IEEE Transactions on Biomedical Engineering*, 59(9), 2431-2438, 2012.

[55] J. Stang, "A 3D active microwave imaging system for breast cancer screening," *Duke University*, 7, 2008.

[56] D. O. Rodriguez-Duarte, J. A. Tobon Vasquez, R. Scapaticci, G. Turvani, M. Cavagnaro, M. R. Casu, ... & F. Vipiana, "Experimental Validation of a Microwave System for Brain Stroke 3-D Imaging," *Diagnostics*, 11(7), 1232, 2021.

[57] D. O. Rodriguez-Duarte, J. A. T. Vasquez, R. Scapaticci, L. Crocco, & F. Vipiana, "Brick Shaped Antenna Module for Microwave Brain Imaging Systems," *IEEE Antennas and Wireless Propagation Letters*, 2020.

[58] B. Amin, A. Shahzad, D. Kelly, M. O'Halloran, & A. Elahi, "Anthropomorphic calcaneus phantom for microwave bone imaging applications," *IEEE Journal of Electromagnetics, RF and Microwaves in Medicine and Biology,* 2020.

[59] B. Borja, J. A. Tirado, & H. Jardon, "An Overview of UWB Antennas for Microwave Imaging Systems for Cancer Detection Purposes," *Progress In Electromagnetics Research,* B, 80, 2018

[60] A. Yakovlev, S. Kim, & A. Poon, "Implantable biomedical devices: Wireless powering and communication," *IEEE Communications Magazine*, 50(4), 152-159, 2012.

[61] J. C. Bolomey, & L. Jofre, "Three decades of active microwave imaging achievements, difficulties and future challenges," *In 2010 IEEE International Conference on Wireless Information Technology and Systems* (pp. 1-4). IEEE, 2010, September.

[62] A. Kiourti, & K. S. Nikita, "A review of implantable patch antennas for biomedical telemetry: Challenges and solutions" [wireless corner]. *IEEE Antennas and Propagation Magazine*, 54(3), 210-228, 2012.

[63] W. C. Chew, & J. H. Lin, "A frequency-hopping approach for microwave imaging of large inhomogeneous bodies," *IEEE Microwave and Guided Wave Letters*, 5(12), 439-441, 1995.

[64] Y. M. Wang, & W. C. Chew, "An iterative solution of the two-dimensional electromagnetic inverse scattering problem," *International Journal of Imaging Systems and Technology*, 1(1), 100-108, 1989.

[65] I. Catapano, L. Di Donato, L. Crocco, O. M. Bucci, A. F. Morabito, T. Isernia, & R. Massa, "On quantitative microwave tomography of female breast," *Progress In Electromagnetics Research*, 97, 75-93, 2009.

[66] R. Scapaticci, L. Di Donato, I. Catapano, & L. Crocco, "A feasibility study on microwave imaging for brain stroke monitoring," *Progress In Electromagnetics Research*, 40, 305-324, 2012.

[67] M. Wang, L. Crocco, M. Cavagnaro, "Initial guidelines for the design of a microwave imaging system for ablation monitoring," *IEEE Journal of Electromagnetics, RF and Microwaves in Medicine and Biology*, 2021.

[68] M. Persson, A. Fhager, H. D. Trefna`, Y. Yu, T. McKelvey, G. Pegenius, J. E. Karlsson, & M. Elam, "Microwave-based stroke diagnosis making global prehospital thrombolytic treatment possible," *IEEE Transactions on Biomedical Engineering*, vol. 61, no. 11, pp. 2806–2817, Nov 2014.

[69] S. Candefjord, J. Winges, A. Malik, Y., Yu, T. Rylander, T. McKelvey, A. Fhager, M. Elam, and M. Persson, "Microwave technology for detecting traumatic intracranial bleedings: tests on phantom of subdural hematoma and numerical simulations," *Medical & Biological Engineer- ing & Computing*, vol. 55, no. 8, pp. 1177–1188, Aug 2017.

[70] T. Mobashsher, K. S. Bialkowski, A. M. Abbosh, and S. Crozier, "Design and experimental evaluation of a non-invasive microwave head imaging system for intracranial haemorrhage detection," *PLoS ONE*, vol. 11, no. 4, pp. 1–29, April 2016.

[71] M. Hopfer, R. Planas, A. Hamidipour, T. Henriksson, and S. Semenov, "Electromagnetic tomography for detection, differentiation, and moni- toring of brain stroke: A virtual data and human head phantom study." *IEEE Antennas and Propagation Magazine*, vol. 59, no. 5, pp. 86–97, Oct 2017.

[72] J. A. Tobon Vasquez, R. Scapaticci, G. Turvani, G. Bellizzi, D. O. Rodriguez-Duarte, N. Joachimowicz, B. Duchêne, E. Tedeschi, M. R. Casu, L. Crocco, F. Vipiana, "A Prototype Microwave System for 3D Brain Stroke Imaging," *Sensors*, 20, 2607, 2020.

[73] S. Semenov, J. Kellam, P. Althausen, T. Williams, A. Abubakar, A. Bulyshev, and Y. Sizo, "Microwave tomography for functional imaging of extremity soft tissues: feasibility assessment," *Physics in Med and Bio.*, vol. 52, no. 18, p. 5705, 2007.

[74] B. J. Mohammed, A. M. Abbosh, S. Mustafa, & D. Ireland, "Microwave system for head imaging," *IEEE Transactions on Instrumentation and Measurement*, 63(1), 117-123, 2013.

[75] I. Merunka, A. Massa, D. Vrba, O. Fiser, M. Salucci, & J. Vrba, "Microwave tomography system for methodical testing of human brain stroke detection approaches," *International Journal of Antennas and Propagation*, 2019.

[76] A. W. Preece, I. Craddock, M. Shere, L. Jones, & H. L. Winton, "MARIA M4: clinical evaluation of a prototype ultrawideband radar scanner for breast cancer detection," *Journal of Medical Imaging*, *3*(3), 033502, 2016.

[77] E. Porter, H. Bahrami, A. Santorelli, B. Gosselin, L. A. Rusch, & M. Popović, "A wearable microwave antenna array for time-domain breast tumor screening," *IEEE transactions on medical imaging*, 35(6), 1501-1509, 2016.

[78] H. Bahramiabarghouei, E. Porter, A. Santorelli, B. Gosselin, M. Popović, & L. A. Rusch, "Flexible 16 antenna array for microwave breast cancer detection," *IEEE Transactions on Biomedical Engineering*, 62(10), 2516-2525, 2015.

[79] M. Klemm, I. J. Craddock, J. A. Leendertz, A. Preece, & R. Benjamin, "Improved delay-and-sum beamforming algorithm for breast cancer detection," *International Journal of Antennas and Propagation*, 2008.

[80] M. Klemm, J. A. Leendertz, D. Gibbins, I. J. Craddock, A. W. Preece & R. Benjamin, "Microwave radar-based differential breast cancer imaging: Imaging in homogeneous breast phantoms and low contrast scenarios," *IEEE Transactions on Antennas and Propagation*, 58(7), 2337-2344, 2010.

[81] M. Klemm, D. Gibbins, J. A. Leendertz, T. Horseman, A. W. Preece, R. Benjamin, & I. J. Craddock, "Development and testing of a 60-element UWB conformal array for breast cancer imaging," *In Proceedings of the 5th European Conference on Antennas and Propagation* (EUCAP) (pp. 3077-3079), IEEE, 2011, April.

[82] O. Fiser, M. Helbig, J. Sachs, S. Ley, I. Merunka, & J. Vrba, "Microwave non-invasive temperature monitoring using UWB radar for cancer treatment by hyperthermia," *Progress In Electromagnetics Research*, 162, 1-14, 2018.

[83] A. Prokhorova, S. Ley, & M. Helbig, "Quantitative Interpretation of UWB Radar Images for Non-Invasive Tissue Temperature Estimation during Hyperthermia," *Diagnostics*, *11*(5), 818, 2021.

[84] S. M. Aguilar, M. A. Al-Joumayly, M. J. Burfeindt, N. Behdad, & S. C. Hagness, "Multiband miniaturized patch antennas for a compact, shielded microwave breast imaging array," *IEEE transactions on antennas and propagation*, 62(3), 1221-1231, 2013.

[85] D. Tajik, F. Foroutan, D. S. Shumakov, A. D. Pitcher, & N. K. Nikolova, "Real-time microwave imaging of a compressed breast phantom with planar scanning," *IEEE Journal of Electromagnetics, RF and Microwaves in Medicine and Biology*, 2(3), 154-162, 2018.

[86] R. K Amineh, A. Trehan, & N. K. Nikolova, "TEM horn antenna for ultra-wide band microwave breast imaging," *Progress In Electromagnetics Research*, 13, 59-74, 2009.

[87] M. A. Al-Joumayly, S. M. Aguilar, N. Behdad, & S. C. Hagness, "Dual-band miniaturized patch antennas for microwave breast imaging," *IEEE antennas and wireless propagation letters*, 9, 268-271, 2010.

[88] A. Molaei, A. G. Dagheyan, J. H. Juesas & J. Martinez-Lorenzo, "Miniaturized UWB Antipodal Vivaldi Antenna for a mechatronic breast cancer imaging system," *In 2015 IEEE International Symposium on Antennas and Propagation & USNC/URSI National Radio Science Meeting (pp. 352-353).* IEEE, 2015, July.

[89] X. Li, E. J. Bond, B. D. Van Veen, & S. C. Hagness, "An overview of ultra-wideband microwave imaging via space-time beamforming for early-stage breast-cancer detection," *IEEE Antennas and Propagation Magazine*, 47(1), 19-34, 2005.

[90] E. C. Fear, X. Li, S. C. Hagness, & M. A. Stuchly, "Confocal microwave imaging for breast cancer detection: Localization of tumors in three dimensions," *IEEE Transactions on biomedical engineering*, 49(8), 812-822, 2002.

[91] M. Abbak, M. N. Akıncı, M. Çayören, & İ. Akduman, "Experimental microwave imaging with a novel corrugated Vivaldi antenna," *IEEE Transactions on antennas and propagation*, 65(6), 3302-3307, 2017.

[92] I. Merunka, O. Fiser, L. Vojackova, J. Vrba, & D. Vrba, "Utilization potential of balanced antipodal Vivaldi antenna for microwave hyperthermia treatment of breast cancer," *In The 8th European Conference on Antennas and Propagation (EuCAP 2014)* (pp. 706-710). IEEE, 2014, April.

[93] X. Li, S. C. Hagness, M. K. Choi, & D. W. van der Weide, "Numerical and experimental investigation of an ultrawideband ridged pyramidal horn antenna with curved launching plane for pulse radiation," *IEEE Antennas and Wireless propagation letters*, 2, 259-262, 2003.

[94] R. K Amineh, A. Trehan, & N. K. Nikolova, "TEM horn antenna for ultra-wide band microwave breast imaging," *Progress In Electromagnetics Research*, 13, 59-74, 2009.

[95] S. Radiom, H. Aliakbarian, G. A. Vandenbosch, & G. G. Gielen, "An effective technique for symmetric planar monopole antenna miniaturization," *IEEE transactions on antennas and propagation*, 57(10), 2989-2996, 2009.

[96] Q. Ying, & W. Dou, "Simulation of two compact antipodal Vivaldi antennas with Radiation Characteristics enhancement," *In 2013 Proceedings of the International Symposium on Antennas & Propagation* (Vol. 1, pp. 523-526). IEEE, 2013, October.

[97] X. Fang, M. Ramzan, Q. Wang, & D. Plettemeier, "Compact antipodal Vivaldi antennas for body area communication," *In Advances in Body Area Networks* I (pp. 357-369). Springer, Cham, 2019.

[98] F. S. Di Clemente, M. Helbig, J. Sachs, U. Schwarz, R .Stephan, & M. A. Hein, "Permittivity-matched compact ceramic ultra-wideband horn antennas for biomedical diagnostics," *In Proceedings of the 5th European Conference on Antennas and Propagation* (EUCAP) (pp. 2386-2390), IEEE, 2011, April.

[99] A. Hamidipour, T. Henriksson, M. Hopfer, R. Planas, & S. Semenov, "Electromagnetic tomography for brain imaging and stroke diagnostics: Progress towards clinical application," *In Emerging Electromagnetic Technologies for Brain Diseases Diagnostics, Monitoring and Therapy* (pp. 59-86). Springer, Cham, 2018.

[100] E. Razzicchia, P. Lu, W. Guo, O. Karadima, I.Sotiriou, N. Ghavami, ... & P. Kosmas, "Metasurface-Enhanced Antennas for Microwave Brain Imaging," *Diagnostics*, 11(3), 424, 2021.

[101] E. Razzicchia, I. Sotiriou, H. Cano-Garcia, E. Kallos, G. Palikaras, & P. Kosmas, "Feasibility study of enhancing microwave brain imaging using metamaterials," *Sensors*, 19(24), 5472, 2019.

[102] R. C. Hansen, "Fundamental limitations in antennas," *Proceedings of the IEEE*, 69(2), 170-182, 1981.

[103] M. Fallahpour, & R. Zoughi, "Antenna miniaturization techniques: A review of topology-and material-based methods," *IEEE Antennas and Propagation Magazine*, 60(1), 38-50, 2017.

[104] R. Cicchetti, A. Faraone, E. Miozzi, R. Ravanelli & O. Testa, "A high-gain mushroom-shaped dielectric resonator antenna for wideband wireless applications," *IEEE Transactions on Antennas and Propagation,* 64(7), 2848-2861, 2016.

[105] M.Wang, L. Crocco, M. Cavagnaro, "Antipodal Vivaldi Antenna with Ceramic Cone Lens for Biomedical Microwave Imaging Systems", *In 2021 15th European Conference on Antennas and Propagation* (EuCAP) (pp. 1-4). IEEE, 2021.

[106] N. N. Wang, M. Fang, H. T. Chou, J. R. Qi, & L. Y. Xiao, "Balanced antipodal Vivaldi antenna with asymmetric substrate cutout and dual-scale slotted edges for ultrawideband operation at millimeter-wave frequencies," *IEEE Transactions on Antennas and Propagation,* 66(7), 3724-3729, 2018.

[107] I. T. Nassar, & T. M. Weller, "A novel method for improving antipodal Vivaldi antenna performance," *IEEE Transactions on Antennas and Propagation*, 63(7), 3321-3324, 2015.

[108] H. Hong, J. Ahn, J. G. Jeong, & Y. J. Yoon, "Gain enhancement technique for an antipodal Vivaldi antenna. *In 2015 IEEE International Symposium on Antennas and Propagation & USNC/URSI National Radio Science Meeting* (pp. 2343-2344). IEEE, 2015, July.

[109] W. Wang, & Y. Zheng, "Improved design of the Vivaldi dielectric notch radiator with etched slots and a parasitic patch," *IEEE Antennas and Wireless Propagation Letters*, 17(6), 1064-1068, 2018.

[110] X. Li, M. Jalilv & Y. L. Sit, & T. Zwick, "A compact double-layer on-body matched bowtie antenna for medical diagnosis," *IEEE transactions on antennas and propagation*, 62(4), 1808-1816, 2014.

[111] A. T. Mobashsher, A. Mahmoud, & A. M. Abbosh, "Portable wideband microwave imaging system for intracranial hemorrhage detection using improved back-projection algorithm with model of effective head permittivity," Scientific reports, 6(1), 1-16, 2016.

[112] M. Z. Mahmud, M. T. Islam, N. Misran, S. Kibria, & M. Samsuzzaman, "Microwave imaging for breast tumor detection using uniplanar AMC based CPW-fed microstrip antenna," *IEEE Access*, 6, 44763-44775, 2018.

[113] O. M. Bucci, L. Crocco, R. Scapaticci, & G. Bellizzi, "On the design of phased arrays for medical applications," *Proceedings of the IEEE*, 104(3), 633-648, 2016.

[114] S. A. Rezaeieh, A. Zamani, & A. M. Abbosh, "3-D wideband antenna for head-imaging system with performance verification in brain tumor detection," *IEEE Antennas and Wireless Propagation Letters*, *14*, 910-914, 2014.

[115] K. D. Paulsen, & P. M. Meaney, "Nonactive antenna compensation for fixed-array microwave imaging. I. Model development," *IEEE Transactions on Medical Imaging*, 18(6), 496-507, 1999.

[116] M. O'Halloran, M. Glavin, & E. Jones, "Rotating antenna microwave imaging system for breast cancer detection," *Progress In Electromagnetics Research*, 107, 203-217, 2010.

[117] A. Janjic, M. Cayoren, I. Akduman, T. Yilmaz, E. Onemli, O. Bugdayci, & M. E. Aribal, "SAFE: A Novel Microwave Imaging System Design for Breast Cancer Screening and Early Detection—Clinical Evaluation," *Diagnostics*, 11(3), 533, 2021.

[118] O. M. Bucci, & T. Isernia, "Electromagnetic inverse scattering: Retrievable information and measurement strategies," *Radio Science*, *32*(6), 2123-2137, 1997.

[119] X. Chen, "*Computational methods for electromagnetic inverse scattering,"* John Wiley & Sons, 2018.

[120] O. M. Bucci, L. Crocco, & R. Scapaticci, "On the optimal measurement configuration for magnetic nanoparticles-enhanced breast cancer microwave imaging," *IEEE Transactions on Biomedical Engineering*, *62*(2), 407-414, 2014.

[121] M. Helbig, K. Dahlke, I. Hilger, M. Kmec, & J. Sachs "Design and test of an imaging system for UWB breast cancer detection," *Frequenz*, 66(11-12), 387-394, 2012.

[122] K. Kanazawa, K. Noritake, Y. Takaishi and S. Kidera, "Microwave Imaging Algorithm Based on Waveform Reconstruction for Microwave Ablation Treatment, "*IEEE Transactions on Antennas and Propagation*, vol. 68, no. 7, pp. 5613-5625, July 2020.

[123] G. Chen, J. Stang, M. Haynes, E. Leuthardt, M. Moghaddam, "Real-time three-dimensional microwave monitoring of interstitial thermal therapy," *IEEE Transactions on Biomedical Engineering*, 65(3), 528-538 2017.

[124] B. M. Kolundzija, J. S. Ognjanovic, & T. Sarkar, "WIPL-D: Electromagnetic modeling of composite metallic and dielectric structures: Software and user's manual," *Artech House*, 2000.

[125] R. Drake, A. W. Vogl, & A. W. Mitchell, "Gray's Anatomy for Students E-Book", *Elsevier Health Sciences*. 2009.

[126] H. Bismuth, "Surgical anatomy and anatomical surgery of the liver", *World journal of surgery*, 6(1), 3-9,1982.

[127] Abdominal MRI | Insight Medical Imaging. Retrieved 13 May 2021, from https://x-ray.ca/services/magnetic-resonance/abdominal-mri-scan/, 2021.

[128] A. Peyman, & C. Gabriel, "Cole–Cole parameters for the dielectric properties of porcine tissues as a function of age at microwave frequencies," *Physics in Medicine & Biology*, 55(15), N413, 2010.

[129] S. Gabriel, R. W. Lau, & C. Gabriel, "The dielectric properties of biological tissues: III. Parametric models for the dielectric spectrum of tissues," *Physics in Medicine & Biology*, 41(11), 2271, 1996.

[130] G. Ruvio, L. Farina, A. Bottiglieri, J. Eaton-Evans, M. E. Elahi, M. O'Halloran, R. Pinto, V. Lopresto, and M. Cavagnaro, "Comparison of coaxial open-ended probe based dielectric measurements on ex-vivo thermally ablated liver tissue," *in 2019 13th European Conference on Antennas and Propagation* (EuCAP). IEEE, pp.1–4, 2019.

[131] I. G. Zubal, C. R. Harrell, E. O. Smith, Z. Rattner, G. Gindi, & P. B. Hoffer, "Computerized three-dimensional segmented human anatomy, " *Medical physics*, 21(2), 299-302, 1994.

[132] O. Akkus, A. Oguz, M. Uzunlulu, & M. Kizilgul, "Evaluation of skin and subcutaneous adipose tissue thickness for optimal insulin injection", *J Diabetes Metab*, 3(216), 2, 2012.

[133] C. A. Balanis, "Advanced engineering electromagnetics", *John Wiley & Sons*, 1999.

[134] R. Scapaticci, M. Bjelogrlic, J. A. T. Vasquez, F. Vipiana, M. Mattes, and L. Crocco, "Microwave technology for brain imaging and monitoring: physical foundations, potential and limitations," in *Emerging Electromagnetic Technologies for Brain Diseases Diagnostics, Monitoring and Therapy*, *L. Crocco, I. Karanasiou, M. L. James, and R. C. Conceição, (Eds). Springer*, 2018, pp. 7–35

[135] J. VanderKruk, C. Steelman, A. Endres, and H. Vereecken, "Dispersion Inversion of electromagnetic pulse propagation with in freezing and thawing soil waveguides," *Geophysical Research Letters*, vol.36, no.18, 2009.

[136] M. Wang, L. Farina, L. Crocco and M. Cavagnaro, "Changes in dielectric properties following a microwave thermal ablation procedure," *In 2021 International Conference on Electromagnetics in Advanced Applications (ICEAA)* (pp. 255-255), IEEE, 2021.

[137] D. B. Davidson, "Computational electromagnetics for RF and microwave engineering," *Cambridge University Press*, 2010.

[138] A. M. Abbosh, H. K. Kan, & M. E. Bialkowski, "Compact ultra-wideband planar tapered slot antenna for use in a microwave imaging system," *Microwave and optical technology letters*, 48(11), 2212-2216, 2006.

[139] D. M. Pozar, "Microwave engineering," *John wiley & sons,* 2011.

[140] T. Maleszka and G. Jaworski, "Broadband stripline to microstrip transition with constant impedance field matching section for applications in multilayer planar technologies," *In 18-th International Conference on Microwaves, Radar and Wireless Communications* (pp. 1-4), IEEE, 2010.

[141] R. C. Hansen, "Fundamental limitations in antennas," *Proceedings of the IEEE*, *69*(2), 170-182, 1981.

[142] P. Fei, Y. Jiao, W. Hu and F. Zhang, "A Miniaturized Antipodal Vivaldi Antenna With Improved Radiation Characteristics," in *IEEE Antennas and Wireless Propagation Letters*, vol. 10, pp. 127-130, 2011.

[143] J. Ao, J. Huang, W. Wu, & N. Yuan, "A miniaturized Vivaldi antenna by loading with parasitic patch and lumped resistor," *AEU-International Journal of Electronics and Communications*, 81, 158-162, 2017.

[144] V. Lopresto, L. Strigari, L. Farina, S. Minosse, R. Pinto, D. D'Alessio, B. Cassano, M. Cavagnaro, "CT-based investigation of the contraction of ex vivo tissue undergoing microwave thermal ablation," *Phys. Med. Biol.*, 63, 055019, 2018.

[145] M. N. Akınc, "Improving near-field orthogonality sampling method for qualitative microwave imaging,". *IEEE Transactions on Antennas and Propagation*, 66(10), 5475-5484, 2018.

[146] R. Scapaticci, G. G. Bellizzi, M. Cavagnaro, V. Lopresto, & L.Crocco, "Exploiting microwave imaging methods for real-time monitoring of thermal ablation", *International Journal of Antennas and Propagation*, 2017.

[147] M. Bertero, P. Boccacci, "Introduction to Inverse Problems in Imaging," *CRC Press: Boca Raton, FL, USA*, 2020.

[148] S. Kidera, L.M. Neira, B.D. van Veen, S.C. Hagness, "TDOA-based microwave imaging algorithm for real-time microwave ablation monitoring," *International Journal of Microwave and Wireless Technologies*, *10*(2), 169-178, 2018.